ATOMIC MOTION IN OPTICAL POTENTIALS

by

MARTIN CHRISTIAN FISCHER, M.A.

DISSERTATION

Presented to the Faculty of the Graduate School of
The University of Texas at Austin
in Partial Fulfillment
of the Requirements
for the Degree of

DOCTOR OF PHILOSOPHY

THE UNIVERSITY OF TEXAS AT AUSTIN
May 2001

ATOMIC MOTION IN OPTICAL POTENTIALS

APPROVED BY
DISSERTATION COMMITTEE:

Supervisor: ____________________

____

____

____

Manfred Fink

To my family for their never-ending love and support.

Acknowledgements

I am grateful to have had the opportunity to spend most of my graduate career in Mark Raizen's laboratory at The University of Texas at Austin. Mark is an excellent physicist and is always willing to share his knowledge with his group. He also shares his enthusiasm for physics and his creativity with the people around him. His fairness as a supervisor is equaled by his compassion for his students. I have tremendously enjoyed the time working with him and hope to have picked up some of his physical intuition.

Cyrus Bharucha and Kirk Madison showed me the ropes in the lab and never ceased to offer help and support wherever needed. I enjoyed Cyrus' company and friendship from the summers in Austin to the winters on the ski slopes of Colorado and Switzerland. With Kirk I spent many days and nights hunting for signals and discussing all sorts of topics. Kirk proved his skills not only in the lab but also on the soccer field. He is an excellent teammate and a great friend.

Braulio Gutiérrez joined the sodium and the soccer teams a couple of years later and has performed great in both. Together we have set up the current experiment. With his sense of humor and experimental skills he has made the time very enjoyable and productive. Recently Artëm Dudarev enrolled in our team and has always offered help and support without hesitation.

I also want to thank our post-doc Valery Milner for help in the experiment and many enjoyable days in the office. The discussions I had with him were numerous and always helpful. To Dan Steck I am indebted for answering so many questions, ranging from physics to motorcycles, from computers to travel. His range and depth of knowledge never ceases to amaze me. Windell Oskay has my appreciation for providing the coolest 3D-graphics and lots of fine chocolate. Thanks to all the past and current members of the Raizen group, including Bruce Klappauf, Jay Hanssen, Kevin Henderson, Artur Widera, Adrienne Lipoma and Patrick Bloom, who have provided a great environment that has made work in the lab fun and interesting. I also want to thank all members for their help in the final editing of this dissertation.

For their theoretical support I want to thank Bala Sundaram, Qian Niu and his student Roberto Diener. They have contributed much to the theoretical and numerical analysis of our experiments.

Les Deavers, Allan Schroeder and their crew from the Physics Department Mechanical Section have helped me in many ways during the construction of our apparatus. Thanks also go to Norma Kotz, Glenn Suchan, Jan Dunn, Dorothy Walker and Olga Vorloou for making dealing with administrative issues a breeze.

Many other people have helped me throughout the time in Austin and contributed to making this time an enjoyable and productive period. Thanks to all of them.

Finally I am deeply grateful for the love and support of my family. My folks in Germany have always supported my decisions, no matter what. Most importantly, my wife Maria has offered encouragement, patience and help in completing this work, while performing the most challenging job of taking care of our daughter Emma. They both added an abundance of joy and happiness to my life.

ATOMIC MOTION IN OPTICAL POTENTIALS

Publication No. ___________________

Martin Christian Fischer, Ph.D.
The University of Texas at Austin, 2001

Supervisor: Mark G. Raizen

This dissertation describes the experimental study of atomic motion in optical potentials. Our system consists of ultra-cold sodium atoms in an optical potential created by a standing wave of light. As we will show, the properties of this system are closely related to those of an electron in a crystal lattice.

First, we describe the study of the transport properties of an atom in an accelerated lattice. For moderate acceleration, we can observe coherent effects in our system that are obscured by short relaxation times in the corresponding condensed matter system. Bloch states and how they are modified by applied static and time-dependent fields are investigated with spectroscopic tools.

For a large acceleration of the lattice, atoms can escape from the trapping potential via tunneling. The behavior of this unstable system may be expected to follow the universal exponential decay law. This exponential law, however, is not fully consistent with quantum mechanics. Initially the number of trapped atoms shows strong non-exponential decay features before evolving into the characteristic exponential decay. We repeatedly measure the number of atoms that remain trapped during the initial period of non-exponential decay. Depending on the time delay between successive measurements we observe a decay that is suppressed or enhanced as compared to the unperturbed system. The experiments described here are the first and only observation of these Quantum Zeno and Anti-Zeno effects in an unstable quantum system.

The manipulation of the atomic motional state, as described here, is based on the exchange of momentum between the atom and the light beams forming the optical potential. An atom, changing its momentum due to the interaction with the optical lattice, will cause a corresponding change of the number of photons in the constituent light beams. We can measure this change of optical power in order to obtain information about the momentum distribution of the atomic sample. The fundamental properties of this method, named the method of recoil-induced resonances, are derived here. Furthermore, a novel experimental method is presented that greatly improves the sensitivity of the measurement.

Table of Contents

List of Figures

Chapter 1

Introduction

1.1 The interaction of atoms and light

The manipulation of the motional state of individual atoms with electromagnetic light fields was observed as early as 1930, when Frisch measured the deflection of an atomic beam with resonant light from a sodium lamp [1]. The measured deflection was caused by the recoil momentum that an atom acquires when absorbing or emitting a single photon of light. When an atom absorbs a photon from a beam of light, it acquires momentum in the direction of the light beam. Since scattered photons are emitted without preferred direction, the momentum acquired during the emission averages to zero over many cycles. This leads to a net force on the atom which is called the *spontaneous force*, or *radiation pressure*. The spontaneous force scales with the scattering rate and for large detunings falls off quadratically with the detuning Δ_{L} of the light from the atomic resonance [2]

$$F_{\mathrm{spont}} \propto \frac{I}{\Delta_{\mathrm{L}}^2}, \tag{1.1}$$

where I is the laser intensity.

Another type of force is based on the coherent scattering of photons. The oscillating electric field of light can induce a dipole moment in the atom. If the induced dipole moment is in phase with the the electric field, the interaction potential is lower in regions of high field and the atom will experience a force towards those regions. If it is out of phase, a force pointing away from regions of high field results. This force is called the *dipole force.* As opposed to the spontaneous force, the dipole force only falls off linearly with the detuning from the atomic resonance in the limit of large detuning [2]

$$F_{\mathrm{dipole}} \propto \frac{\nabla I}{\Delta_{\mathrm{L}}}. \tag{1.2}$$

From the scaling laws for the two types of forces it is clear that with sufficient laser intensity, the spontaneous force can be made negligibly small while still generating an appreciable dipole force. As early as 1970, Ashkin succeeded in trapping small particles with a pair of opposing, focused laser beams, making use of both types of forces. However, only the relatively recent development of laser cooling and trapping techniques have created the conditions for controlled manipulation of atoms with the dipole force alone [3]. While the laser cooling and trapping required to prepare our atomic sample utilized near resonant light and thus both types of light forces, the optical lattices were composed of far-detuned light, so that only the dipole interaction was important.

1.2 Optical lattices and the connection to solid state physics

In all the experiments described in this work, we created a periodic optical potential by spatially overlapping two laser light beams. The periodicity of the resulting standing wave was determined by the interference pattern in the region of overlap. In the nodes of a standing wave, the electric field of the light interferes destructively and atoms at those positions are unaffected by the light. Away from the nodes, the dipole interaction causes a light-induced shift of the atomic energy levels, which is maximal at the anti-nodes. This shift of the energy levels is another way of describing the aforementioned dipole force.

It is important to note that this force or level shift is periodic in space. The system of a particle in a periodic potential has been studied in great detail. It is a textbook model of an electron in a crystal lattice. In the 1920's Bloch studied the states in such a system and arrived at the conclusion that due to the periodicity of the lattice, the eigenstates are plane waves modulated by periodic functions of position [4]. The implications of these findings on the description of transport in periodic potentials under the influence of externally applied fields are profound. Some of the resulting effects, such as Bloch oscillations and Wannier-Stark states, are treated in more detail in Chapter 3. Experimental verification of those predicted effects in crystal lattices, however, has been hindered by extremely short relaxation times. Electrons in a crystal lattice can scatter on impurities, dislocations, phonons and even on other electrons. If the scattering occurs on a time scale faster than the time scale for coherent evolution of the system, coherent transport effects are destroyed. Advances in the production of very high purity superlattice structures in the 1970's allowed the experimental investigation of some of those coherent effects for the first time [5]. However, the ratio of the relaxation time to the characteristic time scale for coherent evolution in those systems was still only on the order of unity.

In our system we can achieve a ratio on the order of 10^3. The relaxation time is mainly limited by spontaneous emission during the interaction, which can be made very small by detuning far from resonance. This high ratio and the ability to dynamically control the interaction potential in real-time during the experiment allowed us to observe many of the coherent effects which are inaccessible in solid state systems. A more detailed comparison of the solid state and atom optics system is given in a recent overview article [6] and the dissertation of Madison [7].

1.3 Theoretical description

1.3.1 Interaction Hamiltonian

In this section, we derive the effective Hamiltonian for a two-level atom in a standing wave of far-detuned light. In the semiclassical derivation we treat the electromagnetic field classically. This formulation closely follows the derivation by Graham et al. [8].

The atom is assumed to have a ground state $|\mathrm{g}\rangle$ and an excited state $|\mathrm{e}\rangle$, separated in energy by $\hbar\omega_0$. For a single atom of such type in a light field $\mathbf{E}(\mathbf{r}, t)$, the Hamiltonian is the sum of three contributions: the center of mass part, the internal energy, and the interaction energy [9]

$$H = H_{\mathrm{CM}} + H_{\mathrm{internal}} + H_{\mathrm{interaction}}, \tag{1.3}$$

where

$$H_{\mathrm{CM}} = \frac{p^2}{2M}, \tag{1.4}$$

$$H_{\mathrm{internal}} = \frac{1}{2}\hbar\omega_0\, \sigma_z, \tag{1.5}$$

and

$$\begin{aligned} H_{\mathrm{interaction}} &= -\mathbf{d} \cdot \mathbf{E}(\mathbf{r}, t) && (1.6) \\ &= -\Big(\langle \mathrm{e}|\mathbf{d} \cdot \mathbf{E}|\mathrm{g}\rangle\, \sigma^+ + \langle \mathrm{g}|\mathbf{d} \cdot \mathbf{E}|\mathrm{e}\rangle\, \sigma^-\Big). && (1.7) \end{aligned}$$

The symbols $\sigma^\pm$ and σ_z denote the Pauli spin matrices. For a linear polarization vector ϵ of the light, we can define the resonant Rabi frequency as

$$\Omega = -\frac{\langle \mathrm{e}|\mathbf{d} \cdot \mathbf{E}|\mathrm{g}\rangle}{\hbar} = -\frac{\langle \mathrm{g}|\mathbf{d} \cdot \mathbf{E}|\mathrm{e}\rangle}{\hbar} = -\frac{\langle \mathrm{g}|\mathbf{d} \cdot \epsilon|\mathrm{e}\rangle}{\hbar} E, \tag{1.8}$$

where in the last step we have assumed a slow variation of the electric field amplitude $E(\mathbf{r}, t)$.

One of the simplest methods of creating an optical lattice is to overlap two laser beams spatially. To simplify the analysis, we assume that the polarization of both beams is linear and their polarization vectors are parallel. The electric field is then of the form

$$\mathbf{E}(\mathbf{r},t) = \frac{1}{2}\epsilon\left(E_1\, e^{i(\mathbf{k}_1\cdot\mathbf{r}-\omega_1\, t)} + E_2\, e^{i(\mathbf{k}_2\cdot\mathbf{r}-\omega_2\, t)}\right) + c.c. \tag{1.9}$$

Using this light field, we find that the interaction term is

$$\begin{aligned} H_{\text{interaction}} &= \hbar\frac{\Omega_1}{2}\left(\sigma^- e^{-i(\mathbf{k}_1\cdot\mathbf{r}-\omega_1 t)} + \sigma^+ e^{i(\mathbf{k}_1\cdot\mathbf{r}-\omega_1 t)}\right) \\ &\quad + \hbar\frac{\Omega_2}{2}\left(\sigma^- e^{-i(\mathbf{k}_2\cdot\mathbf{r}-\omega_2 t)} + \sigma^+ e^{i(\mathbf{k}_2\cdot\mathbf{r}-\omega_2 t)}\right), \end{aligned} \tag{1.10}$$

where we have used the rotating wave approximation to drop the counter-rotating terms $\sigma^+ e^{+i\omega t}$ and $\sigma^- e^{-i\omega t}$ [9]. To separate the center of mass motion of the atoms from their internal state we write the atomic state as

$$|\Psi(\mathbf{r},t)\rangle = c_{\text{g}}(\mathbf{r},t)|\text{g}\rangle + c_{\text{e}}(\mathbf{r},t)|\text{e}\rangle. \tag{1.11}$$

If we insert $|\Psi\rangle$ into the Schrödinger equation,

$$i\hbar\frac{\partial}{\partial t}|\Psi\rangle = H|\Psi\rangle, \tag{1.12}$$

with the full Hamiltonian as in Eq. (1.3) and project onto the internal states $|\text{g}\rangle$ and $|\text{e}\rangle$, we find the set of equations

$$\begin{aligned} i\hbar\partial_t c_{\text{g}} &= \left(-\hbar\frac{\omega_0}{2} + \frac{p^2}{2M}\right) c_{\text{g}} \qquad (1.13) \\ &\quad + \frac{\hbar}{2}\left(\Omega_1\, e^{-i(\mathbf{k}_1\cdot\mathbf{r}-\omega_1 t)} + \Omega_2\, e^{-i(\mathbf{k}_2\cdot\mathbf{r}-\omega_2 t)}\right) c_{\text{e}} \\ i\hbar\partial_t c_{\text{e}} &= \left(\hbar\frac{\omega_0}{2} + \frac{p^2}{2M}\right) c_{\text{e}} \qquad (1.14) \\ &\quad + \frac{\hbar}{2}\left(\Omega_1\, e^{i(\mathbf{k}_1\cdot\mathbf{r}-\omega_1 t)} + \Omega_2\, e^{i(\mathbf{k}_2\cdot\mathbf{r}-\omega_2 t)}\right) c_{\text{g}}. \end{aligned}$$

We can define $\delta = \omega_2 - \omega_1$ as being the frequency difference between the two constituent beams and $\Delta_{\mathrm{L}} = \frac{\omega_1+\omega_2}{2} - \omega_0$ as their average detuning from resonance. The phase transformations

$$\begin{aligned} \tilde{c}_{\mathrm{g}}(\mathbf{r},t) &= \exp\left[i(\frac{\delta}{2} - \frac{\omega_0}{2})t\right] c_{\mathrm{g}}(\mathbf{r},t) && (1.15) \\ \tilde{c}_{\mathrm{e}}(\mathbf{r},t) &= \exp\left[i(\Delta_{\mathrm{L}} + \frac{\omega_0}{2})t\right] c_{\mathrm{e}}(\mathbf{r},t) && (1.16) \end{aligned}$$

then yield

$$\begin{aligned} i\hbar\partial_t\tilde{c}_{\mathrm{g}} &= \left(-\hbar\frac{\delta}{2} + \frac{p^2}{2M}\right)\tilde{c}_{\mathrm{g}} + \frac{\hbar}{2}\left(\Omega_1 e^{-i\mathbf{k_1}\cdot\mathbf{r}} + \Omega_2 e^{-i\mathbf{k_2}\cdot\mathbf{r}} e^{i\delta t}\right)\tilde{c}_{\mathrm{e}} && (1.17) \\ i\hbar\partial_t\tilde{c}_{\mathrm{e}} &= \left(-\hbar\Delta_{\mathrm{L}} + \frac{p^2}{2M}\right)\tilde{c}_{\mathrm{e}} + \frac{\hbar}{2}\left(\Omega_1 e^{i\mathbf{k_1}\cdot\mathbf{r}} + \Omega_2 e^{i\mathbf{k_2}\cdot\mathbf{r}} e^{-i\delta t}\right)\tilde{c}_{\mathrm{g}}. && (1.18) \end{aligned}$$

For a sufficiently large detuning from resonance, we can neglect spontaneous scattering and simplify these equations by adiabatically eliminating the excited state amplitude [8]. This procedure follows from a comparison of the time or energy scales represented by each of the terms in Eq. (1.18):

$$\begin{aligned} \frac{1}{\hbar}\frac{p^2}{2M} &\approx 1 \text{ MHz (several recoil energies)} \\ \Omega = \frac{\mathbf{d}\cdot\mathbf{E_0}}{\hbar} &\approx 500 \text{ MHz} \\ \Delta_{\mathrm{L}} &\approx 100 \text{ GHz} \end{aligned}$$

Due to the small contribution we can safely discard the kinetic energy term in Eq. (1.18). The largest term in this equation is the first term on the right-hand side. This indicates that the dominant behavior of the solution to this equation is an oscillation with a frequency of Δ_{L}. This time scale is faster than the evolution of Eq. (1.17) and will therefore contribute only with an averaged contribution evolving on the same (slow) time scale as Eq. (1.17). To obtain the averaged contribution one can set $\partial_t \tilde{c}_{\mathrm{e}} = 0$ and solve for $\tilde{c}_{\mathrm{e}}$. Inserting the solution

$$\tilde{c}_{\mathrm{e}} = \frac{1}{2\Delta_{\mathrm{L}}} \left(\Omega_1 \, e^{i\mathbf{k}_1\cdot\mathbf{r}} + \Omega_2 \, e^{i\mathbf{k}_2\cdot\mathbf{r}} e^{-i\delta t} \right) \tilde{c}_{\mathrm{g}} \tag{1.19}$$

into Eq. (1.17) one obtains

$$i\hbar\partial_t \tilde{c}_{\mathrm{g}} = \left[\frac{p^2}{2M} + \hbar \frac{{\Omega_1}^2 + {\Omega_2}^2}{4\Delta_{\mathrm{L}}} - \hbar\frac{\delta}{2} + \hbar\frac{\Omega_1\Omega_2}{4\Delta_{\mathrm{L}}} \left(e^{i(\mathbf{q}\cdot\mathbf{r}-\delta t)} + e^{-i(\mathbf{q}\cdot\mathbf{r}-\delta t)} \right) \right] \tilde{c}_{\mathrm{g}} \tag{1.20}$$

where $\mathbf{q} = \mathbf{k}_2 - \mathbf{k}_1$. The second and third terms on the right side of the equation have no spatial dependence and correspond to an overall energy shift which does not affect the dynamics. Here, we can therefore safely neglect those two terms. This leads to an effective Hamiltonian for an atom in the ground state

$$\begin{aligned} H &= \frac{p^2}{2M} + \hbar\frac{\Omega_1\Omega_2}{4\Delta_{\mathrm{L}}} \left(e^{i(\mathbf{q}\cdot\mathbf{r}-\delta t)} + e^{-i(\mathbf{q}\cdot\mathbf{r}-\delta t)} \right) && (1.21) \\ &= \frac{p^2}{2M} + V_0 \cos\left(\mathbf{q}\cdot\mathbf{r} - \delta t\right) && (1.22) \end{aligned}$$

that contains again the kinetic energy and a spatially dependent potential. The amplitude of the potential term is

$$V_0 = \hbar\frac{\Omega_1\Omega_2}{2\Delta_{\mathrm{L}}}. \tag{1.23}$$

The constant frequency difference δ corresponds to a change of the potential phase which is linear in time. For an arbitrary time dependence of the phase $\phi(t)$, we can generalize the equations above to

$$\begin{aligned} H &= \frac{p^2}{2M} + \hbar\frac{\Omega_1\Omega_2}{4\Delta_{\mathrm{L}}} \left(e^{i(\mathbf{q}\cdot\mathbf{r}-\phi(t))} + e^{-i(\mathbf{q}\cdot\mathbf{r}-\phi(t))} \right) && (1.24) \\ &= \frac{p^2}{2M} + V_0 \cos\left(\mathbf{q}\cdot\mathbf{r} - \phi(t)\right), && (1.25) \end{aligned}$$

where the instantaneous frequency difference is

$$\delta(t) = \frac{d\phi}{dt}. \tag{1.26}$$

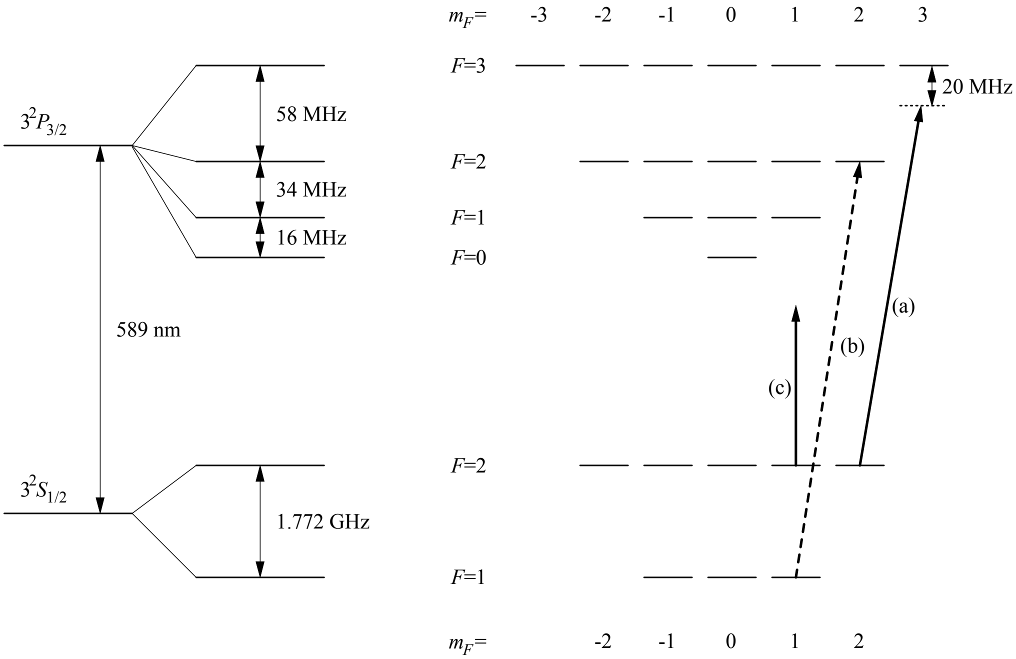

Figure 1.1: Term diagram for the sodium D_2 line. The nuclear spin of sodium is $I = 3/2$, and so the ground state of sodium $3S_{1/2}$ has two hyperfine levels $F = 1, 2$. For the $3P_{3/2}$ excited state we have $J = 3/2$ so that $F = 0, 1, 2, 3$. The $2F + 1$ magnetic sublevels are also shown. Representative examples of (a) the cooling and trapping light, (b) the optical pumping sideband, and (c) the far-detuned optical lattice light are shown as arrows.

The expression for the well depth V_0 contains the resonant Rabi frequencies Ω_1 and Ω_2. The calculation of these frequencies is complicated by the fact that sodium is by no means a system with a two-level structure, as can be seen in the term diagram for the levels contributing to the sodium D_2 line in Fig. 1.1. However, several factors make a determination of the well depth possible. Our initial condition (before the atoms interact with the light) is such that almost all atoms populate the hyperfine $F = 2$ level in the lower manifold. For linearly polarized light, all of the (nearly) degenerate m_F levels experience the same level shift in the far detuned regime. Therefore the entire sample experiences the same effective potential [2, 10]. The actual dipole coupling for a particular ground state sublevel $|F\ m_F\rangle$ is obtained by summing over its couplings to all of the available excited states. When the detuning is large compared to the excited state frequency splittings, all of the excited states participate, and the detuning for each excited state is approximately the same. In addition, the dipole coupling summed over all excited states and all polarizations is independent of the m_F sublevel considered [10, 11]. Because of the spherical symmetry of the dipole operator, the three Cartesian components in this sum are equal and therefore the effective dipole coupling for the case of linearly polarized light and large detuning, regardless of the ground state population, is one third the square of the dipole matrix element for the full D_2 ($J = 1/2 \leftrightarrow J' = 3/2$) transition

$$|d_{\text{effective}}|^2 = \frac{e^2|D_{12}|^2}{3}. \tag{1.27}$$

The dipole matrix element $e^2|D_{12}|^2$ can be obtained from the Einstein A coefficient,

$$A_{21} = \Gamma = \frac{1}{\tau} = \frac{\omega_0^3 e^2|D_{12}|^2}{3\pi\epsilon_0\hbar c^3}\frac{2J+1}{2J'+1}, \tag{1.28}$$

which is related to the radiative lifetime [9]. Here, $J = 1/2$ is the ground state and $J' = 3/2$ is the excited state. The radiative lifetime, $\tau = 16.2$ ns, is known empirically. Using Eqs. (1.27) and (1.28), the effective dipole moment is then

$$d_{\text{effective}} = \sqrt{\frac{\epsilon_0 \hbar \lambda_{\text{L}}^3}{4\pi^2 \tau}} = 1.71 \times 10^{-29}\,\text{C}\,\text{m}. \tag{1.29}$$

The time averaged intensity (defined as the absolute value of the Poynting vector) of a beam of light is related to the amplitude of the electric field by

$$I = \frac{1}{2} c \epsilon_0 E^2. \tag{1.30}$$

Using this relation together with Eqs. (1.8) and (1.23) yields an expression for the well depth in terms of measurable quantities

$$V_0 = \frac{2\pi c^2}{\tau \omega_0^3} \frac{\sqrt{I_1 I_2}}{\Delta_{\text{L}}}, \tag{1.31}$$

where I_1 and I_2 are the intensities of the traveling wave components. If the light beams we consider have a Gaussian intensity profile, then

$$I_{\text{Gauss}}(\rho) = I_0\, e^{-\frac{2\rho^2}{w_0^2}}, \tag{1.32}$$

where ρ is the radial distance from the beam axis. The peak intensity I_0 can then be expressed in terms of the integrated power P_0 over the whole profile as

$$I_0 = 2 \frac{P_0}{\pi w_0^2}. \tag{1.33}$$

Using this relation in Eq. (1.31) yields for the well depth at the center of the beam profile

$$V_0 = \frac{4c^2}{\tau \omega_0^3} \cdot \frac{\sqrt{P_1 P_2}}{w_1 w_2 \Delta_{\text{L}}}. \tag{1.34}$$

1.3.2 Spontaneous emission rate

In deriving the Hamiltonian for our system, we made the assumption that spontaneous emission can be neglected. Since spontaneous emission is the largest source of decoherence, this statement needs to be quantitatively verified. The total spontaneous photon scattering rate is given by the product of the lifetime and the (steady state) excited-state population, $\Gamma\rho_{ee}$. Ignoring collisional relaxation we have for the scattering rate [9, 11]

$$R_{\mathrm{sc}} = \left(\frac{\Gamma}{2}\right)\frac{S}{1+S+4(\Delta_{\mathrm{L}}/\Gamma)^2}, \tag{1.35}$$

where the *saturation parameter* is given by

$$S = \frac{I}{I_{\mathrm{sat}}} = 2\left(\frac{\Omega}{\Gamma}\right)^2. \tag{1.36}$$

The resonant Rabi frequency Ω is defined in Eq. (1.8). Using this definition, the saturation intensity I_{sat} can be expressed as

$$I_{\mathrm{sat}} = \frac{c\epsilon_0\Gamma^2\hbar^2}{4d^2_{\mathrm{effective}}}. \tag{1.37}$$

For a linearly polarized far-detuned light beam we can use the effective dipole matrix element defined in Eq. (1.29) and obtain

$$I_{\mathrm{sat}} = \frac{\pi^2\hbar c\Gamma}{\lambda^3} = 9.39\,\mathrm{mW/cm^2}. \tag{1.38}$$

For a large detuning we can also approximate the scattering rate to be

$$R_{\mathrm{sc}} = \left(\frac{\Gamma}{2}\right)\frac{S}{4(\Delta_{\mathrm{L}}/\Gamma)^2}. \tag{1.39}$$

Using this approximation together with the expression for I_{sat} and the definition of the well depth for equal beam intensities

$$V_0 = \hbar\frac{\Omega}{2\Delta_{\mathrm{L}}} \tag{1.40}$$

from Eq. (1.23), we obtain

$$R_{\mathrm{sc}} \approx \frac{\pi\Gamma}{\Delta_{\mathrm{L}}}\frac{V_0}{h}. \tag{1.41}$$

For typical experimental parameters of $V_0/h = 80$ kHz and $\Delta_{\mathrm{L}} = 2\pi \cdot 40$ GHz we get $R_{\mathrm{sc}} = 60$ s^{-1} or roughly one event every 20 ms. For the tunneling experiments of Chapter 4, where the requirements on the spontaneous emission were the most stringent, the relevant interaction duration (the time of large acceleration) was at most 100 μs. In this time, less than 1% of the atoms scattered a spontaneous photon.

Chapter 2

Experimental Apparatus

2.1 Overview

The experiments on quantum transport and tunneling (Chapters 3 and 4) and recoil-induced resonances (Chapter 5) described in this work have been performed utilizing very similar experimental techniques. Many aspects of the setup are common to all experiments and will be described in this chapter. Details specific to each experiment will be described in the corresponding subsequent chapter.

Three important steps were necessary to perform the experiments described here: the preparation of the initial condition, the generation and application of the interaction potential, and the measurement of the final state of the atoms. To outline the experimental sequence, a simplified schematic is shown in Fig. 2.1. The starting point for the interaction was an atomic cloud that was trapped and cooled in a magneto-optic trap (MOT). The cloud was then further cooled with a stage of molasses cooling. The trapping and cooling fields were then switched off and the interaction beams were turned on. After a typical interaction duration of not more than a few milliseconds, all fields were turned off and the atoms were allowed to expand freely. After expanding for several milliseconds the light beams were again turned on and the spatial location of the atoms was recorded.

During the course of this work, the entire experimental setup underwent

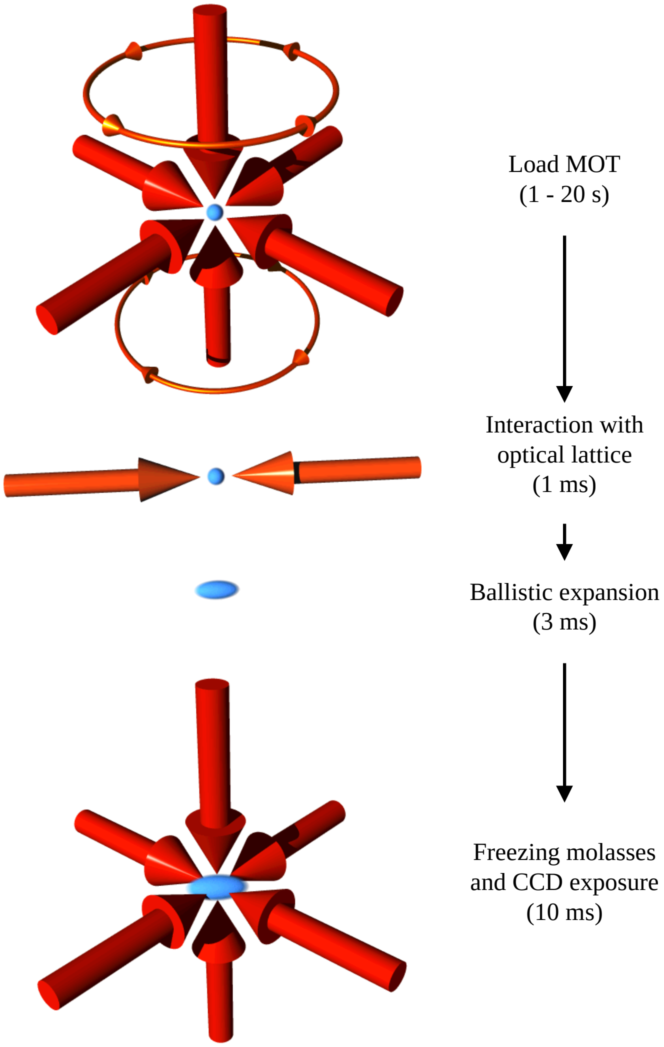

Figure 2.1: Schematic of the experimental sequence. First the atoms are collected and cooled in a magneto-optic trap. The trapping fields are extinguished and the the optical interaction potential is introduced. After interacting with the optical lattice, the atoms are allowed to expand freely in the dark. Finally, the cooling beams are turned on, freezing the atoms in place, and the fluorescence is imaged onto a charge-coupled device (CCD) camera.

radical changes. The apparatus which was used for the quantum transport experiments described in Chapter 3 was completely disassembled and replaced by a new system designed to accommodate the necessary tools and techniques to perform experiments investigating the quantum reflection of ultra-cold atoms from surfaces [12, 13]. For this purpose a much colder atomic sample will be prepared via evaporative cooling in a magnetic trap [14]. With the method of accelerating lattices described in Chapter 3, these atoms can be accelerated without increasing their momentum spread. They will be launched on a ballistic trajectory towards a prism. A blue detuned laser undergoing total internal reflection inside the prism creates a repulsive potential that decays exponentially from the surface. This combines with the attractive atom-surface potential to form a potential barrier, from which the incoming atoms can be reflected. Optionally, nanofabricated surfaces can be used to study the quantum reflection without an evanescent wave. For potentials that vary on the scale of the atomic de Broglie wavelength, a significant reflection probability is expected. The rebuild included the complete vacuum system and optics setup, as well as most of the electronics involved. The computer system underwent a major upgrade and was outfitted with new hardware and software.

The apparatus utilized for the quantum transport experiments is described in detail in the dissertation of Kirk Madison [7] and will not be explained further here. Most of the techniques described there also overlap strongly with the ones described here. The new work on the *Quantum Zeno* and *Anti-Zeno* effects (Chapter 4) and on *recoil-induced resonances* (Chapter 5) was performed utilizing the new setup, which will be described in the following sections. As mentioned above, the current system was designed with further experiments in mind. Many features and techniques of the new design were not necessary for the work described here and were not used. The system is still undergoing changes and many of the parameters were not optimized for maximum performance at the time the data presented here was taken. I will therefore describe only those parts of the setup that were utilized in the recent experiments. A description of the complete system will be deferred to a report of the experiments currently in progress.

2.2 Trapping and cooling

The starting point for all experiments described here was a sample of ultra-cold sodium atoms. In our apparatus, atoms were cooled and trapped in a *double MOT* system. This setup consisted of two spatially separated magneto-optic traps in the standard $\sigma^+ - \sigma^-$ configuration [15, 16]. The motivation for using two traps was to collect more atoms and to have a longer storage time as compared to a single vapor-cell MOT.

The light for both magneto-optic traps was provided by a Coherent 899-21 single-mode CW dye laser pumped by a Coherent Sabre argon ion laser as shown in Fig. 2.2. Typical output power was 1 W single mode using 33% of the 19 W pump power. The laser was actively locked 60 MHz to the blue of the sodium D$_2$ transition $(3S_{1/2}, F = 2) \rightarrow (3P_{3/2}, F' = 3)$ at a wavelength of 589 nm using saturated-absorption FM spectroscopy. The beam providing light for the MOT cycling transition was deflected by an acousto-optic modulator (AOM2) which shifted it down by 80 MHz so that the light incident on the atoms was roughly 20 MHz to the red of the transition. This AOM also provided the means for the intensity control of the light by adjusting its radio-frequency drive power. The frequency-downshifted beam was aligned through a short section of polarization-preserving single-mode fiber. Since the spatial output mode of the fiber was fixed and stable in time, it prevented difficult realignment of the MOT beam setup after performing daily alignment of the laser. The MOT light emerging from the fiber was monitored continuously on a photodiode (power lock PD) and provided the feedback signal necessary to

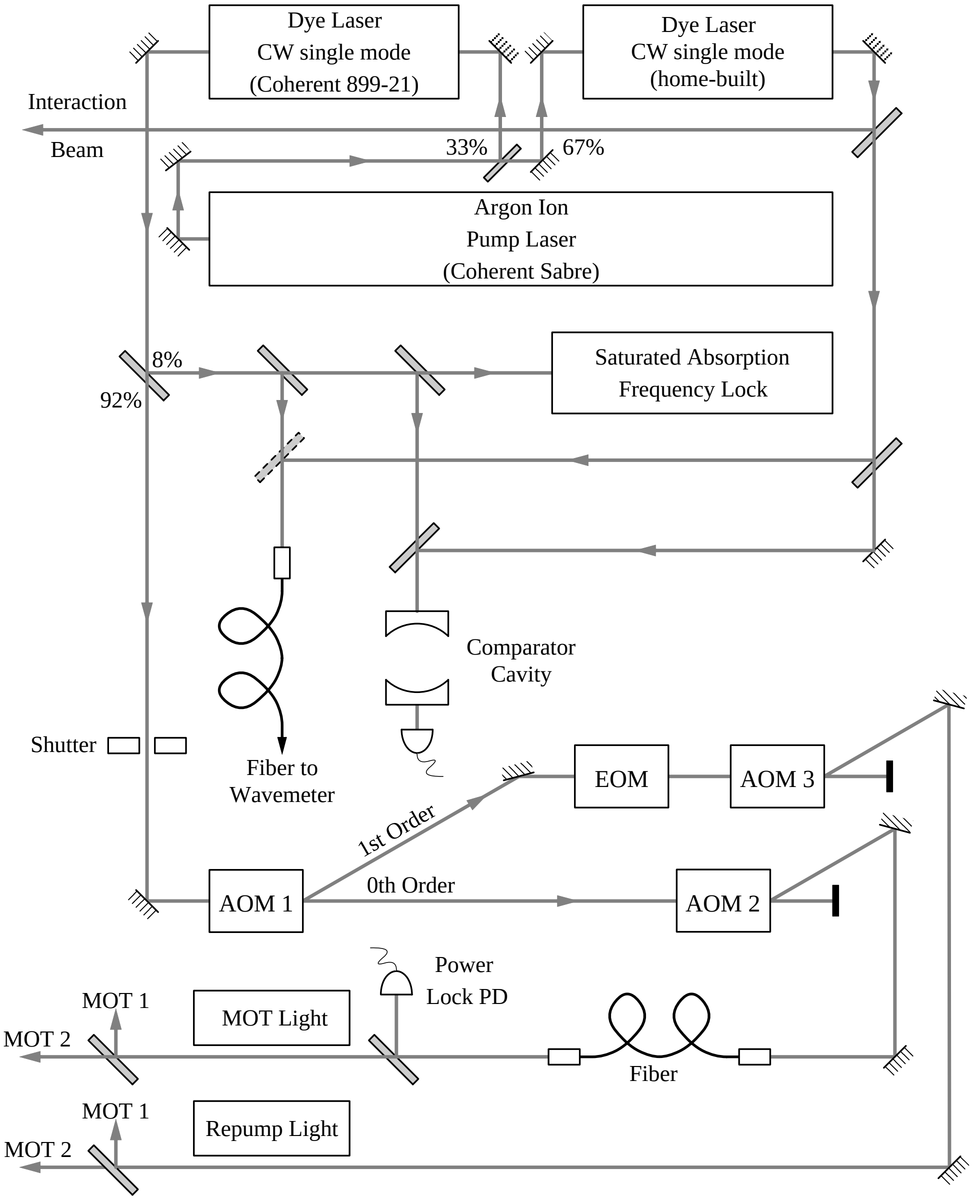

Figure 2.2: Schematic of the laser setup. The argon ion laser pumps two CW single-mode dye lasers. The commercial dye laser (Coherent 899-21) provides the cooling and trapping beams. The home-built dye laser provides the optical lattice interaction beams.

stabilize the output intensity of the fiber by controlling the drive power into AOM2. Residual fluctuations were less than 1% of the average intensity. When the far-detuned optical lattice was on, a *MOT inhibit* signal (see Figures 2.8 and 2.9) disconnected the driver from the modulator (AOM2) to prevent any residual RF leakage that would allow resonant light to reach the atoms during the interaction.

The near-resonant light for the MOT is tuned close to the $F = 2$ ground to $F' = 3$ excited state *cycling* transition; however, it also can populate the $F' = 2$ excited state. If this happens, the atom can either decay back to the $F = 2$ ground state or fall to the $F = 1$ ground state, as can be seen from the term diagram in Fig. 1.1. If it falls to the lower ground state, the interaction with this light stops abruptly since it is now 1.772 GHz (the ground state splitting) away from resonance. In order to prevent this optical pumping into the 'dark' ground state, *repump light* resonant with the $F = 1$ ground to the $F' = 2$ excited state transition was provided. Atoms that fell into the lower ground state were re-excited to the $F' = 2$ excited state where they could fall back to the $F = 1$ state or back to the "correct" $F = 2$ ground state. In order to have independent control of the MOT beam and the repump beam, part of the laser output was deflected by a 270 MHz AOM (AOM1) and the up-shifted portion of the beam was passed through an electro-optic modulator that shifted the maximal amount (about 35%) of the optical power into the first sideband at 1.462 GHz. The upper sideband was then nearly resonant with the $F = 1$ ground to the $F' = 2$ excited state transition. The carrier and the other sidebands were too far from resonance to affect the performance of the MOT. Similar to the main MOT light, the repump beam was then passed through an 80 MHz acousto-optic modulator (AOM3) that provided the intensity control. For this beam no intensity stabilization was employed. Both beams were split in equal amounts to provide light for both traps.

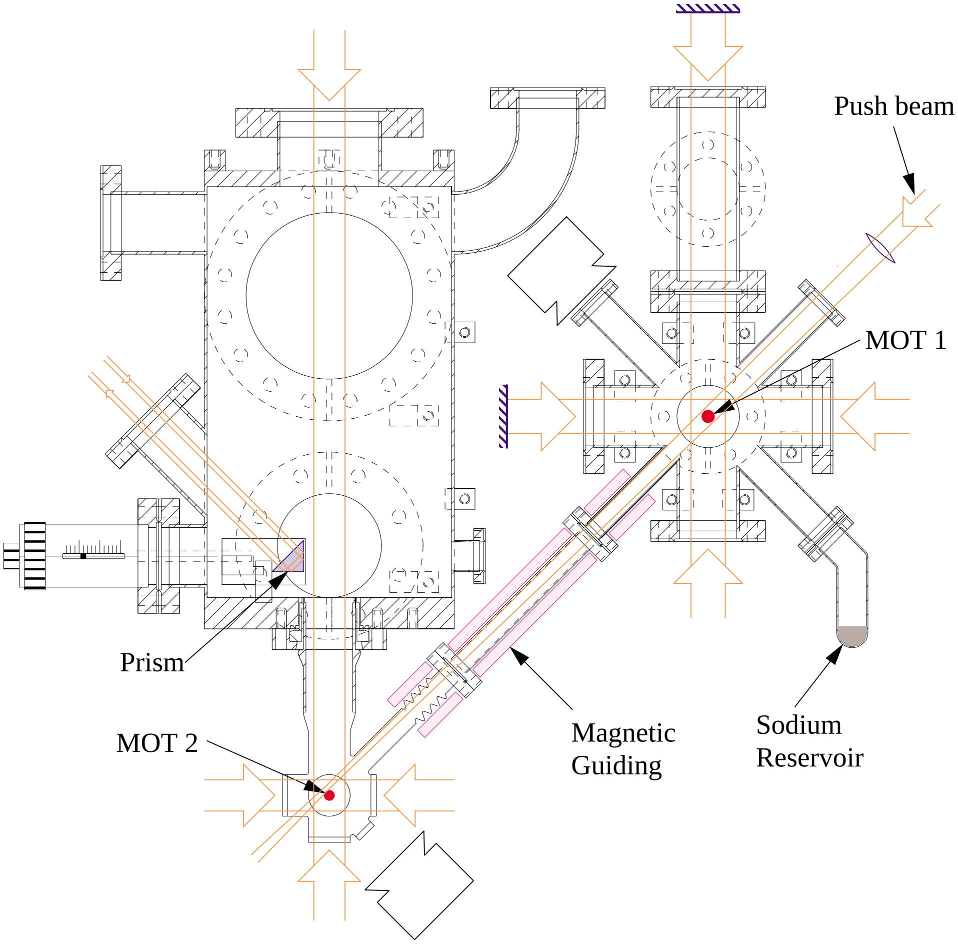

Figure 2.3: Sketch of the double MOT system. Two vacuum chambers are connected via a differential pumping tube (transfer tube). A magneto-optic trap is operated in each chamber. MOT1 is loaded with atoms captured from the vapor phase. A push beam is used to transfer the captured atoms to MOT2 where they are accumulated and cooled further. All experiments were performed at the location of MOT2. The prism indicated in the main chamber is not currently used. It was included for future experiments on quantum reflection of cold atoms from surfaces.

A sketch of the vacuum chamber is displayed in Fig. 2.3. The two magneto-optical traps are located in different parts of the chamber which are connected through a differential pumping section.

In the first (upper) MOT of the 'double MOT' system, atoms are collected directly from the vapor phase. The partial pressure of sodium in the first chamber was increased over the room temperature value by heating the sodium reservoir to about 100 °C. A 20 l/s ion pump was used to maintain high vacuum in the chamber. The MOT, in a standard $\sigma^+ - \sigma^-$ configuration, was formed by intersecting six circularly polarized laser beams at the center of the chamber. In addition, two current-carrying coils in an anti-Helmholtz configuration were placed around the chamber to provide a magnetic field gradient with a zero point in the magnetic field that coincided with the intersection of the six beams. Approximately $5 \cdot 10^6$ atoms were trapped when the MOT was maximally loaded. After collecting enough atoms the MOT cycling light was turned off. A short pulse of near-resonant light was imposed onto the atoms along the direction of the transfer tube as indicated in Fig. 2.3. This push pulse accelerated the atoms in the direction of the second MOT where the atoms were recaptured. The duration of the push pulse, and therefore the resulting final velocity of the atoms leaving the upper MOT region, was adjusted to maximize the transfer efficiency between the two traps. If the velocity was chosen too low, the atoms were not able to traverse the transfer tube due to the gravitational sag and would hit the inside of the tube. If, on the other hand, the velocity was too high, the capture velocity of the second MOT was exceeded and the atoms were too fast to be re-trapped. A further complication was the transverse velocity spread of the atoms perpendicular to the transfer axis. The initial finite temperature as well as heating during the push contributed to the spread. To prevent the atoms from hitting the transfer tube due to the transverse expansion, magnetic guiding along the tube was employed. The atoms, which were optically pumped into the state with maximum magnetic moment during the push, were guided through the transfer tube by a magnetic hexapole field created by permanent magnets along the tube. Even though in a comparable system with Rubidium a transfer efficiency near unity has been reported [17], our efficiency was limited to about 10%. Due to mechanical constraints of the vacuum chamber a continuous arrangement of magnetic material along the entire transfer tube was not possible. This left segments along the tube without a guiding field. We attribute the low transfer efficiency to incomplete guiding caused by regions of low magnetic field between the magnet arrangement. Design changes to improve the magnetic guiding are currently under way.

In the main vacuum chamber a background pressure of approximately $5 \cdot 10^{-11}$ torr was maintained by a 65 l/s ion pump in combination with a titanium sublimation pump. Good optical access was ensured by operating the MOT in an all-optical quartz cell attached to the main chamber. Retrapping of the transferred atoms was achieved using a 'dark spot' MOT in the $\sigma^+ - \sigma^-$ configuration [18]. In this type of MOT the central region of the repump beam is blocked by a round obstacle whose shadow is imaged onto the MOT region. This leaves the central part of the MOT region illuminated only with the MOT 'cycling' light. As described above, the absence of the repump light forces the atoms to be optically pumped into the lower hyperfine state. Since for atoms in that 'dark' state the interaction with the MOT light is negligible, light-assisted collisions are strongly suppressed. Storage times in the lower MOT longer than 60 s were achieved using this technique. Since the upper MOT had a load time much shorter than this storage time, multiple transfers of atoms to the lower MOT were possible. To maximize the average load rate, atoms trapped in the upper MOT were transferred after a load time of 1 s, at which point about $3 \cdot 10^6$ atoms were captured. About 10% of the accumulated atoms were recaptured in the lower MOT after each push.

To outline the different trapping and cooling stages in the lower MOT, a timing diagram of the core elements in the experimental sequence is provided in Fig. 2.4. The atoms stored in the dark MOT are confined by the boundary of the dark spot in the repump beam. To temporarily increase the density of the stored atoms, a repump beam without a dark spot was superimposed with the light beams after the number of desired loads had been performed. This provided spatial confinement in a conventional MOT. Additional spatial compression with the cost of an increase in temperature was achieved by ramping up the magnetic field gradient of the trapping field [19]. To compensate for this temperature increase, a molasses cooling stage was performed following the compression. During this stage the anti-Helmholtz magnetic trapping fields were extinguished and the light intensity was reduced. The temperature of the atoms was reduced by the polarization gradient cooling process [20]. This seemingly counterproductive procedure of first compressing while heating the cloud and then cooling while letting it expand does, however, lead to an increase in overall phase space density.

For the experiments described in the following chapters a large number of trapped atoms was not crucial. To allow for a high repetition rate of the experiment, the number of loads into the lower MOT was typically not larger than five loads. Optionally the regular (bright) MOT could be loaded directly, bypassing the ‘dark MOT’ stage, as was done for the quantum tunneling experiments. Even though fewer atoms were loaded, the experimental sequence simplified substantially. Loading into the dark MOT typically resulted in a cloud of $1.5 \cdot 10^6$ atoms with a final Gaussian distribution with a width of $\sigma_x = 0.35$ mm in position and $\sigma_p = 8\,\hbar k_\mathrm{L}$ in momentum, where $\hbar k_\mathrm{L}$ is the momentum of a single photon of resonant light. For the direct load into the bright MOT the atomic cloud had a typical width of $\sigma_x = 0.3$ mm in position

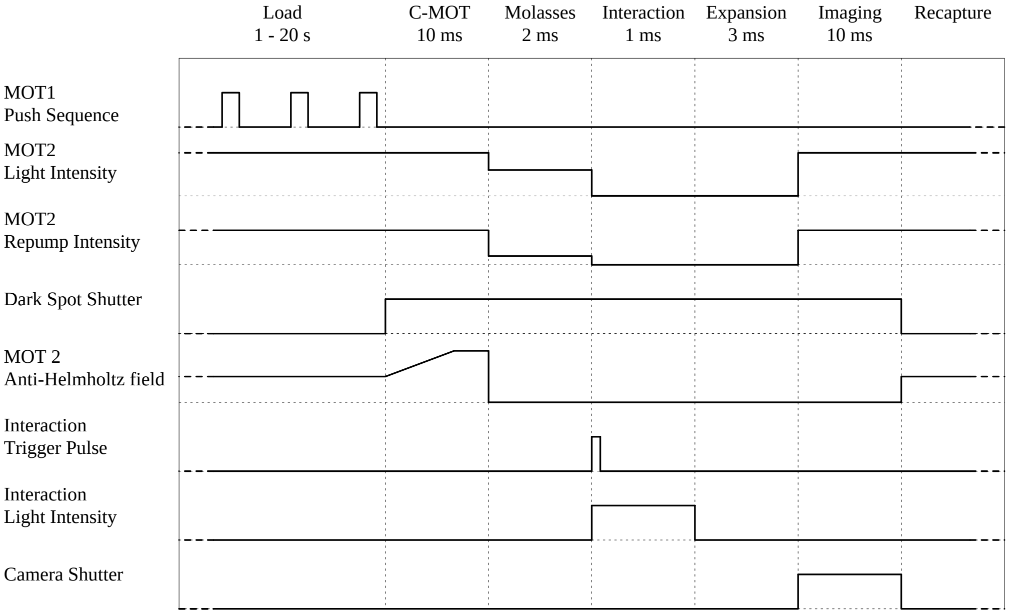

Figure 2.4: Timing diagram for the loading, trapping and cooling sequence as well as the detection following the interaction. The lower MOT in the 'dark spot' configuration is loaded multiple times with atoms from the upper MOT. A repump beam without the dark spot is turned on and the magnetic field gradient is increased to spatially compress the atomic cloud (C-MOT). By suddenly switching off the anti-Helmholtz magnetic field coils and reducing the intensity of the trapping light, the atoms are further cooled. Then the resonant light is turned off and the interaction beams are introduced. After the interaction period the atoms are allowed to expand ballistically in the dark, after which time the cooling beams are turned on, freezing the atoms in place. At this point a picture of the atomic distribution is taken by imaging the fluorescence onto a CCD camera.

and $\sigma_p = 6\,\hbar k_\mathrm{L}$ in momentum, containing about $3 \cdot 10^5$ atoms.

2.3 Interaction

The interaction beams were generated by a home-built dye laser based on a design by Jim Bergquist at NIST in Boulder, CO [21]. This laser was also pumped by the Coherent Sabre argon ion laser, as shown in Fig. 2.2. Typical output power was 1 W single mode using 66% of the 19 W pump power. The wavelength was monitored with a NIST LM-11 wavemeter and was stabilized using the Hänsch-Couillaud lock scheme [22]. The invar reference cavity used in this locking scheme drifted less than 100 MHz per hour, which is a very small amount compared to the typical 40 GHz detuning. The frequency could also be measured relative to the cycling transition of the MOT by coupling both lasers into the same Fabry-Perot monitor cavity. However, with this method the frequency difference could only be determined modulo the free spectral range of the cavity (1.5 GHz).

The optical potential was formed by overlapping two linearly polarized traveling waves with parallel polarization vectors. Both beams were derived from the same laser in order to reduce sensitivity to frequency fluctuations originating in the laser. A schematic of the setup is shown in Figure 2.5. The overall power of the beams was adjusted by a 40 MHz acousto-optic modulator (AOM4). The frequencies of the two beams were controlled independently by two acousto-optic modulators (AOM5 and AOM6). During the tunneling experiments described in Chapter 4 the atoms needed to be accelerated to a velocity of up to 3 m/s. This corresponds to $100\,v_\mathrm{r}$, where v_r is the single photon recoil velocity of the atom. To reach this velocity, the counter-propagating beams need to differ in frequency by 10 MHz. During the experiment the frequency difference needed to be adjusted from zero to this maximum value without misalignment. For this reason a double-pass AOM

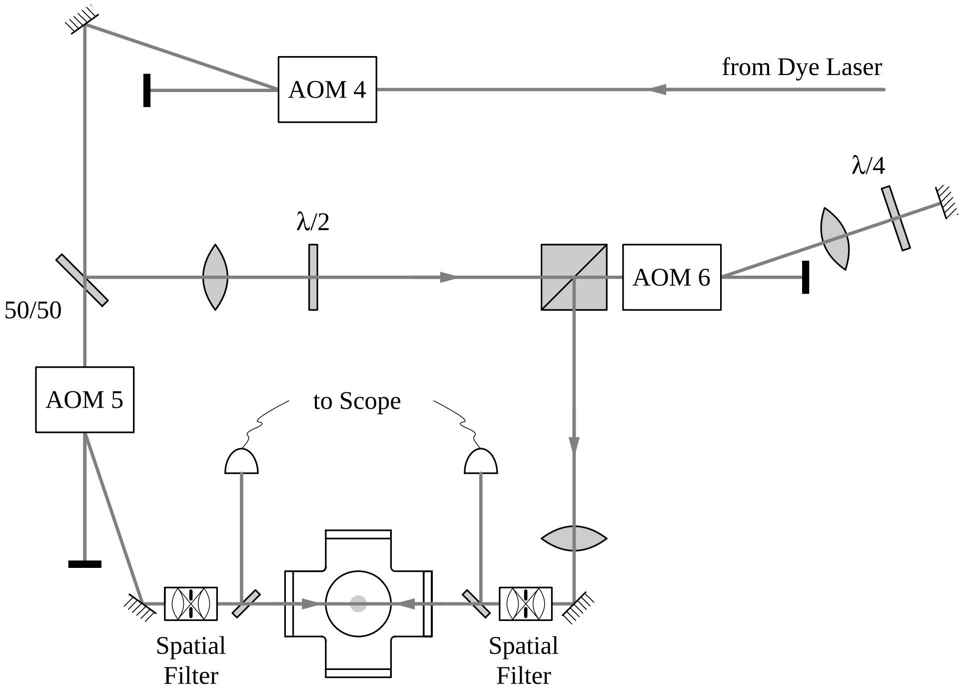

Figure 2.5: Schematic of the interaction beam setup. AOM4 (40 MHz) provides the global control of the intensity. AOM6 is a double-passed, 40 MHz AOM shifting the beam frequency down by twice its drive frequency without leading to an appreciable angular deflection. AOM5 is in the single-passed configuration shifting down the beam frequency by 80 MHz.

setup was chosen. The frequency of the double-passed beam was scanned whereas the frequency of the counter-propagating beam was held constant. The beam in the variable frequency arm of the arrangement was focused by a lens of focal length $f = 500$ mm through the acousto-optic modulator (AOM6) operating at $(40 \pm \Delta\nu)$ MHz. An identical lens was placed 500 mm after the AOM in the first order diffracted beam. The undeflected portion of the beam was discarded. After being reflected by a mirror the diffracted beam retraced its path through AOM6 and was diffracted again in the same manner. The beam was deflected twice on its path back and forth through the AOM and the frequency was therefore down-shifted by twice the drive frequency. Any change in the drive frequency of AOM6 led to an angle change of the first order diffracted beam. By choosing this particular setup, the beam completing both passes through the AOM was still overlapped with the incoming beam regardless of the deflection angle. To separate the backreflected from the incoming beam the polarization was rotated along the path with a quarter-wave plate $(\lambda/4)$ so that a polarization beam splitter cube could be used for separation. To compensate for the frequency offset of 80 MHz introduced by AOM6, the frequency in the second arm was down-shifted by AOM5, also by 80 MHz. The frequency difference between both beams was therefore $(2 \cdot \Delta\nu)$ MHz. After passing through the acousto-optic modulators each beam was spatially filtered. The resulting transverse beam intensity profiles could be approximated by a Gaussian

$$I_{\mathrm{Gauss}}(\rho) = I_0 \, \exp\left(-\frac{2\rho^2}{w_0^2}\right), \tag{2.1}$$

where ρ is the radial distance from the beam axis. A typical value of w_0 in the quantum transport and tunneling experiments was about 2 mm. In the recoil-induced resonance experiments w_0 was in the range of $200\,\mu\mathrm{m} - 400\,\mu\mathrm{m}$. The size and divergence of the beams were matched to avoid transverse spatial interference fringes, which could have created local variations of the well depth.

A small part of each beam was diverted onto a photodiode and the signal was captured on a digitizing oscilloscope during the experiment. The photodiodes were calibrated by measuring the power in the beams with a power meter before entering the interaction region while recording the photodiode voltage. Comparing the power meter to a NIST traceable reference, a calibration with an accuracy of 10% was achieved. Analysis of the photodiode signals provided a means of determining the power in each beam during the interaction and was used for post-selection of the data. The well depth was calculated using Eq. (1.34). Runs for which the well depth was not within a certain window due to laser intensity fluctuations, could be re-taken or simply discarded.

2.4 Detection

After the interaction the light beams were turned off and the atoms were allowed to expand freely. During this period of ballistic expansion, each atom moved a distance proportional to its velocity. This allowed us to determine the velocity distribution by recording the spatial distribution of the atomic cloud. For this purpose the resonant light was turned on after the free drift period to produce a viscous optical molasses that halted the ballistic motion of the atoms and provided spontaneously scattered resonant light for detection. This light was imaged onto a charge-coupled device camera (CCD) to obtain the desired spatial information. Although the atomic cloud expansion in the optical molasses can be made to be spherically symmetric and slow compared to the exposure time, the MOT beams have a Gaussian profile with a finite size (typically 2 cm in diameter). Since the beam intensity decreases with the distance from the center of the chamber the atomic fluorescence will also decrease. In order to correct for this effect, we characterized the fluorescence as a function of position. For this purpose a certain fraction of the atoms was accelerated to a particular velocity as described in Chapter 3. During

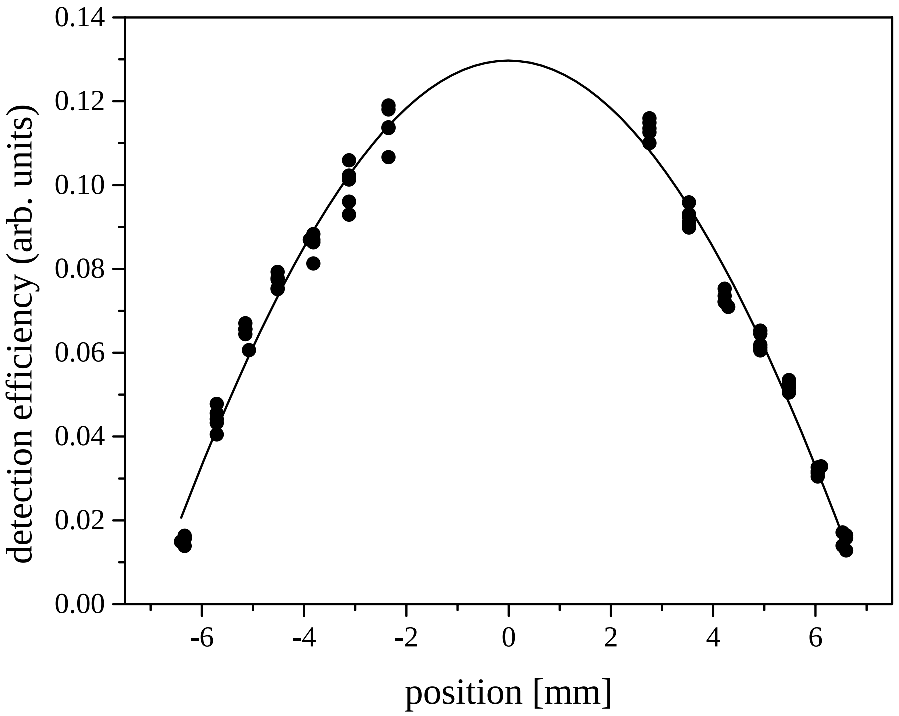

Figure 2.6: A typical detection efficiency envelope of the freezing molasses. The horizontal scale denotes the horizontal position within the detection beams. The line represents a Gaussian fit which was then used to scale the one-dimensional integrated line shapes.

a fixed drift time the atoms traveled a certain distance away from the rest of the atomic cloud. The resulting distribution was imaged and the relative fluorescence of the two subsets of atoms was determined. By varying the initial launch velocity the entire width of the beam could be mapped out and calibrated. In this way, we obtained an empirical measure of the detection efficiency. An example of a typical detection efficiency envelope is shown in Fig. 2.6. The fluorescence profiles acquired during the experiments were then scaled by this function before the distribution was analyzed.

2.5 Control of the experiment

In order to perform the experiments many devices had to be controlled and synchronized with great precision. A variety of parameters had to be adjusted and the resulting changes had to be analyzed and documented. To handle all these tasks the control sequence was fully automated. The core of the control was a PC equipped with multiple National Instruments (NI) data acquisition boards. A layout grouped by functionality is shown in Fig. 2.7. All of the programming was performed in the 'ANSI-C' language within the NI LabWindows/CVI environment. Including the library interfaces that had to be written for various devices, the total number of program lines amounted to a mere 23,000 lines of code.

All of the time-critical sections of the experimental sequence were controlled with the digital pattern generation board (NI PCI-DIO-32HS) which could be pre-programmed and triggered externally. It provided trigger and timing signals to most external devices with a time resolution of 100 ns. Digital signals that were not time-critical were generated with the interrupt-driven digital output board (NI PC-DIO-24). A multi-function I/O board (NI PCI-6024E) was used to read in slowly varying analog signals during the experiment. External, programmable arbitrary-function generators were used to

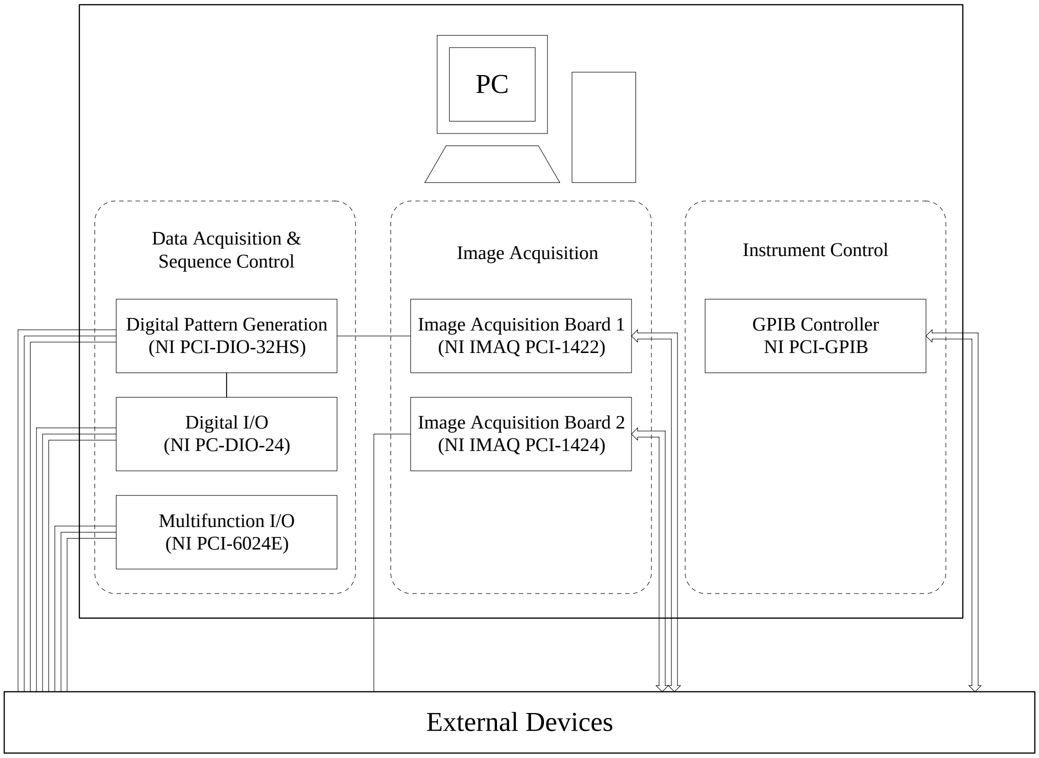

Figure 2.7: Schematic of the computer controlling the experiment. The 200 MHz PC was equipped (via a PCI expansion chassis) with a variety of data acquisition, image acquisition and communication cards from National Instruments. Programming was done using the LabWindows/CVI environment.

output analog signals. These devices were programmed using the GPIB protocol via an NI PCI-GPIB controller card. Analog signals for the MOT light and magnetic fields were provided by two Tektronix AWG 5105 arbitrary function generators, whereas the signal that controlled the frequency of AOM6 in the interaction setup was created using Stanford Research Systems DS345 function generators. Two of those generators were used in conjunction to increase the voltage and timing resolution.

Several charge-coupled device (CCD) cameras were utilized to capture the spatial distribution of atoms during the experiment. To measure the temperature and number of atoms in the upper (MOT1) and the lower (MOT2) magneto-optic traps, two digital cameras (Pulnix TM 9701) with an 8-bit resolution were used. Both were controlled and read out by NI image acquisition boards. In order to capture the spatial distribution of the atoms after the interaction, a higher resolution camera system was necessary. For this purpose we used a Princeton Instruments (PI) 12-bit cooled CCD camera which was controlled by a PI ST-135 controller via the GPIB interface. Background subtraction was employed to reduce unwanted signals due to stray or room light.

Simplified control hierarchies for the electronics controlling the lower MOT and the interaction beams are shown in Fig. 2.8 and Fig. 2.9, respectively.

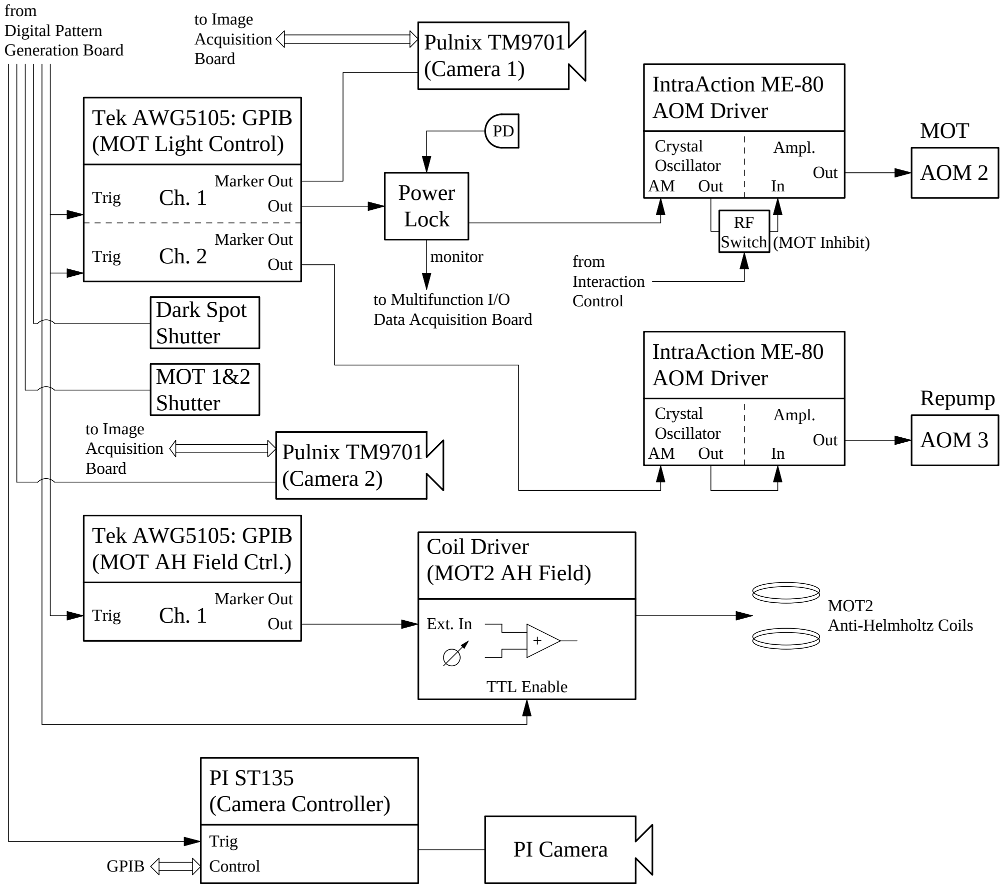

Figure 2.8: Simplified schematic of the devices involved in controlling the lower MOT (MOT2). Timing signals were created with the digital pattern generation board. Arbitrary function generators were utilized to control the intensity of the trapping light and the strength of the necessary magnetic fields. CCD cameras recorded the spatial distribution of the atoms.

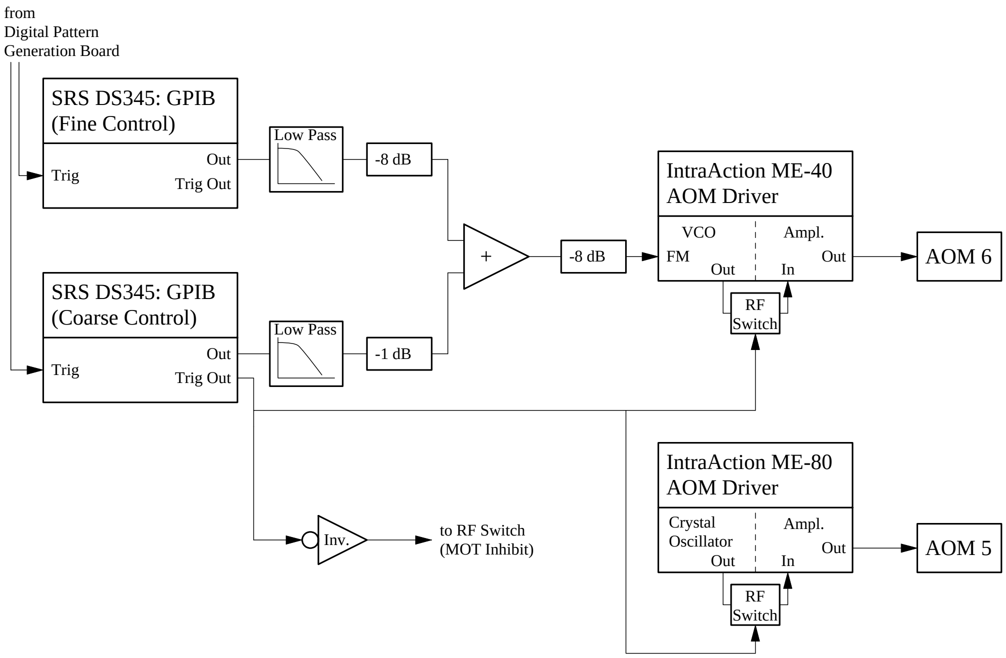

Figure 2.9: Simplified schematic of the devices involved in controlling the interaction beams. The outputs of two arbitrary-function generators operating with different clock rates were added with an appropriate attenuation in order to increase the voltage and timing resolution. This signal served to adjust the frequency difference between the two arms of the interaction beam setup. The intensities of the beams could be extinguished quickly by disconnecting the drive sources from the AOM amplifiers with TTL-controlled RF switches.

Chapter 3

Quantum transport

The system of ultra-cold atoms in a periodic optical potential offers a unique means of studying solid state effects with quantum optics tools. In order to gain insight into the possibilities for experiments, some of the basic properties of this system will be reviewed. A thorough treatment of the fundamental properties can be found in many solid state textbooks, such as Ashcroft and Mermin [23] or Marder [24]. The specifics of our system are described more thoroughly by Madison [7].

3.1 Stationary lattice

As described in Chapter 1 we created the optical potential by spatially overlapping two traveling light beams. For the quantum transport experiments we chose the beams to be counterpropagating ($\mathbf{k}_\mathrm{L} \equiv \mathbf{k}_2 = -\mathbf{k}_1$), which yields $\mathbf{q} = \mathbf{k}_2 - \mathbf{k}_1 = 2\mathbf{k}_\mathrm{L}$. Choosing the same frequency for both beams ($\delta = 0$) simplifies the effective Hamiltonian in Eq. (1.22) to

$$\begin{aligned} H &= \frac{p^2}{2M} + \frac{V_0}{2}\left(e^{2i\,\mathbf{k}_\mathrm{L}\cdot\mathbf{r}} + e^{-2i\,\mathbf{k}_\mathrm{L}\cdot\mathbf{r}}\right) && (3.1)\\ &= \frac{p^2}{2M} + V_0\cos\left(2\mathbf{k}_\mathrm{L}\cdot\mathbf{r}\right) && (3.2)\\ &= \frac{p^2}{2M} + V_0\cos\left(2k_\mathrm{L}x\right), && (3.3)\end{aligned}$$

assuming that beam propagation is along the x-axis.

This form of the Hamiltonian is a textbook example for a particle placed in a spatially periodic potential, and many general properties of this system can be derived by symmetry arguments alone. The most fundamental properties are expressed in *Bloch's theorem.* It states that the eigenstates $\psi(x)$ of this Hamiltonian take on the form of a plane wave multiplied by a function $u(x)$ with the periodicity $d = \frac{\pi}{k_\mathrm{L}} = \frac{\lambda}{2}$ of the potential:

$$\psi_{n,k}(x) = e^{ikx} u_{n,k}(x), \tag{3.4}$$

where

$$u_{n,k}(x+d) = u_{n,k}(x) \tag{3.5}$$

and k is the quasi-momentum of the particle. The index n is called the *band index* and appears in Bloch's theorem because for a given k there are many solutions to the Schrödinger equation. An important consequence of Bloch's theorem is that the wave functions and the energy dispersion of the particle are periodic in quasi-momentum (reciprocal) space

$$\begin{aligned} \psi_{n,k+K}(x) &= \psi_{n,k}(x) && (3.6) \\ E_n(k+K) &= E_n(k), && (3.7) \end{aligned}$$

where $K = \frac{2\pi}{d} = 2k_\mathrm{L}$ is the periodicity in reciprocal space. Another property of paramount importance concerns the mean velocity of a particle in a particular Bloch state $\psi_{n,k}$. It can be shown that the velocity is determined by the energy dispersion relation as

$$v_n(k) = \frac{1}{\hbar} \frac{\partial E_n(k)}{\partial k}, \tag{3.8}$$

in analogy to the free particle case [23].

The problem of finding the energy eigenstates of H, that is solving $H|\psi\rangle = E|\psi\rangle$, is equivalent to solving Mathieu's equation, whose properties and solutions can be found in most handbooks of mathematical functions [25].

A numerical method of calculating the eigenvalues and eigenfunctions is described in Appendix A. Using these routines, sample dispersion curves (energy versus the quasi-momentum k) are calculated and plotted in Fig. 3.1

For a vanishing well depth V_0 the dispersion curve is the free particle energy parabola $E(k) = \frac{\hbar^2 k^2}{2M}$. To make the connection to the repetitive nature of the band description in Eq. (3.7) for finite V_0, the parabola is repeatedly plotted at multiples of the reciprocal space period in the left panels of Fig. 3.1(a). Since this is a highly redundant picture, the curves are conventionally restricted to the fundamental period in reciprocal space (the first Brillouin zone), as indicated in the right panels of the same figure. Higher branches of the dispersion curves are assigned successive band indices. For finite well depth V_0, the lowest crossing points of the free energy parabolas at $k = \pm k_{\mathrm{L}}$ develop a level repulsion due to the coupling of the levels by the potential term. The amount of repulsion in this *avoided level crossing* can easily be estimated by first order degenerate perturbation theory. The unperturbed eigenstates of the momentum operator at the first crossing are plane waves

$$\psi_1 = e^{ik_{\mathrm{L}}x} \tag{3.9}$$

$$\psi_2 = e^{-ik_{\mathrm{L}}x}. \tag{3.10}$$

Since these states become coupled by the potential term, they will in general no longer be eigenstates of the full Hamiltonian. We try to find new eigenstates that are linear combinations of ψ_1 and ψ_2,

$$\Psi = a\psi_1 + b\psi_2, \tag{3.11}$$

and solve for the solution of

$$H\Psi = E\Psi. \tag{3.12}$$

This leads to the set of equations

$$\begin{pmatrix} H_{11} - E & H_{12} \\ H_{21} & H_{22} - E \end{pmatrix} \begin{pmatrix} a \\ b \end{pmatrix} = 0, \tag{3.13}$$

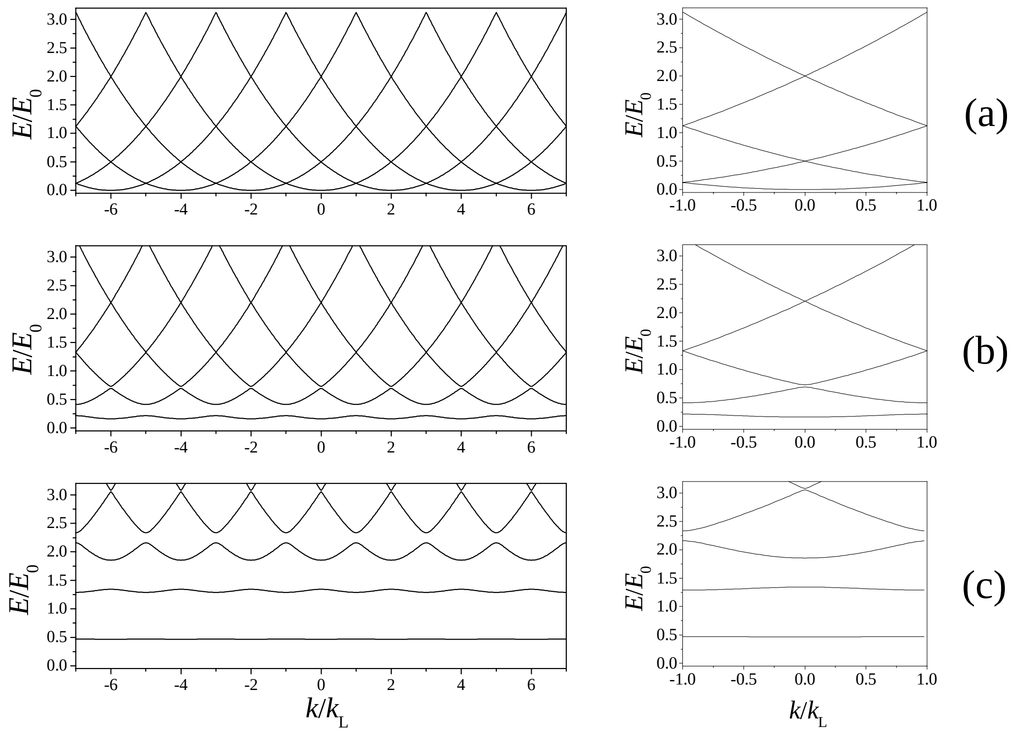

Figure 3.1: Dispersion curves of a particle in a sinusoidal potential. Plotted here are the energy (in units of $E_0 = 8\,\hbar\omega_\mathrm{r}$) versus the quasi-momentum k (in units of k_L) in the repeated-zone scheme (left panels) and in the reduced-zone scheme (right panels). The well depth V_0/h of the potential is (a) 0, (b) 40 kHz and (c) 200 kHz.

where $H_{ij} = \langle \psi_i | H | \psi_j \rangle$. The existence of a solution requires

$$\begin{vmatrix} H_{11} - E & H_{12} \\ H_{21} & H_{22} - E \end{vmatrix} = 0, \tag{3.14}$$

yielding as solutions of the characteristic polynomial

$$E_{1,2} = \frac{1}{2}(H_{11} + H_{22}) \pm \frac{1}{2}\sqrt{(H_{22} - H_{11})^2 + 4|H_{12}|^2}. \tag{3.15}$$

The energy degeneracy of the unperturbed states has been removed by the coupling between them. The matrix elements can immediately be written down using the orthonormality condition of the momentum eigenstates

$$\begin{aligned} H_{11} &= \left\langle \psi_1 \left| \frac{p^2}{2M} \right| \psi_1 \right\rangle = \frac{\hbar^2 k_\mathrm{L}^2}{2M} = H_{22} && (3.16) \\ H_{12} &= \langle \psi_1 | V_0 \cos(2k_\mathrm{L} x) | \psi_2 \rangle = \frac{V_0}{2} = H_{21}. && (3.17) \end{aligned}$$

Inserting these values yields

$$E_{1,2} = \frac{\hbar^2 k_\mathrm{L}^2}{2M} \pm \frac{1}{2} V_0. \tag{3.18}$$

The energy splitting for the first crossing and therefore the width of the first band gap is, to first order in V_0, equal to V_0 itself. The coupling term $\cos(2k_\mathrm{L}x)$ connects only states with a difference in momentum of $2\,\hbar k_\mathrm{L}$. For the calculation of the splitting at higher crossing points we therefore need to resort to perturbation expansions of higher order.

The energy values evaluated at the band edges as a function of the well depth V_0 have been determined numerically for several crossings and are displayed in Fig. 3.2. From this figure one can see that the energy bands evolve from a continuum of allowed energies, for a vanishing well depth, into the linearly spaced discrete energy levels of a harmonic oscillator, in the limit of large well depth.

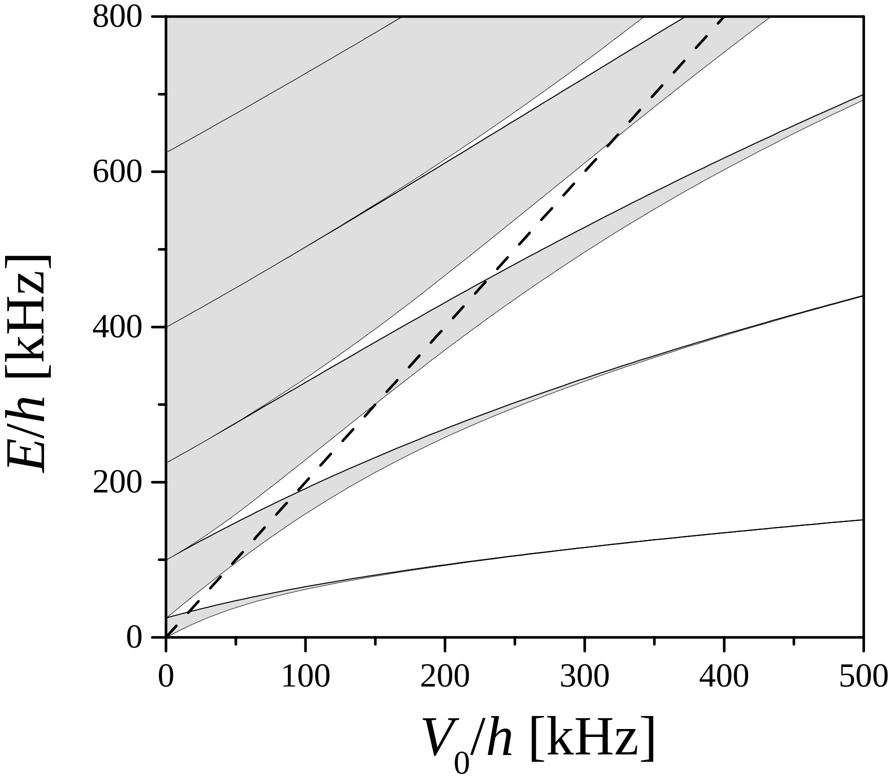

Figure 3.2: Regions of allowed (gray) and restricted (white) energy in the periodic potential as a function of the well depth. The energy is measured relative to the bottom of the well. Indicated as a dashed line is the top edge of the potential ($2V_0$).

3.2 Accelerating lattice

In the previous section we showed that the study of the band structure of an atom in an optical lattice can reveal information about the behavior of electrons in a crystal lattice. Although interesting, these considerations are of limited use if no external influence on the system is considered. For electrons in a crystal lattice the most commonly encountered perturbation is an applied static electric field. This seemingly simple perturbation leads to a very rich system, whose properties were controversial for quite some time. Experimental tests in the field of solid state physics were hindered by decohering processes such as scattering of the electrons on impurities in the crystal lattice or scattering among themselves. These effects are negligible in our atom optics system and we were able to contribute to this field by studying some of the effects previously inaccessible to experiment.

3.2.1 Semiclassical equations of motion

A static electric field, which exerts a strong force on the electrons in a crystal, does not have the desired effect on a neutral atom in an optical potential. However, we can simulate the corresponding force by introducing an appropriate time dependence of the optical lattice. Let us consider an optical lattice composed of two counterpropagating light beams that do not possess the same frequency. As derived in Chapter 1, the effective Hamiltonian for this system is given by

$$H = \frac{p^2}{2M} + V_0 \cos\left(2k_{\mathrm{L}}x - \phi(t)\right), \tag{3.19}$$

where the same assumptions were made as for Eq. (3.3), except for allowing a time dependent phase shift of the standing wave. A constant acceleration of the 'standing' wave pattern is generated by linearly chirping the frequency difference of the counterpropagating beams. This is described by $\phi(t) = k_{\mathrm{L}}at^2$, where a is the acceleration. Inserting this into the equation above yields

$$H = \frac{p^2}{2M} + V_0 \cos\left[2k_{\mathrm{L}}\left(x - \frac{1}{2}at^2\right)\right]. \tag{3.20}$$

To make the connection to the solid state system, one can transform Eq. (3.20) to the frame of reference accelerated with the potential by applying a unitary transformation, following the recipe outlined by Peik et al. [26]. The unitary transformation performs a translation of the position, momentum, and overall energy:

$$U(t) = e^{i\alpha(t)p/\hbar} e^{-i\beta(t)x/\hbar} e^{i\gamma(t)/\hbar}. \tag{3.21}$$

For a time dependent unitary transform the Hamiltonian will be transformed as

$$\tilde{H} = UHU^\dagger + i\hbar\frac{\partial U}{\partial t}U^\dagger. \tag{3.22}$$

A transformation to the accelerating frame is achieved by choosing

$$\alpha(t) = \frac{1}{2}at^2 \tag{3.23}$$

$$\beta(t) = Mat \tag{3.24}$$

$$\dot{\gamma}(t) = \frac{\beta^2}{2M} + \dot{\beta}\alpha. \tag{3.25}$$

Applying this transformation yields

$$\tilde{H} = \frac{p^2}{2M} + V_0 \cos(2k_{\mathrm{L}}x) + Ma\,x. \tag{3.26}$$

The last term containing the mass M of the atom is an inertial term, resulting from the transformation to an accelerating frame of reference. It mimics the role of the interaction potential between an electric field $\mathcal{E}$ and the electron

$$U_{el} = \mathcal{E}e\,x, \tag{3.27}$$

where e is the electric charge of the electron.

Having established this connection, we can directly apply the results for the solid state system to an atom in the accelerated optical potential. A derivation of the semiclassical equations of motion for small electric fields can be found in standard text books [23, 24] and are simply stated here without proof. The equations of motion express the relationship of the state's quasi-momentum (k), band index (n), energy ($E_n(k)$), and mean velocity ($v_n(k)$). By replacing the force $F = e\mathcal{E}$ with $F = Ma$, we obtain the following equations of motion:

1. The band index n is a constant of motion.
2. The evolution of the system is described by

$$\begin{aligned} v_n(k) &= \frac{1}{\hbar}\frac{\partial E_n(k)}{\partial k} && (3.28) \\ \dot{k}_n(t) &= -\frac{1}{\hbar}Ma. && (3.29) \end{aligned}$$

3. The form of the band structure $E_{n,k}$ is unchanged.

The restriction of *small fields*, mentioned above, deserves special attention. The statement that the band index is a constant of motion indicates that inter-band transitions are being neglected in this derivation. However, for larger fields electrons can tunnel across the band gap from one band into the next. An estimate for the field strength is given by Ashcroft and Mermin as $E \ll \frac{E_{\mathrm{g}}^2}{e\hbar v_{\mathrm{F}}}$, with v_{F} being the typical electron velocity in the originating band [23]. In our system this transforms to a condition for the acceleration

$$a \ll \frac{E_{\mathrm{g}}^2}{\hbar^2 k_{\mathrm{L}}} \tag{3.30}$$

where $v_{\mathrm{r}} = \hbar k_{\mathrm{L}}/M$ serves as the typical velocity at the edge of the Brillouin zone. Since for higher band indices the gaps get smaller and the typical velocity gets higher, a dramatic increase in the tunneling probability is to be expected. A more detailed study of the tunneling process across the band gaps will be provided in Chapter 4.

3.2.2 Bloch oscillations and Wannier-Stark states

One remarkable consequence of the equations of motion stated above is that particles exposed to a static field are predicted to oscillate in space rather than increase their velocity steadily. As can be seen by integrating Eq. (3.29), the quasi-momentum increases linearly with time as

$$k(t) = k_0 - \frac{Mat}{\hbar}. \tag{3.31}$$

The velocity of the particle with a given quasi-momentum k is given by Eq. (3.28) as the derivative of the dispersion curve at the point k. Since $E_n(k)$ is oscillatory in reciprocal space and k varies linearly with time, the velocity $v_n(t)$ is oscillatory in time. The period of oscillation τ_B is the time it takes for a particle to traverse the Brillouin zone of width $K = 2k_\mathrm{L}$ and calculates to

$$\tau_\mathrm{B} = \frac{2\hbar k_\mathrm{L}}{Ma} = \frac{2v_\mathrm{r}}{a}. \tag{3.32}$$

A sketch of these *Bloch oscillations* is graphically depicted in Fig. 3.3(a). An atom starting in the lowest band of the potential will increase its quasi-momentum k due to the applied force, as given by Eq. (3.31). As it approaches the edge of the Brillouin zone at a constant rate $\partial_t k$, the velocity decreases as the slope of the dispersion curve decreases. At $k = k_\mathrm{L}$ the derivative $\partial_k E_0(k)$ is zero and according to Eq. (3.28) the particle is at rest. It will then reverse its velocity and continue its motion, until the velocity is reversed again at the next minimum of the dispersion curve. The reversal of its velocity at $k = k_\mathrm{L}$ can be viewed as a first order Bragg reflection of the particle wave by the periodic potential. The arguments above also hold for atoms in higher bands. They oscillate at the same Bloch frequency. However, the velocity reversal in higher bands corresponds to a higher order Bragg scattering process. It is important to note that this reversal of the atomic velocity occurs relative to

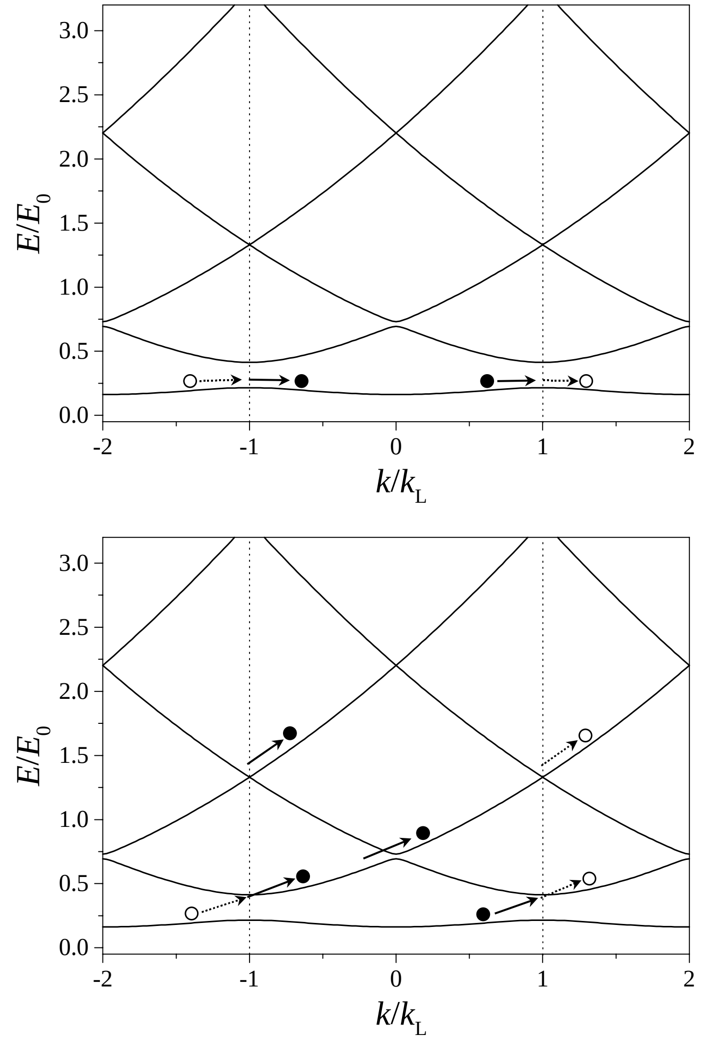

Figure 3.3: Sketch of a particle trajectory in reciprocal space. In part (a) the rate of change of the quasi-momentum is slow enough for the particle to follow the dispersion curve adiabatically across the Brillouin zone boundary. This is equivalent to discontinuing the motion at one edge of the Brillouin zone and emerging from the other side in the same band. Panel (b) illustrates a case for a larger force, where the particle cannot follow the curve and tunnels through the band gap.

the accelerated frame. In the laboratory frame the constant acceleration of the potential is superimposed on the oscillation of the atom.

For a higher field strength (or acceleration, in the atom optics system) the particle might not be able to follow the dispersion curve adiabatically as it approaches the edge of the Brillouin zone. It can cross the band gap and continue its motion in a higher band, as indicated in Fig. 3.3(b). This corresponds to a tunneling process through the band gap, in which case the semiclassical equations stated above no longer hold. For a particle undergoing tunneling, the transformation back to the laboratory frame reveals no change of velocity at all. The particle is simply lost out of the potential and can no longer track the acceleration.

The Bloch bands of an atom in a stationary potential are, by definition, continuous regions in the energy spectrum. Bloch oscillations in an accelerated lattice reveal themselves in the energy spectrum as discrete peaks with an energy separation of $h\nu_{\mathrm{B}}$, where $\nu_{\mathrm{B}} = \frac{1}{\tau_{\mathrm{B}}}$. This is a consequence of the Bloch bands splitting up into discrete *Wannier-Stark states.* A physical interpretation of these states can be obtained by regarding the transition between bands as a temporal interference effect. Quantum mechanically, atoms can tunnel between bands at all positions within the Brillouin zone. Since Bloch oscillations lead to multiple passes through the Brillouin zone, transition amplitudes can interfere constructively or destructively, depending on the rate at which the particle traverses the Brillouin zone. This is in analogy to the optical interference pattern generated by a plane wave of light illuminating an array of slits or a grating. The temporal interference produces sharp resonances spaced at the (temporal) grating period τ_{B}. The more traversals of the Brillouin zone the particle completes, the sharper the resonance becomes. If the particle tunnels out of the band quickly, the resonances are broad, indicating a short lifetime of the associated state. Following the arguments of Krieger and Iafrate [27], one obtains the transition probability $P_{0\to 1}$ from the lowest into the second band after N traversals of the Brillouin zone:

$$P_{0\to 1} \propto \frac{\sin^2(N\beta)}{\sin^2(\beta)}, \tag{3.33}$$

where

$$\beta = \frac{1}{2Ma}\int_{-k_\mathrm{L}}^{k_\mathrm{L}} [E_0(k) - E_1(k)]\, dk \tag{3.34}$$

and we have assumed that the initial population was in the first band. The resonances for the transition occur for $\beta = n\pi$. Defining the average band separation to be

$$\bar{E}_\mathrm{g} \equiv \frac{1}{2k_\mathrm{L}}\int_{-k_\mathrm{L}}^{k_\mathrm{L}} [E_0(k) - E_1(k)]\, dk \tag{3.35}$$

and using

$$\nu_\mathrm{B} = \frac{a}{2v_\mathrm{r}} = \frac{aM}{2\hbar k_\mathrm{L}}, \tag{3.36}$$

we find the tunneling resonance condition to be

$$n\nu_\mathrm{B} = \frac{\bar{E}_\mathrm{g}}{h}. \tag{3.37}$$

This condition indicates the presence of discrete states. The tunneling out of a bound state is enhanced by the presence of a Wannier-Stark state of the same energy, but in a higher band and displaced by one or more lattice sites. This situation is depicted in Fig. 3.4(a).

Krieger and Iafrate also consider the possibility of driving transitions between bands with an external alternating probe field. Assuming that the transition due to the probe drive is the dominant loss process from the first band (neglecting tunneling), they obtain a resonance condition for the drive frequency ν_p

$$\nu_\mathrm{p} = \frac{\bar{E}_\mathrm{g}}{h} + n\nu_\mathrm{B}. \tag{3.38}$$

Here, the driving field provides a direct spectroscopic tool to probe the lattice structure of the Wannier-Stark states by allowing transitions between the states, as indicated in Fig. 3.4(b).

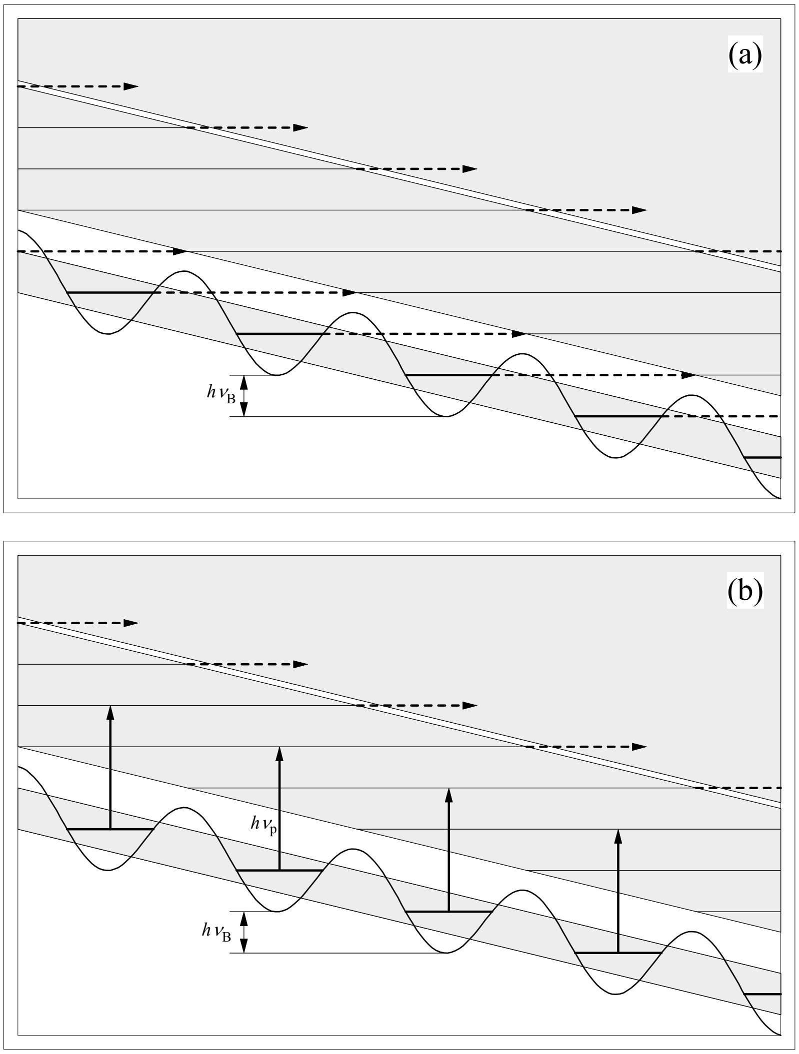

Figure 3.4: Schematic of the Wannier-Stark ladder within the bands. In (a) the tunneling process is indicated. The presence of a Wannier-Stark state in the continuum of the higher band enhances the tunneling probability across the gap. In (b) a weak spectroscopic drive couples the states and introduces transitions. In either case, once an atom is in the second band, it can easily tunnel across successive band gaps into higher bands.

3.3 Band spectroscopy and Rabi oscillations

In Section 2.2 the method of preparing a sample of cold and trapped atoms was outlined. For the experiments described in this chapter [28], the final atomic distribution was approximately Gaussian with a width of $\sigma_x = 0.3$ mm in position and $\sigma_p = 6\,\hbar k_{\mathrm{L}}$ in momentum. However, to be able to study tunneling and transitions between single bands, an initial condition with only one populated band, preferably the lowest, was desired. If we suddenly turn on the optical potential within the molasses distribution, only a fraction of the atoms are transferred into the lowest band [29]. Most atoms will be projected into higher index bands. The location of the bands relative to the potential is indicated in Fig. 3.2. For a typical well depth of $V_0/h = 70$ kHz, we can see that atoms in the lowest band are trapped within the potential wells, whereas atoms in the second band are only partially trapped. Atoms in even higher bands have energies well above the potential and hence are effectively free. The location of the bands with respect to the potential well can be regarded as an indicator for the tunneling rates between bands when an acceleration is applied. Bands that lie entirely within the wells have a much smaller tunneling rate than bands outside the range of the potential. To empty all but the lowest band, we took advantage of this difference in tunneling rates across successive band gaps. After turning on the standing wave, it was accelerated to a velocity of $v_0 = 40\,v_{\mathrm{r}}$, as indicated in Fig. 3.5. During this acceleration the atoms in the first band performed a sequence of Bloch oscillations within the potential and were accelerated in the laboratory frame. Atoms in higher bands could tunnel through the successively smaller band gaps and were lost out of the potential. The transport acceleration a_{trans} was chosen to maximize tunneling out of the second band while minimizing losses from the first trapped band. For typical experimental parameters of $V_0/h = 70$ kHz and $a_{\mathrm{trans}} = 2000\,\mathrm{m/s^2}$, the Landau-Zener expression derived in Chapter 4 for the lifetime of the first

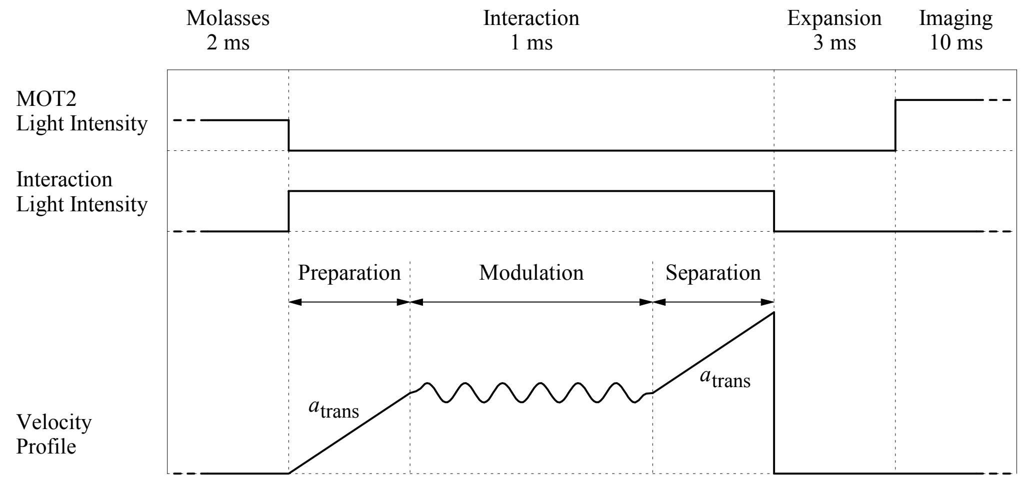

Figure 3.5: Interaction beam timing diagram for the band spectroscopy experiments. After the molasses stage the resonant light is turned off and the optical lattice was turned on. A subset of atoms is projected into the fundamental band and separated in velocity by an acceleration a_{trans}. After this preparation stage, the optical lattice position and amplitude are varied to realize the potential under study. This step is followed by separating the atoms in the lowest band from those in higher bands by the same acceleration a_{trans}. The atoms are then allowed to expand freely in the dark and the spatial distribution is illuminated with the resonant molasses light.

and second band yields 24 ms and 40 μs respectively. This ensured that after 600 μs of acceleration only the first band still contained a significant number of atoms.

After reaching the velocity v_0, the chirp was stopped and the frequency difference was held constant. At that point, a phase modulation at the frequency of ν_{p} was added to one of the two counterpropagating beams forming the standing wave, as indicated in Fig. 3.5. This phase modulation could drive transitions between bands, if the band separation for some value of k was close to $E = h\nu_{\mathrm{p}}$. The modulation was switched on and off smoothly over 16 μs to avoid any discontinuous phase changes in the potential that could induce transition to higher bands. The amplitude of the modulation was chosen to be small enough to not perturb the band structure. For large amplitudes of the modulation the band structure can undergo a *dynamical suppression*, effectively turning off Bloch tunneling. This effect has been observed previously in our system [30]. After a fixed time interval the modulation was turned off and the frequency chirping resumed at a rate corresponding to a_{trans}. This separated in momentum space the remaining trapped atoms in the lowest band from those having made the transition into higher bands. After reaching a final velocity $v_{\mathrm{final}} = 80\, v_{\mathrm{r}}$ the interaction beams were switched off suddenly.

In the detection phase we needed to distinguish three classes of atoms: (1) atoms that were not initially trapped in the lowest band and immediately tunneled out of the well during the initial acceleration, (2) atoms which were trapped in the first band at the beginning of the interaction but were driven out by the modulation, and (3) atoms that remained in the first band during the entire sequence. Since the atoms in different classes had left the trapping potential at different stages of the experimental sequence, they were accelerated to different velocities. Therefore, after drifting in the dark for 3 ms, these classes separated in space and could be distinguished by recording their position. For this purpose the atoms were imaged in the "freezing molasses" as described in Section 2.4. A typical fluorescence image of the atoms is shown in Fig. 3.6(a). The two-dimensional image was then integrated in the direction perpendicular to the axis of the interaction beams to obtain a one-dimensional distribution along the beam direction, containing all three classes of atoms. The corresponding integrated distribution is shown in Fig. 3.6(b). In order to reduce sensitivity to fluctuations of the number of atoms in the MOT, the number of survivors (atoms in class (3)) was normalized by the total number of atoms initially trapped in the first band, which was obtained by summing the contributions of class (2) and class (3). To observe the temporal evolution of the fundamental band population we repeated the experiment for various modulation durations, holding the probe frequency ν_{p} and amplitude m fixed.

The phase modulation added to one of the beams changes the potential term in the Hamiltonian (3.3) to

$$H = \frac{p^2}{2M} + V_0 \cos\left(2k_{\mathrm{L}}x + m\cos[2\pi\nu_{\mathrm{p}}t]\right), \tag{3.39}$$

where ν_{p} is the probe frequency and m is the dimensionless modulation amplitude. The effect of this modulation can be elucidated by expanding the potential for small modulation amplitude m. To first order one obtains

$$V(x,t) = V_0\cos(2k_{\mathrm{L}}x) + V_0\, m\sin(2k_{\mathrm{L}}x)\cos(2\pi\nu_{\mathrm{p}}t). \tag{3.40}$$

The harmonic drive term preserves the periodicity of the lattice and can induce transitions between bands, leaving the quasi-momentum k unchanged.

Figure 3.7 shows the energy bands in the reduced zone scheme for a well depth of $V_0/h = 71$ kHz. As indicated in this figure, the drive frequency ν_{p} can be chosen resonant with the transition between the first two bands ($1 \leftrightarrow 2$), but far from resonance for transitions between successive bands [arrow (a) and (b)] for some value of k. In this case only two eigenstates of the atoms need

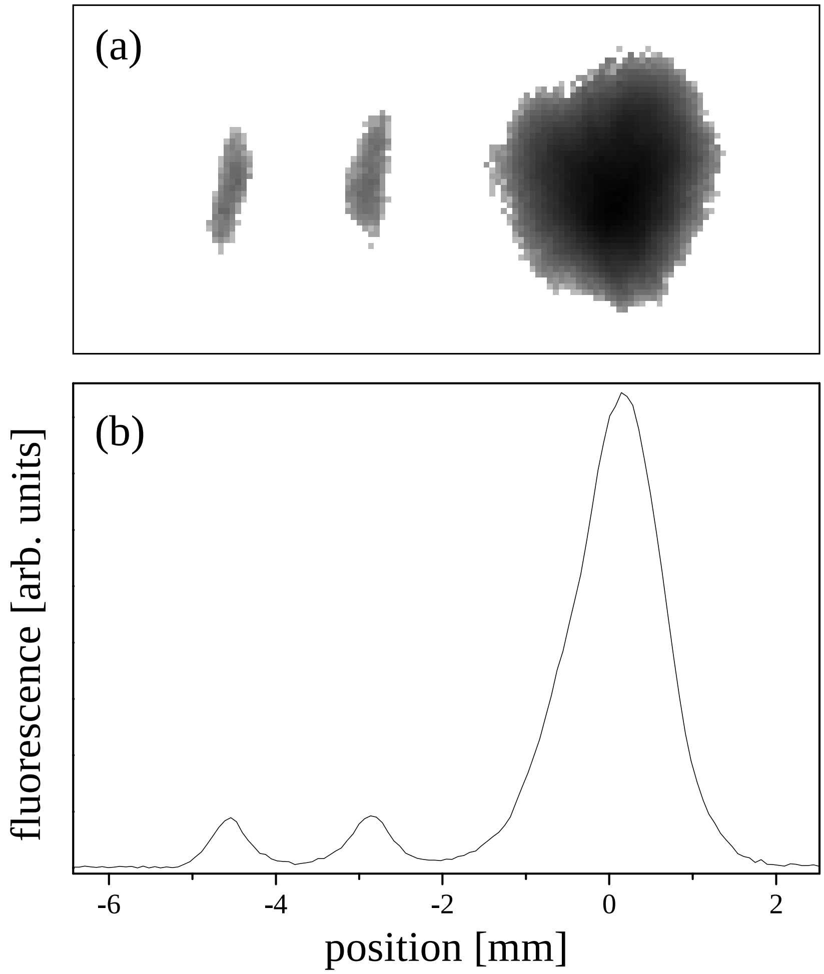

Figure 3.6: Part (a) shows an image of resonance fluorescence from an atomic distribution acquired by the CCD camera. This exposure is taken during the freezing molasses period following a time of ballistic expansion. Part (b) shows the same distribution integrated in the vertical direction. The large peak on the right is the part of the atomic cloud that was not trapped during the initial acceleration. The center peak indicates the atoms that were trapped in the first band at the beginning of the interaction but were driven out by the modulation. The leftmost peak corresponds to atoms that remained trapped during the entire sequence. The survival probability is the area under the left peak normalized by the sum of the areas under the left and center peak.

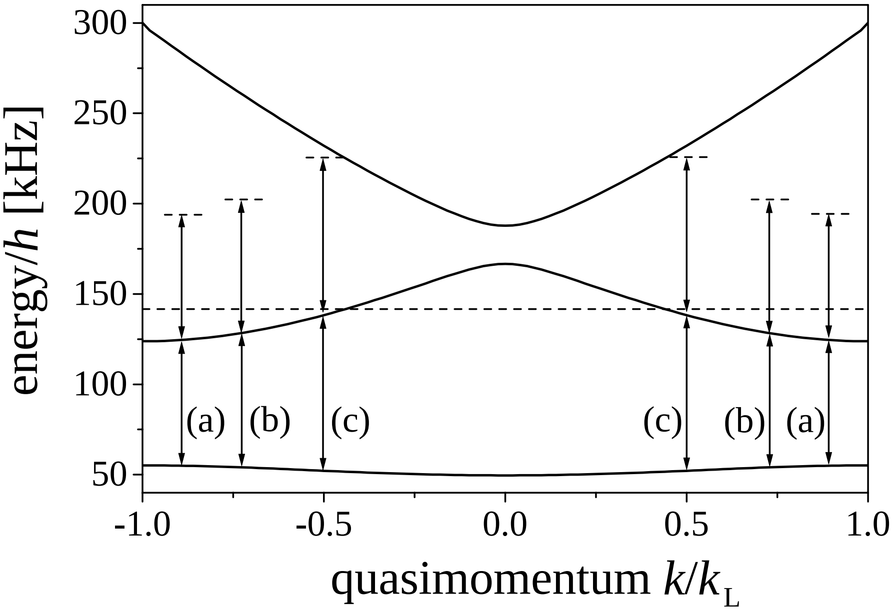

Figure 3.7: Band structure for an atom in a stationary lattice for a well depth of $V_0/h = 71$ kHz. In the reduced zone scheme the quasi-momentum k is limited to the first Brillouin zone $[-k_{\mathrm{L}}, +k_{\mathrm{L}}]$. The arrows correspond to a modulation frequency of (a) 70 kHz, (b) 75 kHz and (c) 85 kHz. The dashed line indicates the top edge of the potential ($2V_0$). The band gap for this value of V_0 is $E_{\mathrm{g}}/h = 69$ kHz.

to be considered. The analytic solutions for such a driven two-level system are well known and for the population evolution one expects to find Rabi oscillations between the bands. We assume that initially only the first band is populated. Then the initial population P_0 in the first band at a given value of k is $P_0 = 1$. The expectation value of the population P_1 in the second band at the same value of k evolves according to

$$P_1(t) = \frac{\Omega_{\mathrm{R}}^2}{\Omega_{\mathrm{eff}}^2} \sin^2(\frac{1}{2}\Omega_{\mathrm{eff}} t), \tag{3.41}$$

where Ω_{R} is the resonant Rabi frequency and Ω_{eff} is called the effective or off-resonant Rabi frequency. The resonant Rabi frequency is proportional to the matrix element of the driving term between the two coupled Bloch states,

$$\Omega_{\mathrm{R}} = \frac{1}{\hbar} \, \left| \langle \Psi_{0,k} \left| V_0 \, m \sin(2k_{\mathrm{L}}x) \right| \Psi_{1,k} \rangle \right| , \tag{3.42}$$

and the effective Rabi frequency is given by

$$\Omega_{\mathrm{eff}} = \sqrt{(\omega - \omega_0)^2 + \Omega_{\mathrm{R}}^2}, \tag{3.43}$$

where $\omega = 2\pi\nu_{\mathrm{p}}$ is the drive frequency and $\omega_0(k)$ is the transition frequency for a given value of k,

$$\hbar\omega_0(k) = E_1(k) - E_0(k). \tag{3.44}$$

Here, ω and ω_0 do not refer to the laser beam parameters as do the symbols introduced in Chapter 1.

If the drive frequency ν_{p} is close to resonance for both $1 \leftrightarrow 2$ and $2 \leftrightarrow 3$ [arrow (c) in Fig. 3.7], more than two levels participate in the interaction and more complicated dynamics are to be expected.

Figure 3.8 compares the evolution of the first band survival probability for increasing modulation amplitude. The data were recorded for $V_0/h = 71$ kHz and $\nu_{\mathrm{p}} = 70$ kHz, which corresponds to a drive resonant with states near

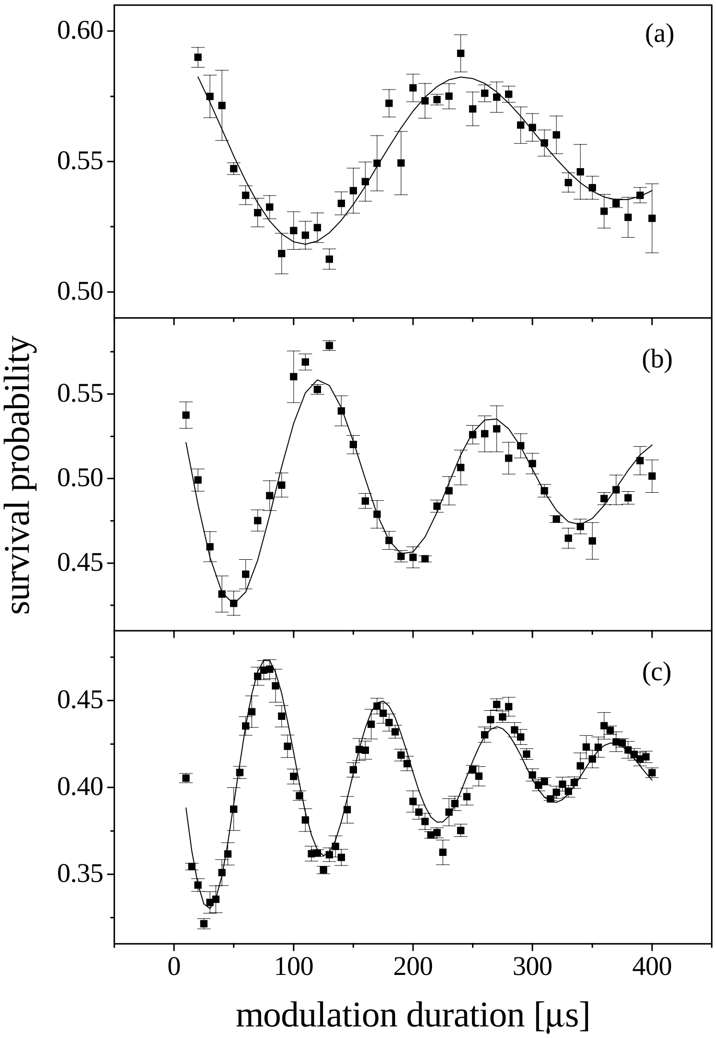

Figure 3.8: Measured survival probability in the lowest band as a function of modulation duration. The modulation amplitude was set to be (a) $m = 0.1$, (b) $m = 0.2$ and (c) $m = 0.3$. The data were taken at a well depth of $V_0/h = 71$ kHz and a modulation frequency of $\nu_\mathrm{p} = 70$ kHz corresponding to a drive near the band edge [as indicated in Fig. 3.7, arrow (a)]. Each run was repeated several times and the error bar denotes the one-sigma error of the mean. The solid line displays the fit of an exponentially damped cosine function to the data.

the band edge, as indicated by arrow (a) in Fig. 3.7. All graphs clearly show damped Rabi oscillations of the population in the first band. The damping can be explained by taking off-resonant transitions into account. Atoms with a quasi-momentum close to the value for which the resonance occurs can undergo Rabi oscillations with different frequencies and different amplitudes. Summing over the distribution of quasi-momenta leads to a dephasing of the oscillations and therefore to a decrease of the average oscillation. It is important to note that this damping effect is not caused by level decay, since the Bloch states involved are stable. The plots of the survival probability in the first band in Fig. 3.8 show an overall offset from unity at zero modulation duration. We attribute this to residual phase modulation of our standing wave caused by incomplete extinction of the modulation signal, which drives transitions to higher bands. This introduces a constant loss independent of the chosen modulation duration and does not affect the curve shape. Because the strength of the residual modulation depends on the set modulation amplitude m, the curve offset changes with increasing m.

As is evident from Fig. 3.8, the frequency of the Rabi oscillation increases with the modulation amplitude. By fitting an exponentially damped cosine function to the experimental data, the value for the oscillation frequency can be extracted.

The solid squares in Fig. 3.9 show the result of the least square fits. The error bars denote the uncertainty in the frequency fitting parameter. The plot shows a Rabi frequency that varies linearly with modulation amplitude m. As was discussed above, we can expect this linear relationship for a driven two-level system for the case of exact resonance. To compare to the experimental data, we calculated the Rabi oscillation frequency for a modulation driving transitions only at the band edge. Since the chosen value of $\nu_{\mathrm{p}} = 70$ kHz does not quite correspond to the band separation at the band edge ($E_{\mathrm{g}}/h = 69$ kHz),

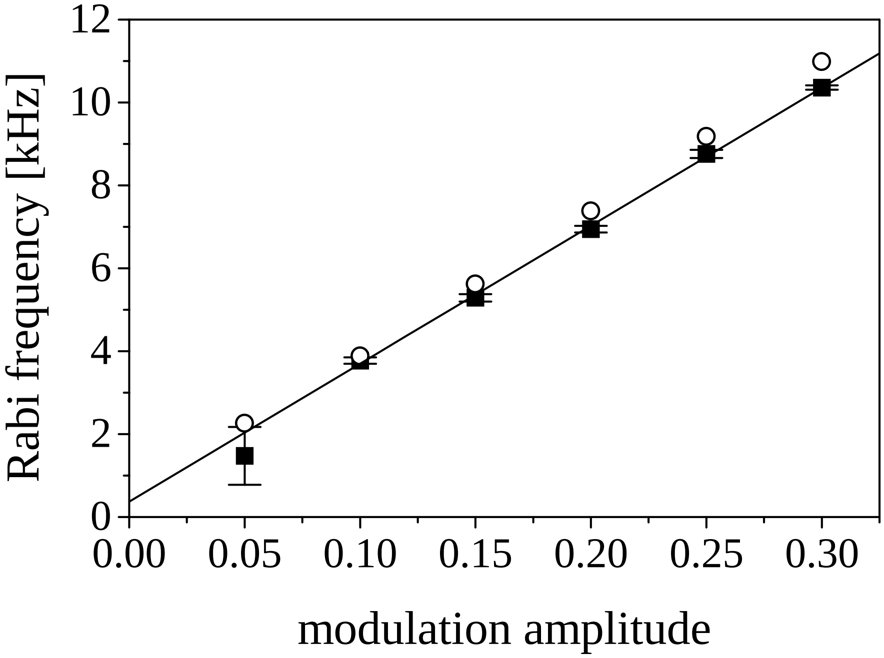

Figure 3.9: The solid squares show the measured Rabi frequency versus modulation amplitude for a well depth of $V_0/h = 71$ kHz and a drive frequency of $\nu_{\mathrm{p}} = 70$ kHz. Uncertainties in the least square fit of the frequency are indicated as error bars. The line depicts the result of a linear least square fit through the experimental data. The hollow dots are the calculated Rabi frequencies for a drive at the band edge ($\nu_{\mathrm{p}} = E_{\mathrm{g}}/h$), corresponding to the experimental parameters.

a slight detuning of the drive from the transition $1 \leftrightarrow 2$ has been taken into account. The resulting frequencies are displayed as hollow dots in Fig. 3.9. The calculation results are in good overall agreement with the experimental data. The slight deviation in frequency of the measured versus calculated data can be attributed to the experimental uncertainty in the determination of the well depth V_0. We could measure the intensity of the interaction beams to within $\pm 10\%$, which lead to the same relative error in the value for the well depth. To check the validity of restricting the range of quasi-momenta to the band edge, we performed a numerical integration of Schrödinger's equation including the full potential in Eq. (3.39), with an initial condition that was taken to be a uniform distribution of atoms in the first band. A more detailed description of the numerical procedure can be found in Appendix A. The frequencies of the resulting population oscillations are not plotted in Fig. 3.9 because, on the scale used, they are indistinguishable from the calculated values, shown by the hollow dots. The calculation and the numerical integrations were performed using experimental values for the well depth and drive frequency with no adjustable parameters.

Driving transitions at the band edge ($\nu_{\mathrm{p}} = E_{\mathrm{g}}/h$) has several advantages, one of which is the high density of states in that region. This results in a large number of atoms that can participate in the population transfer, therefore yielding a large detection signal. Another advantage is the slow damping rate of the Rabi oscillations. Since there is a large fraction of atoms contributing to the oscillation with the same frequency, the small number of off-resonantly driven atoms will not significantly decrease the amplitude of the averaged oscillation. Away from the band edge however, the relative weight of the resonant oscillation frequency becomes less dominant and the off-resonant drives lead to an increased damping rate. The evolution of the first band population for three different drive frequencies is depicted in Fig. 3.10. The data

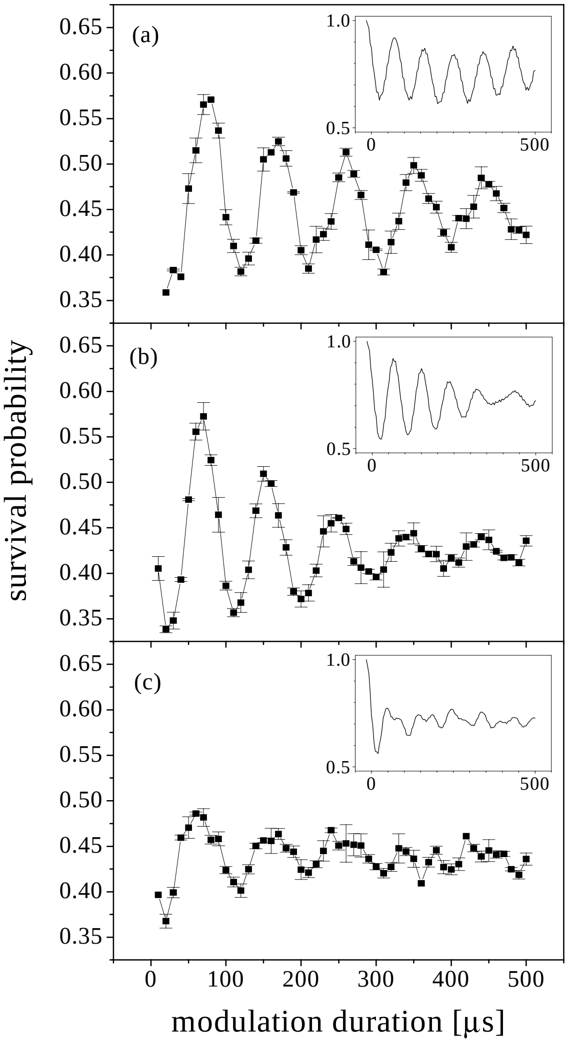

Figure 3.10: Measured survival probability in the lowest band as a function of modulation duration for three different frequencies. All data were recorded at a well depth of $V_0/h = 71$ kHz and a modulation amplitude of $m = 0.3$. The points are connected by solid lines for clarity. The insets show the result of numerical simulations at $V_0/h = 72$ kHz and $m = 0.3$. Note that the modulation duration does not include the 16 μs turn-on and turn-off time. The modulation frequency was set to be (a) $\nu_\text{p} = 70$ kHz, (b) $\nu_\text{p} = 75$ kHz, and (c) $\nu_\text{p} = 85$ kHz corresponding to drives indicated by the arrows in Fig. 3.7.

were recorded at a well depth of $V_0/h = 71$ kHz and a modulation amplitude of $m = 0.3$. The insets show the result of the numerical integrations, for which the well depth was adjusted to $V_0/h = 72$ kHz in order to produce matching damping rates. The modulation frequencies in Fig. 3.10(a) through (c) match the corresponding arrows in Fig. 3.7 [(a) 70 kHz, (b) 75 kHz and (c) 85 kHz]. Larger damping rates for increasing modulation frequencies are clearly visible. In addition, we observed a decrease in oscillation amplitudes due to a smaller density of states at the center of the band. At the opposite side of the energy band ($2\pi\nu_\mathrm{p} = \omega_0(k = 0)$) lower damping rates are recovered. Modulating the potential with frequencies beyond the band edges ($2\pi\nu_\mathrm{p} > \omega_0(k = 0)$) lead to Rabi oscillations with higher frequency and lower amplitude, as expected for off-resonantly driven systems (not shown).

3.4 Wannier-Stark ladder

In order to study the Wannier-Stark states experimentally, we used a similar spectroscopic technique as the one described above [31]. However, to create the Wannier-Stark states a constant acceleration of the optical potential was necessary. Therefore the frequency chirp was not stopped during the modulation time. The chirp rate, however, was adjusted to yield the desired value of the acceleration a. To spectroscopically investigate the states, we superimposed the phase modulation at frequency ν_p onto this frequency chirp. The time during which the atoms were exposed to the phase modulation (while undergoing an acceleration) was 500 μs. To obtain a spectrum of the Wannier-Stark states we repeated the experiment for various probe modulation frequencies, holding the modulation amplitude m and the duration fixed.

Figure 3.11 shows three measured spectra for the accelerations of 947 m/s^2, 1260 m/s^2, and 1680 m/s^2, which correspond to the Bloch frequencies $\omega_\mathrm{B}/2\pi$ = 16.0 kHz, 21.4 kHz, and 28.5 kHz respectively. The spectra were

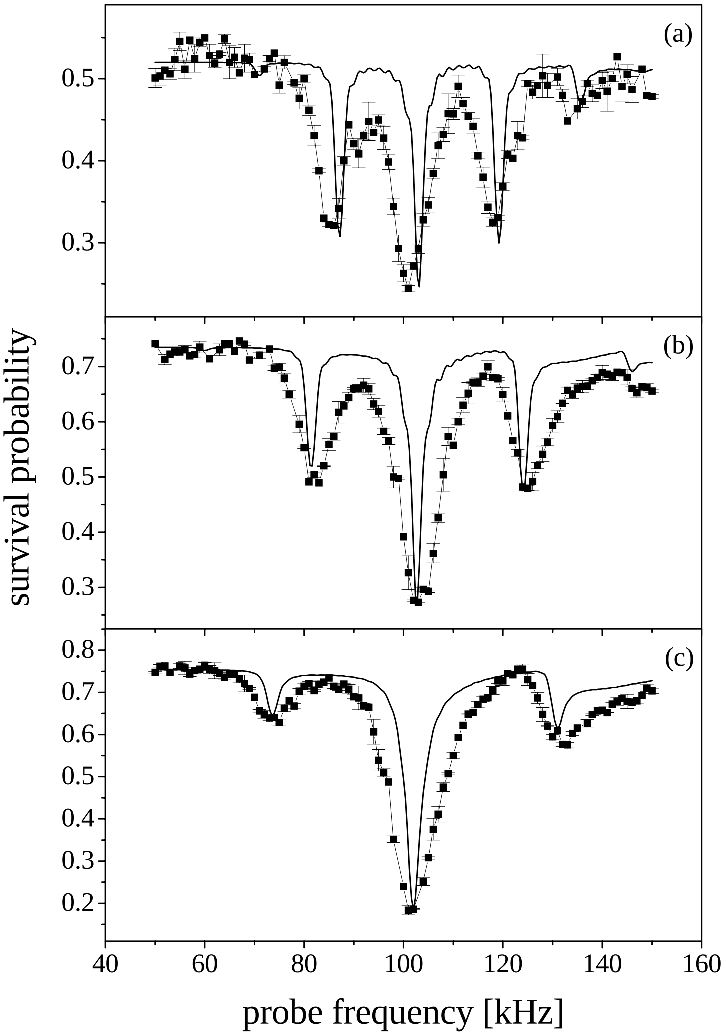

Figure 3.11: Wannier-Stark ladder resonances for a well depth of $V_0/h = 91.6$ kHz and accelerations of (a) 947 m/s^2, (b) 1260 m/s^2, and (c) 1680 m/s^2, which correspond to the Bloch frequencies $\omega_{\rm B}/2\pi = 16.0$ kHz, 21.4 kHz and 28.5 kHz respectively. For the chosen well depth, the average band spacing is $\bar{E}_{\rm g}/h = 104$ kHz which is in good agreement with the location of the central resonance. The points are connected by thin solid lines for clarity. The thick solid lines shows the results of numerical simulations using the experimental parameters.

obtained at a fixed well depth of $V_0/h = 91.6$ kHz and a fixed probe modulation amplitude of $m = 0.05$. For a well depth of $V_0/h = 91.6$ kHz, the average band spacing is $\bar{E}_{\mathrm{g}}/h = 104$ kHz, which is in good agreement with the location of the central resonance in the three spectra of Fig. 3.11. While Eq. (3.38) predicts the location of the spectral features, it is simply a statement of energy conservation and does not include the attenuation of the transition probability for states lying outside the allowed energy bands.

Also shown in Fig. 3.11 is the result of a numerical integration of the time-dependent Schrödinger equation using the experimental parameters. We believe that phase noise in the interaction beams prevented the survival probability from reaching unity, when the probe was far from resonance, and reduced the depth of the spectral features by a constant factor. For this reason, the y-values of the theory curves were shifted and scaled to match the baseline and amplitude of the central resonance. In addition, the value for the probe modulation amplitude m was adjusted in the numerical simulations from 0.05 to 0.035 to reproduce the relative peak heights.

The spectral width of the resonances is fundamentally determined by the finite lifetime of the Wannier-Stark states due to tunneling. For the case of $a = 1680$ m/s^2, where the tunneling rate is the highest, the Landau-Zener lifetime of the states in the second band exceeds 125 μs, leading to a broadening of less than 1.3 kHz. Due to the finite probe interaction time of 500 μs, one would expect the resonances to be further broadened by 2 kHz; however, there were a number of experimental mechanisms which contributed to the measured width being substantially broader than that predicted by the simulations. The first source of line broadening was due to phase noise in the standing wave beams with a 5 kHz bandwidth resulting from mirror vibrations and electronic noise in the acousto-optic modulator drivers. The second source of broadening came from variations in the well depth which, for the range considered, is approximately proportional to the average band spacing and therefore the absolute position of the resonances. Although the transverse Gaussian width of the standing wave beams was large compared to the initial size of the atomic distribution, fast atoms could move radially out of the center and across the profile producing a time-dependent variation in their effective well depth. By limiting the binning window of the 2D images in order to restrict our measurement to a colder subset of atoms in one of the transverse directions, we were able to reduce but not totally eliminate this effect.

A series of Wannier-Stark spectra were taken at different accelerations while keeping the well depth constant. The peak locations were determined in each case and are plotted versus the acceleration in Fig. 3.12, generating the Wannier-Stark fan. The solid lines are the resonance locations as predicted by Eq. (3.38). In accordance with theory there is one resonance ($m = 0$) at a frequency corresponding to the average band spacing. The location of this resonance does not change as the acceleration is varied, while the other peaks spread out with a slope proportional to m.

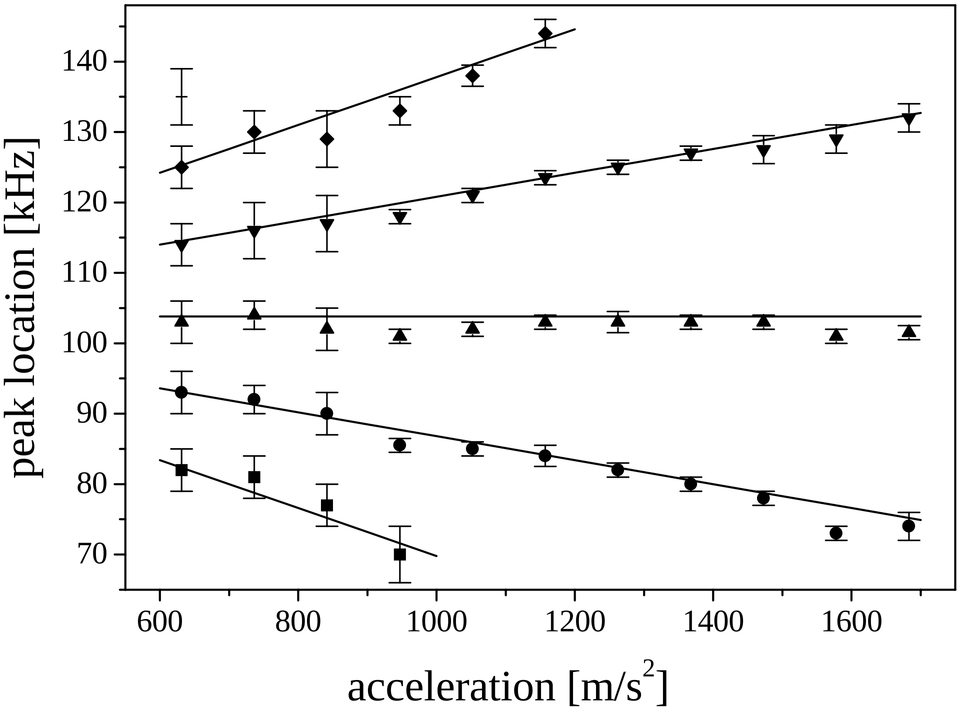

Figure 3.12: A fan plot of the Wannier-Stark resonances for a well depth of $V_0/h = 91.6$ kHz. The position of the center resonance is independent of acceleration and corresponds to the average band spacing. The solid lines represent the resonance locations as predicted by Eq. (3.38).

Chapter 4

Quantum Tunneling

In the previous chapter we studied the spectral features of Bloch states and Wannier-Stark states by driving transitions between those states. These inter-band transitions, which provided the basis for the experimental study, were imposed externally by a modulation of the potential. Without modulation the band index was conserved. The accelerations that transported the atoms through reciprocal space were small enough to preserve the validity of the semiclassical equations of motion in Section 3.2.1.

In this chapter we investigate the effect of a large acceleration of the optical potential. In this case the semiclassical equations no longer hold and inter-band tunneling can occur. The atoms can leave the trapping potential via tunneling into the continuum of free states. The system is therefore unstable and the number of trapped atoms decays with time. By adjusting the acceleration the stability of the system can be altered dynamically and the decay rates vary over a wide range. In this system, short-time deviations from the universal exponential decay law are observed [32]. In addition, we study the fundamental effects of measurements on the decay rate and report on the first observation of the Quantum Zeno and Anti-Zeno effects in an unstable system.

4.1 Classical limits

As derived in Chapter 3, atoms in an accelerated standing wave are subject to a potential

$$V(x) = V_0 \cos(2k_\mathrm{L} x) + Max. \tag{4.1}$$

This potential is stated in the reference frame accelerated with the potential as given in Eq. (3.26). For a small enough acceleration a particle can be classically trapped within the wells of this 'washboard' potential as indicated in Fig. 4.1(a). In this case the particle will accelerate along with the potential. For a larger acceleration the potential wells become increasingly asymmetric up to a point where the particle is no longer confined by the potential. A sketch of this situation is given in Fig. 4.1(b). The critical acceleration $a_\mathrm{c,class}$, for which the potential looses its ability to confine the particle can be found by solving for the extrema of the potential in Eq. (4.1)

$$\frac{dV}{dx} = -2k_\mathrm{L} V_0 \sin(2k_\mathrm{L} x) - Ma = 0. \tag{4.2}$$

This equation only has solutions for

$$|a| < a_\mathrm{c,class} = \frac{2k_\mathrm{L} V_0}{M}. \tag{4.3}$$

For accelerations smaller than $a_\mathrm{c,class}$ the particle gets accelerated along with the potential whereas for larger accelerations there are no local potential minima.

4.2 Landau-Zener tunneling

4.2.1 Tunneling rates

In this section we provide a short description of the Landau-Zener tunneling process based on diabatic transitions in momentum space [29, 33]. An alternative description can be derived in the position representation [7, 34].

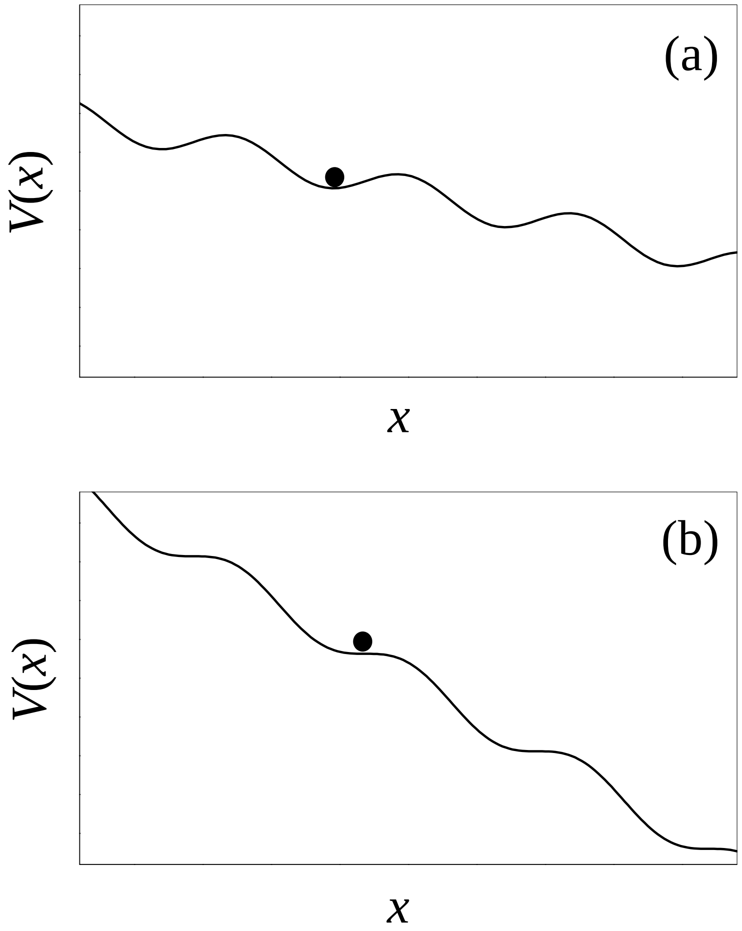

Figure 4.1: Sketch of the classical confinement of a particle in the tilted washboard potential of an accelerated lattice. Part (a) shows the case for small acceleration where the particle is confined within the potential wells. In part (b) the acceleration has been increased to a point where the wells no longer provide confinement.

As a starting point for the derivation of the tunneling rates we consider the semiclassical equations of motion as derived in Section 3.2.1. These equations describe the time evolution of the quasi-momentum in reciprocal space. In order to allow for inter-band transitions we now must abandon the condition that the band index be a constant of motion. The shape of the Bloch bands and the time evolution equation for the quasi-momentum are still assumed to be valid. As we pointed out in Section 3.2.2, the stationary periodic potential causes the free particle energy levels to undergo a level repulsion. This shift is most pronounced at the edges of the Brillouin zone. A particle approaching the avoided level crossing might not be able to follow the dispersion curve adiabatically, in which case it continues its motion and diabatically changes levels across the energy gap. In 1932 Zener derived an expression for the probability P of diabatic transfer between two repelled levels [33]

$$P = \exp\left(-\frac{\pi}{2\hbar}\,\frac{E_{\mathrm{g}}^2}{\frac{d}{dt}(\epsilon_1-\epsilon_2)}\right), \tag{4.4}$$

where E_{g} is the minimum energy separation of the perturbed levels and $\epsilon_{1,2}$ are the unperturbed energy eigenvalues of level 1 and 2, respectively. In our case the unperturbed energy curve is simply the free particle kinetic energy dispersion $E_p = p^2/2M$. Since at the edges of the Brillouin zone the levels are symmetric with respect to reflection at the zone boundary we can evaluate

$$\begin{aligned} \frac{d}{dt}(\epsilon_1-\epsilon_2) &= 2\,\frac{dE_p}{dt}\bigg|_{p=n\,\hbar k_{\mathrm{L}}} = 2Ma\,\frac{dE_p}{dp}\bigg|_{p=n\,\hbar k_{\mathrm{L}}} \\ &= 2n\,a\,\hbar k_{\mathrm{L}}, \end{aligned} \tag{4.5}$$

where we used $p = p_0 + Mat$ to describe the evolution of the momentum, and n is the band index. In using this relation we have implicitly made use of the semiclassical equation of motion for the quasi-momentum. Inserting Eq. (4.5) into Eq. (4.4) we obtain for the probability of transfer

$$P = e^{-a_{\mathrm{c}}/a}, \tag{4.6}$$

where the critical acceleration a_c is given by

$$a_\mathrm{c} = \frac{\pi}{4}\,\frac{E_\mathrm{g}^2}{n\,\hbar^2 k_\mathrm{L}}. \tag{4.7}$$

Let N denote the number of particles populating the lowest band within the first Brillouin zone. Then the rate r of atoms crossing the band gap is equal the rate of atoms approaching the transition region times the probability of tunneling

$$r = -\frac{dN}{dt} = \frac{N}{2k_\mathrm{L}}\frac{dk}{dt}\,P = N\,\frac{Ma}{2\hbar k_\mathrm{L}}\,P, \tag{4.8}$$

where we have assume the band to be uniformly populated. Solving the above equation for N yields an exponential decay of the population in the band under consideration as

$$N = N_0\,e^{-\Gamma_\mathrm{LZ}\,t} \tag{4.9}$$

with the Landau-Zener (LZ) decay rate Γ_LZ given by

$$\Gamma_\mathrm{LZ} = \frac{a}{2v_\mathrm{r}}\,e^{-a_\mathrm{c}/a}. \tag{4.10}$$

Experimental studies of the tunneling rates out of the lowest band were performed in our group and the decay rates were compared to the Landau-Zener prediction [35, 36].

4.2.2 Deviations from Landau-Zener tunneling

The expression for the LZ tunneling rate derived above is based on a single transit of the atom through the region of an avoided crossing. However, for small tunneling probability the atom can undergo Bloch oscillations within a given band, leading to multiple passes through the Brillouin zone. As described in Section 3.2.2, the tunneling amplitudes can interfere constructively or destructively depending on the rate at which the atom traverses the Brillouin zone. This mechanism is responsible for the formation of the tunneling resonances in Eq. (3.37). For small accelerations the tunneling rate is small and the atoms can perform many Bloch oscillations before leaving the band. Therefore large deviations from the Landau-Zener prediction for the tunneling rate are to be expected. For a larger acceleration the atom leaves the band quickly and the interference effects are less pronounced. For those cases the LZ prediction is a good approximation for the actual tunneling rate. These statements are in agreement with the observed tunneling rates [35, 36].

4.3 Non-exponential decay

4.3.1 Theoretical description

An exponential decay law is the universal hallmark of unstable systems and is observed in all fields of science. This law is not, however, fully consistent with quantum mechanics and deviations from exponential decay have been predicted for short as well as long times [37, 38, 39]. In 1957 Khalfin showed that if H has a spectrum bounded from below, the survival probability is not a pure exponential but rather of the form

$$\lim_{t\to\infty} P(t) \approx \exp(-ct^q) \qquad q < 1, c > 0. \tag{4.11}$$

Later Winter examined the time evolution in a simple barrier-penetration problem [38]. He showed that the survival probability begins with a non-exponential, oscillatory behavior. Only after this initial time does the system start to evolve according to the usual exponential decay of an unstable system. Finally, at very long times, it decays like an inverse power of the time. The initial non-exponential decay behavior is related to the fact that the coupling between the decaying system and the reservoir is reversible for short enough times. Moreover, for these short times, the decayed and undecayed states are not yet resolvable, even in principle.

A simple argument will illustrate this point. We assume that the system is initially in the undecayed state $|\Psi_0\rangle$ at $t = 0$, and that the state evolves under the action of the Hamiltonian H,

$$|\Psi(t)\rangle = e^{-iHt/\hbar}|\Psi_0\rangle = A(t)|\Psi_0\rangle + |\Phi(t)\rangle, \tag{4.12}$$

where $A(t)$ is the probability amplitude for remaining in the undecayed state

$$A(t) = \langle\Psi_0|e^{-iHt/\hbar}|\Psi_0\rangle, \tag{4.13}$$

and the state $|\Phi(t)\rangle$ denotes the decayed state with $\langle\Psi_0|\Phi(t)\rangle = 0$. The probability of survival P in the undecayed state is therefore

$$P(t) = |A(t)|^2. \tag{4.14}$$

Acting with the time evolution operator $e^{-iH(t+t')/\hbar}$ on the state $|\Psi_0\rangle$ and projecting onto the initial state yields

$$A(t+t') = A(t)A(t') + \langle\Psi_0|e^{-iHt'/\hbar}|\Phi(t)\rangle, \tag{4.15}$$

where we have made use of Eq. (4.12) and the orthonormality relation. If it were not for the last term, the equation above would generate the characteristic exponential decay law of an unstable system. However, the term under consideration describes the possibility for the decayed state $|\Phi(t)\rangle$ to re-form the initial state $|\Psi_0\rangle$ under the time evolution operator for time t'.

For very short times we can determine the time evolution of the survival probability P explicitly. Given that the mean energy of the decaying state is finite, one can show following the arguments of Fonda et al. [39], that

$$\left.\frac{dP(t)}{dt}\right|_{t\to 0} = 0. \tag{4.16}$$

To derive this property, we consider a complete set of commuting observables H and α and their common eigenstates $|\phi_{E,a}\rangle$ with discrete and/or continuous spectra. The completeness relation is

$$\int dE\,da\,|\phi_{E,a}\rangle\langle\phi_{E,a}| = \mathbf{1}, \tag{4.17}$$

and we can expand our state in terms of this basis set. Doing so, we have

$$A(t) = \int_{-\infty}^{\infty} dE\,\omega(E)e^{-iEt/\hbar}, \tag{4.18}$$

where

$$\omega(E) = \int da\,|\langle\phi_{E,a}|\Psi_0\rangle|^2 . \tag{4.19}$$

Now, we make the assumption that H has a spectrum that is bounded from below. This assumption is reasonable and necessary for a physical system. This allows us to restrict the range of integration in Eq. (4.18) to

$$A(t) = \int_{E_{\min}}^{\infty} dE\,\omega(E)e^{-iEt/\hbar}, \tag{4.20}$$

Utilizing the normalization condition for Ψ we get

$$\begin{aligned}\int_{E_{\min}}^{\infty} dE\,\omega(E) &= \int_{E_{\min}}^{\infty} dE \int da\,|\langle\Psi|\phi_{E,a}\rangle\langle\phi_{E,a}|\Psi\rangle| \\ &= \langle\Psi|\Psi\rangle = 1.\end{aligned} \tag{4.21}$$

Since we have from Eq. (4.21) that

$$\int_{E_{\min}}^{\infty} dE\,|\omega(E)| < \infty, \tag{4.22}$$

it can be shown that it is possible to extend the definition of $A(t)$ to negative times. This condition also ensures that the integral defining $A(t)$ is uniformly convergent and that $A(t)$ is continuous for all times. Since $\omega(E)$ is real, one can see that

$$A^*(t) = A(-t). \tag{4.23}$$

Now, we make the second assumption that the mean energy in the state $|\Psi\rangle$ is finite:

$$\langle E\rangle = \langle\Psi|H|\Psi\rangle = \int dE\,\omega(E)\,E < \infty. \tag{4.24}$$

This assumption implies that the derivative of A is well defined and is continuous everywhere, since

$$\frac{dA(t)}{dt} = -\frac{i}{\hbar}\int dE\,\omega(E)Ee^{-iEt/\hbar}. \tag{4.25}$$

Using Eq. (4.23), the survival probability can be rewritten as

$$P(t) = A^*(t)A(t) = A(-t)A(t). \tag{4.26}$$

Taking the derivative, we have, using the chain rule,

$$\frac{dP(t)}{dt} = \frac{dA(-t)}{dt}A(t) + A(-t)\frac{dA(t)}{dt}, \tag{4.27}$$

and since both A and its derivative are continuous and $A \rightarrow 1$ as $t \rightarrow 0$ we have immediately that

$$\left.\frac{dP(t)}{dt}\right|_{t=0} = 0. \tag{4.28}$$

The form of the expression for the survival probability P in Eq. (4.14) implies the shape of the initial time dependence. As outlined by Grotz and Klapdor [40] we can expand $A(t)$ in a power series

$$\begin{aligned} A(t) &= \langle\Psi_0|e^{-iHt/\hbar}|\Psi_0\rangle & (4.29)\\ &= 1 - i\frac{t}{\hbar}\langle\Psi_0|H|\Psi_0\rangle - \frac{t^2}{2\hbar^2}\langle\Psi_0|H^2|\Psi_0\rangle + O(t^3). & (4.30)\end{aligned}$$

Using this expansion results in an expression for the survival probability

$$P(t) = |A(t)|^2 = 1 - \frac{t^2}{\hbar^2}\langle\Psi_0|(H-\bar{E})^2|\Psi_0\rangle + O(t^4), \tag{4.31}$$

where $\bar{E} = \langle\Psi_0|H|\Psi_0\rangle$. This form also indicates a population transfer beginning with a flat slope in accordance with Eq. (4.28) and suggests an initial quadratic time dependence. However, this simple argument neglects the convergence properties of the series and can not be considered as rigorous as the arguments leading to the derivation of Eq. (4.28).

The results stated here are general properties independent of the details of the interaction. However, the time scale over which the deviation from exponential behavior is apparent depends on the particular time scales of the decaying system. Greenland and Lane point out a number of time scales which are relevant [41]. The first time scale τ_e is given by the time that it takes the decay products to leave the bound state region. This time can be estimated as

$$\tau_\mathrm{e} = \frac{\hbar}{E_0}, \tag{4.32}$$

where E_0 is the energy released during the decay. It determines the amount of time required to pass before the decayed and undecayed states can be resolved. The second time scale τ_w is related to the bandwidth ΔE of the continuum to which the state is coupled

$$\tau_\mathrm{w} = \frac{\hbar}{\Delta E}. \tag{4.33}$$

The phases of all states in the continuum evolve at a rate corresponding to their energy. Thus after the time τ_w the phases of these states have spread over such a wide range as to prevent the reformation of the initial undecayed state. After this dephasing time, the coupling is essentially irreversible.

Although these predictions are of general nature and applicable in every unstable system, deviations from exponential decay have not been observed experimentally in any other system than the one described here [32]. The primary reason is that these characteristic time scales in most naturally occurring systems are extremely short. For the decay of a spontaneous photon, the time τ_e it takes a photon to traverse the bound state size is approximately an optical period, 10^{-15} s. For a nuclear decay this time scale is orders of magnitude shorter, about 10^{-21} s. By contrast, the dynamical time scale for an atom bound in an optical lattice is just the inverse band gap energy, which in our experiments is on the order of several microseconds.

Niu and Raizen [42] performed a more detailed investigation of a two-band model of our system. They find an initial non-exponential regime that starts with a quadratic time dependence, then becomes a damped oscillation, and finally settles into an exponential decay. The time scale for which the coherent oscillations damp out and the exponential decay behavior sets in is identified as the crossover time t_{c} equal to

$$t_{\mathrm{c}} = \frac{E_{\mathrm{g}}}{a} \frac{1}{2\hbar k_{\mathrm{L}}}. \tag{4.34}$$

For a typical value for the acceleration of $a = 10,000\,\mathrm{m/s}^2$ and a band gap of $E_{\mathrm{g}}/h = 80$ kHz the crossover time calculates to $t_{\mathrm{c}} = 2\,\mu$s.

4.3.2 Experimental realization

To observe tunneling out of the lowest band of an optical potential some changes had to be made to the setup used in the quantum transport experiments described in Chapter 3. The procedure for cooling and trapping a sample of atoms is outlined in in Section 2.2. For the experiments described in this chapter the final atomic distribution had a width of $\sigma_x = 0.3$ mm in position and $\sigma_p = 6\,\hbar k_{\mathrm{L}}$ in momentum.

The preparation of the initial state was done in a similar fashion as described earlier. After turning on the interaction beams, a small acceleration of $a_{\mathrm{trans}} = 2,000\,\mathrm{m/s}^2$ was imposed to separate those atoms projected into the lowest band from the rest of the distribution. After reaching the velocity $v_0 = 35\,v_{\mathrm{r}}$ the acceleration was suddenly increased to a value a_{tunnel} where appreciable tunneling out of the first band occurred. Unlike in the quantum transport experiments no phase modulation was added to induce transitions between the bands. The large acceleration a_{tunnel} was maintained for a period of time t_{tunnel}, after which time the frequency chirping continued again at the decreased rate corresponding to a_{trans}. This separated in momentum space the atoms that were still trapped in the lowest band from those in higher bands. After reaching a final velocity of $v_{\text{final}} = 80\, v_{\text{r}}$ the interaction beams were switched off suddenly. A diagram of the velocity profile versus time is shown in Fig. 4.2(a).

In the detection phase we determined the number of atoms that were initially trapped and what fraction remained in the first band after the tunneling sequence. After an atom tunneled out of the potential during the sequence, it would maintain the velocity that it had at the moment of tunneling. Turning off the light beams allowed the atoms to expand freely. During this period of ballistic expansion each atom moved a distance proportional to its velocity. Due to the difference in final velocity, trapped and tunneled atoms separated and could be spatially resolved. After the expansion the position distribution of the atoms was determined by imaging their fluorescence in a 'freezing molasses' as described in Section 2.4. Regions of the two-dimensional image were then integrated to obtain the desired fraction of remaining atoms over the number of initially trapped atoms. A typical integrated distribution is shown in Fig. 4.2(b). For this trace, about one third of the initially trapped atoms have tunneled out of the optical potential during the fast acceleration duration. To observe the temporal evolution of the fundamental band population we repeated the experiment for various tunneling durations t_{tunnel}, holding the other parameters of the sequence fixed.

Since we were mainly interested in the decay behavior of the system for very short times, a careful timing calibration was necessary. The time scale for deviations from the exponential decay law was estimated in the previous section to be on the order of $2\,\mu$s. The timing resolution of the tunneling duration needed to be much more precise than this time scale. The time of tunneling was given by the duration of the large tunneling acceleration a_{tunnel}. The scan rate of the frequency difference between the two beams therefore had

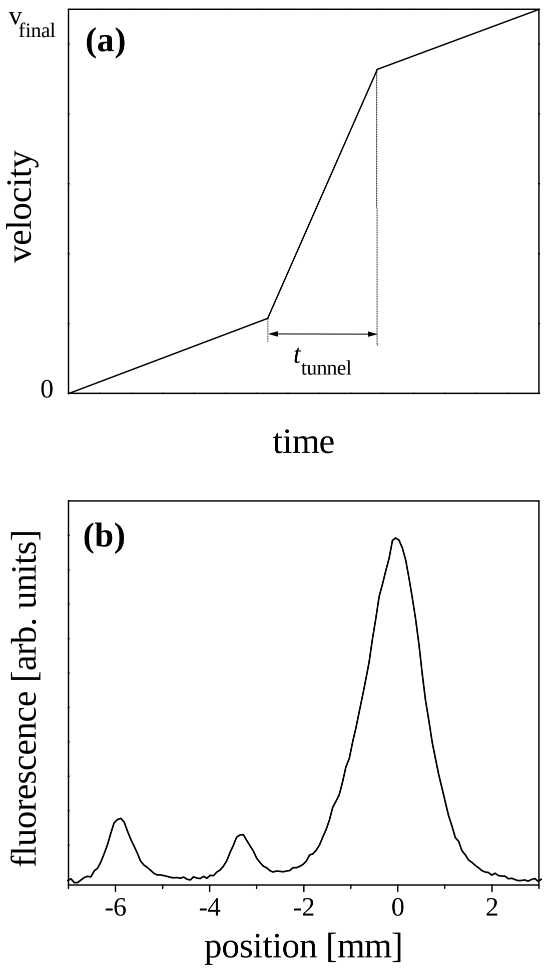

Figure 4.2: Part (a) shows a diagram of the acceleration sequence to study tunneling out of the lowest band. Part (b) shows a typical integrated spatial distribution of atoms after the time of ballistic expansion. The large peak on the right is the part of the atomic cloud that was not trapped during the initial acceleration. The center peak indicates the atoms that tunneled out of the optical potential during the fast acceleration period. The leftmost peak corresponds to atoms that remained trapped during the entire sequence.

to be switched from a rate corresponding to a_{trans} to a_{tunnel} and back within less than one microsecond.

In order to determine the time response of the system to a change of acceleration, a Fourier analysis method was utilized. The starting point for the analysis was the desired velocity profile that was programmed to control the frequency difference between the counter-propagating interaction beams. A repeated sequence of this velocity profile was expanded in a Fourier series. In order to simplify the analysis and to treat the most demanding case encountered, $a_{\text{trans}} = 0$ was chosen. An example of the profile to be analyzed is shown in Fig. 4.3(a). In this example the desired time of large acceleration is $1\,\mu$s. Due to the simplicity of the function, an analytic solution for the Fourier coefficients could be obtained. As indicated in Fig. 2.5, the signal of the velocity ramp passes through various electronic devices on its way to a voltage-controlled oscillator, where it determines the frequency of the AOM RF drive. In the AOM it finally determines the frequency of the acoustic wave and therefore the frequency shift of the light beam passing through it. Due to frequency dependent losses in the electronic setup and the finite propagation speed of the sound wave within the AOM crystal, the shape of the signal profile will undergo changes. In order to determine the response of the system to the desired velocity profile, the frequency dependent transfer function was experimentally determined. For this purpose a sinusoidal control signal was applied to the control input and the size of the modulation in the light was determined by acquiring a heterodyne spectrum [7]. The resulting transfer function of the complete control system (electronics and AOM) is shown in Fig. 4.4. The amplitude response is consistent with the amplitude transfer function of a double-pole Butterworth low-pass filter [43]

$$\frac{A_{\text{out}}}{A_{\text{in}}} = \frac{1}{\sqrt{1 + (f/f_{\text{c}})^4}}. \tag{4.35}$$

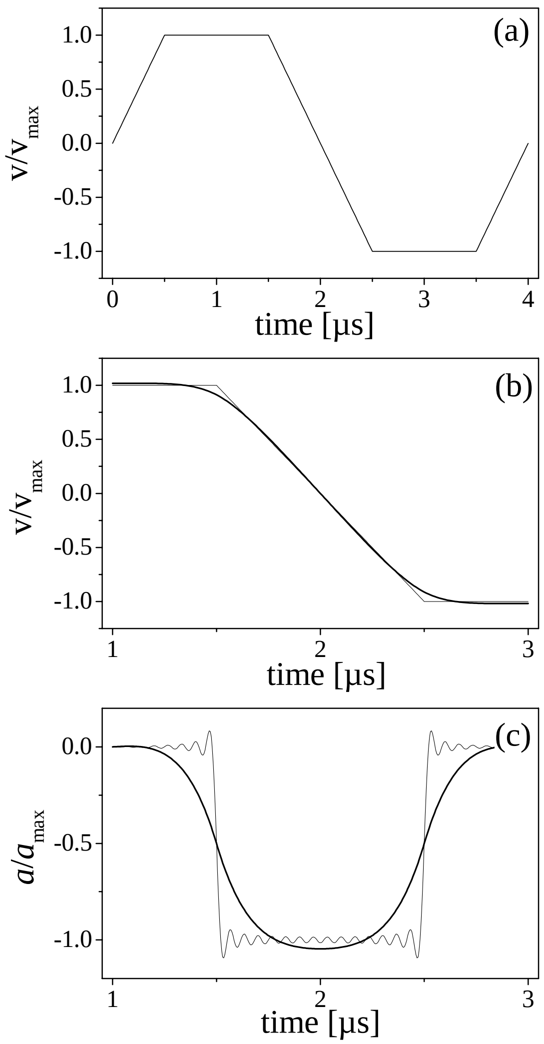

Figure 4.3: Fourier analysis of the velocity profile. Part (a) shows an example profile to be analyzed. In this case the desired tunneling duration is 1 μs. Part (b) shows the central region of the transmitted profile after re-summation of the first 30 Fourier components. For the thick line the transfer function has been taken into account, whereas the thin line shows the sum for an ideal transfer. Part (c) shows the derivative of the Fourier sums in (b). The time to switch between the two accelerations is estimated as 220 ns.

The cut-off frequency f_c was determined with a least square fit to be $f_\mathrm{c} = 0.98$ MHz. With the knowledge of the transfer function we were able to calculate the system response to an arbitrary velocity profile. For the example in Fig. 4.3 we re-summed the Fourier series after multiplying each term with the frequency dependent attenuation factor in Eq. (4.35). The resulting profile is shown in Fig. 4.3(b), where the re-summation with no attenuation is included for comparison. The acceleration of the potential was determined by taking the derivative of the velocity curve, as shown in part (c) of the same figure. From this graph we can estimate the time it takes to switch between a_trans and a_tunnel as the time during which the acceleration is outside the windows of 20% around the two values. For the worst-case example of Fig. 4.3 this time was 220 ns. Subtracting this switching time from all the tunneling durations in the analysis of the data ensured that only sections were included for which tunneling was substantial. Since the values for a_trans and a_tunnel were chosen to correspond to the most stringent case, using this overestimated value for the switching time of 220 ns established a lower bound for the actual tunneling duration.

Figure 4.5 shows the probability of survival in the accelerated potential as a function of the duration of tunneling for various values of the tunneling acceleration a_tunnel between 6,000 m/s^2 and 20,000 m/s^2. The value for the well depth for all curves was $V_0/h = 92$ kHz. Each point represents the average of 5 experimental runs, and the error bar denotes the error of the mean. Initially, the survival probability shows a flat region, owing to the reversibility of the decay process for short times. At intermediate times the decay shows a damped oscillation, that for long times evolves into the characteristic exponential decay law. By this time the coupling is essentially irreversible and reformation of the undecayed state is prohibited. As a comparison we also show the results of quantum mechanical simulations of the entire experimental sequence as solid

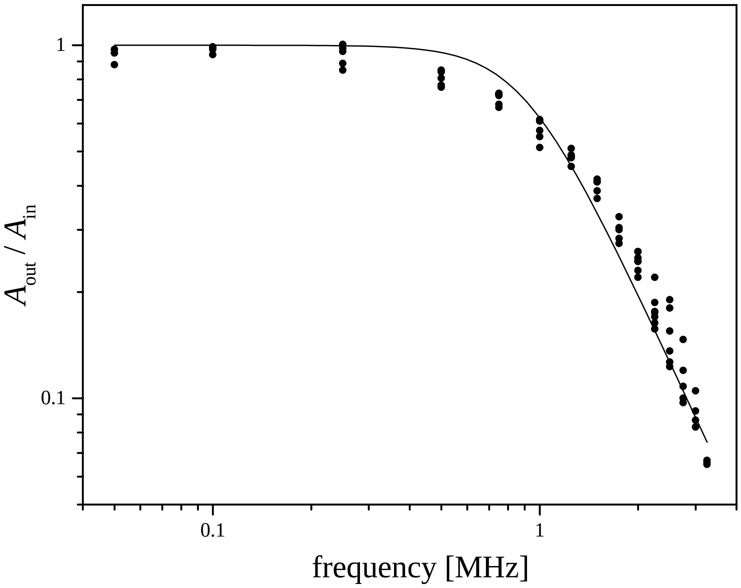

Figure 4.4: Measured amplitude transfer function of the combined system of electronics and optics controlling the velocity profile of the standing wave. The data points show the attenuation values as determined by analyzing a heterodyne spectrum versus the frequency of the calibration signal. The solid line shows a fit to a double-pole Butterworth low-pass filter response.

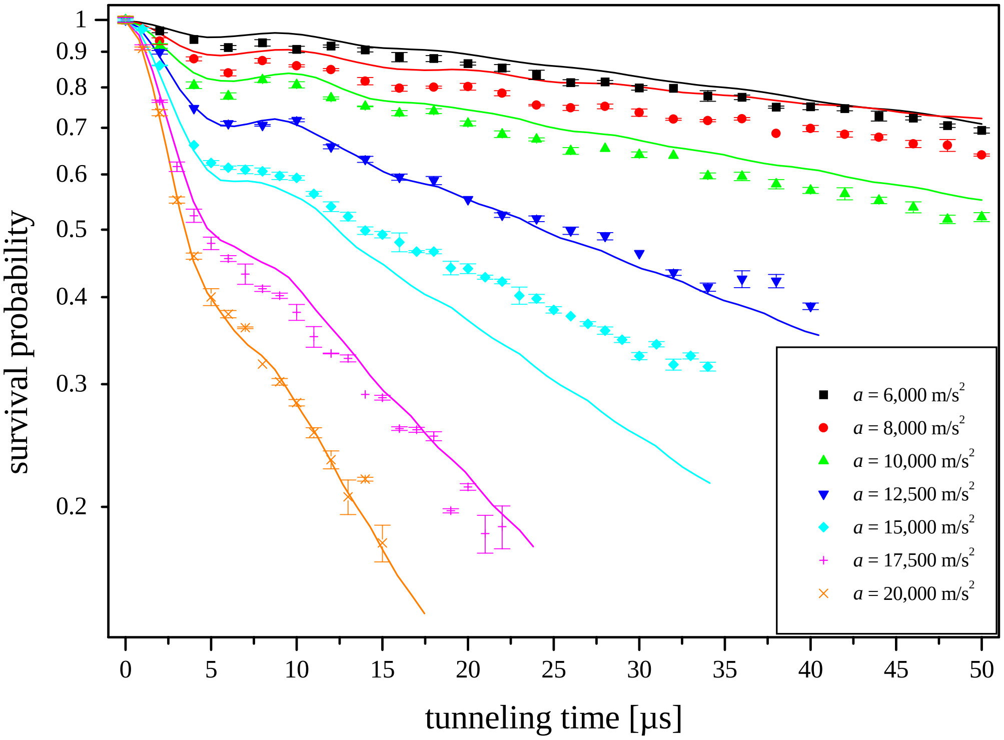

Figure 4.5: Probability of survival in the accelerated potential as a function of duration of the tunneling acceleration. Data points for different values of the large acceleration a_{tunnel} are shown. The error bars denote the error of the mean. These data were recorded for a well depth of $V_0/h = 92$ kHz. The data have been normalized to unity at $t_{\mathrm{tunnel}} = 0$ in order to compare to the simulations. The solid lines are quantum mechanical simulations of the experimental sequence with no adjustable parameters.

lines in the same graph. The tunneling rates depend strongly on the well depth of the potential. Considering the uncertainty of 10% in the calibration of the power in the interaction beams, the simulations match the observed data quite well.

4.4 Quantum Zeno and Anti-Zeno effects

The universal phenomenon of non-exponential decay of unstable systems led Misra and Sudarshan in 1977 to the prediction that frequent measurements during this non-exponential period could inhibit decay entirely [44, 45, 46]. They named this effect the *Quantum Zeno effect* after the Greek philosopher, famed for his paradoxes and puzzles. In his most famous paradox, Zeno considers an arrow flying through the air. The time of flight can be subdivided into infinitesimally small intervals during which the arrow moves only by infinitesimal amounts. Assuming the summation of infinitesimal terms amounts to nothing led Zeno to believe that motion is impossible and is merely an illusion. The version put forth by Misra and Sudarshan is the quantum mechanical version of the paradox.

To illustrate their main point we consider the time evolution of a system in the non-exponential regime, where the probability of remaining in the undecayed state is given by Eq. (4.31)

$$P(t) = 1 - \frac{t^2}{\hbar^2} \langle H^2 \rangle. \tag{4.36}$$

We now subdivide the time t into n time intervals of length τ and perform a measurement of the system after each interval. Each measurement redefines a new initial condition and effectively resets the time evolution. The system must therefore start the evolution again with the same non-exponential decay features. The probability of remaining in the undecayed state at time t (after

n measurements at intervals τ) is therefore

$$P(t) = [P(\tau)]^n = \left[1 - \frac{\tau^2}{\hbar^2} \langle H^2 \rangle \right]^n . \tag{4.37}$$

Approximating the initial quadratic time evolution as an exponential, we can simplify this equation to

$$P(t) = \exp\left(-n\, \tau^2 \frac{\langle H^2 \rangle}{\hbar^2} \right) = e^{-\gamma\, t}, \tag{4.38}$$

where the decay rate γ is given by

$$\gamma = \tau\, \frac{\langle H^2 \rangle}{\hbar^2}. \tag{4.39}$$

The time evolution of the system that is repeatedly measured is therefore an exponential decay. The remarkable fact is that the decay rate depends on the measurement interval τ and tends to zero as τ goes to zero

$$\lim_{\tau \to 0} \gamma = 0. \tag{4.40}$$

Reviews of the Quantum Zeno effect can be found in modern textbooks of quantum mechanics [47]. Even though measurement-induced suppression of the dynamics of a two-state driven system has been observed [48, 49], no such effect was ever measured on an unstable system.

Whereas in the previous section we established the non-exponential time-dependence, the focus of this section is the effect of measurements on the system decay rate. The quantity to be measured was the number of atoms remaining trapped in the potential during the tunneling segment. This measurement could be realized by suddenly interrupting the tunneling duration by a period of reduced acceleration a_{interr}, as indicated in Fig. 4.6(a). During this interruption tunneling was negligible and the atoms were therefore transported to a higher velocity without being lost out of the well. This separation in velocity space enabled us to distinguish the remaining atoms from

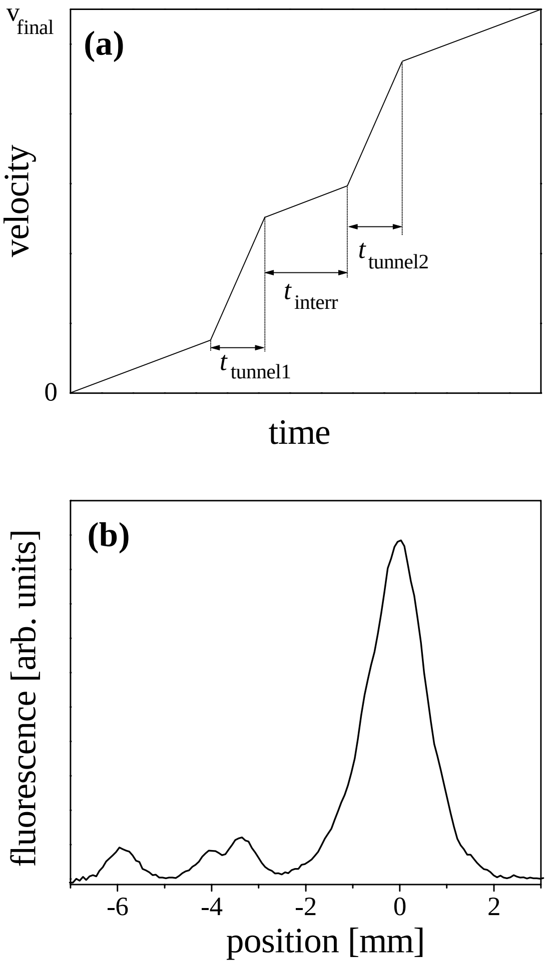

Figure 4.6: Part (a) shows a diagram of the interrupted acceleration sequence. The total tunneling time is the sum of all the tunneling segments. Part (b) shows a typical integrated spatial distribution of atoms after the time of ballistic expansion. The peaks can be identified as in Fig. 4.2. However, the area containing the tunneled fraction of the atoms is now composed of two peaks. Atoms that left the well during the first tunneling segment are offset in velocity from the ones having left during the second period of tunneling. The amount of separation is equal to the velocity increase of the well during the interruption segment.

the ones having tunneled out up to the point of interruption, as can be seen in Fig. 4.6(b). By switching the acceleration back to a_{tunnel} the system was then returned to its unstable state. The measurement of the number of atoms that remained trapped defined a new initial state with the remaining number of atoms as the initial condition. The requirements for this interruption section were very similar to those during the transport section, namely the largest possible acceleration while maintaining negligible losses for atoms in the first band. Hence a_{interr} was chosen to be the same as a_{trans}.

Figure 4.7 shows the dramatic effect of frequent measurements on the decay behavior. The hollow squares indicate the decay curve without interruption. The solid circles in Fig. 4.7 depict the measurement of the survival probability in which after each tunneling segment of 1 μs an interruption of 50 μs duration was inserted. Only the short tunneling segments contribute to the total tunneling time. The survival probability clearly shows a much slower decay than the corresponding system measured without interruption. Care was taken to include the limited time response of the experimental setup into the analysis of the data, as described above. Also indicated as solid lines are quantum mechanical simulations of the decay by numerically integrating Schrödinger's equation for the experimental sequence and determining the survival probability numerically. Further details of the numerical procedure can be found in Appendix A. The simulations contained no adjustable parameters and are in good agreement with the experimental data. We attribute the seemingly larger decay rate for the Zeno experiment as compared to the simulation to the under-estimate of the actual tunneling time.

Recently it was predicted that an *enhancement* of decay can be observed for slightly longer time delays between successive measurements during the non-exponential region. In contrast to the suppressed decay for the Zeno effect this prediction was named the *Anti-Zeno* effect [50, 51, 52]. The shape of the

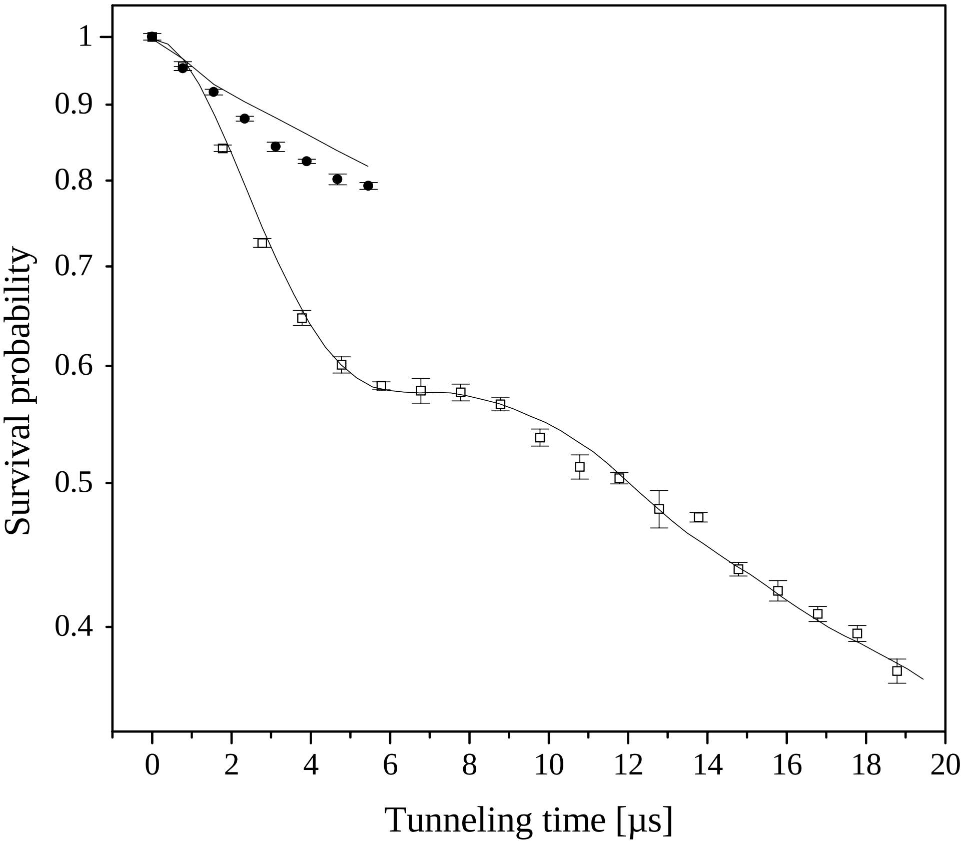

Figure 4.7: Probability of survival in the accelerated potential as a function of duration of the tunneling acceleration. The hollow squares show the non-interrupted sequence, the solid circles show the sequence with interruptions of 50 μs duration every 1 μs. The error bars denote the error of the mean. The data have been normalized to unity at $t_{\text{tunnel}} = 0$ in order to compare to the simulations. The solid lines are quantum mechanical simulations of the experimental sequence with no adjustable parameters. For these data the parameters were: $a_{\text{tunnel}} = 15,000\,\text{m/s}^2$, $a_{\text{interr}} = 2,000\,\text{m/s}^2$, $t_{\text{interr}} = 50\,\mu\text{s}$ and $V_0/h = 91$ kHz.

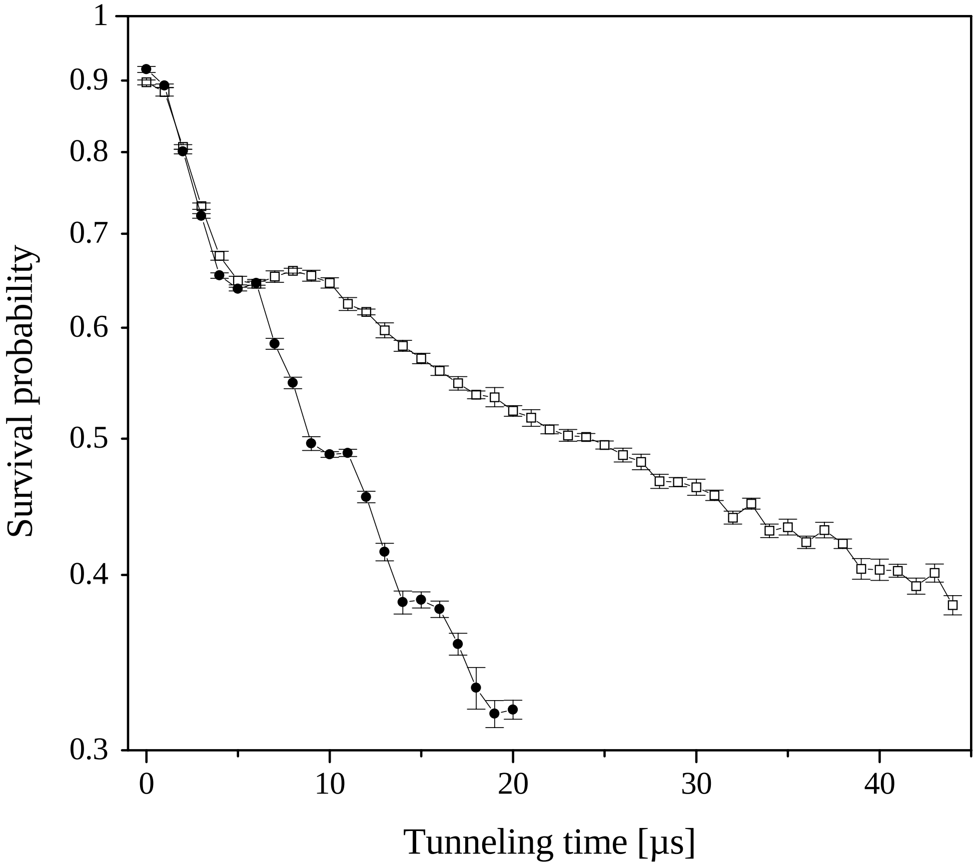

Figure 4.8: Survival probability as a function of duration of the tunneling acceleration. The hollow squares show the non-interrupted sequence, the solid circles show the sequence with interruptions of 40 μs duration every 5 μs. The error bars denote the error of the mean. The experimental data points have been connected by solid lines for clarity. For these data the parameters were: $a_{\text{tunnel}} = 15,000\,\text{m/s}^2$, $a_{\text{interr}} = 2,800\,\text{m/s}^2$, $t_{\text{interr}} = 40\,\mu\text{s}$ and $V_0/h = 116$ kHz.

uninterrupted decay curve in Fig. 4.7 makes this suggestion fairly obvious. After an initial period of slow decay the curve shows a steep drop as part of an oscillatory feature, which for longer time damps away to show the well-known exponential decay. If the system was interrupted right after the steep drop, one would expect an overall decay that is faster than the uninterrupted decay [51]. The solid circles in Fig. 4.8 show such a decay sequence, where after every 5 μs of tunneling the decay was interrupted by a slow acceleration segment. As in the Zeno-case, these interruption segments force the system to repeat the initial non-exponential decay behavior after every measurement. Here, however, the tunneling segments between the measurements are chosen longer in order to include the periods exhibiting fast decay. The overall decay is much faster than for the uninterrupted case, indicated by the hollow squares in the same figure.

The key to observing the Zeno and Anti-Zeno effects is the ability to measure the state of the system in order to repeatedly redefine a new initial state. In our case the measurement is done by separating in momentum space the atoms still left in the unstable state from the ones that decayed into the reservoir. In order to distinguish the two classes of atoms, they must have a separation of at least the size of the momentum distribution of the unstable state, which in our case is the width of the first Brillouin zone of $\Delta p = 2\hbar k_{\mathrm{L}}$. The time it takes for an atom to be accelerated in velocity by this amount is the Bloch period $\tau_{\mathrm{B}} = 2v_{\mathrm{r}}/a_{\mathrm{interr}}$, assuming an acceleration of a_{interr}. An interruption shorter than this time will not resolve the tunneled atoms from those still trapped in the potential and therefore results in an incomplete measurement of the atom number. To investigate the effect of the interruption duration we repeated a sequence to measure the Anti-Zeno effect for varying interruption durations while holding all other parameters constant. Fig. 4.9 displays the results of this measurement, interrupting the decay every 5 μs with an ac-

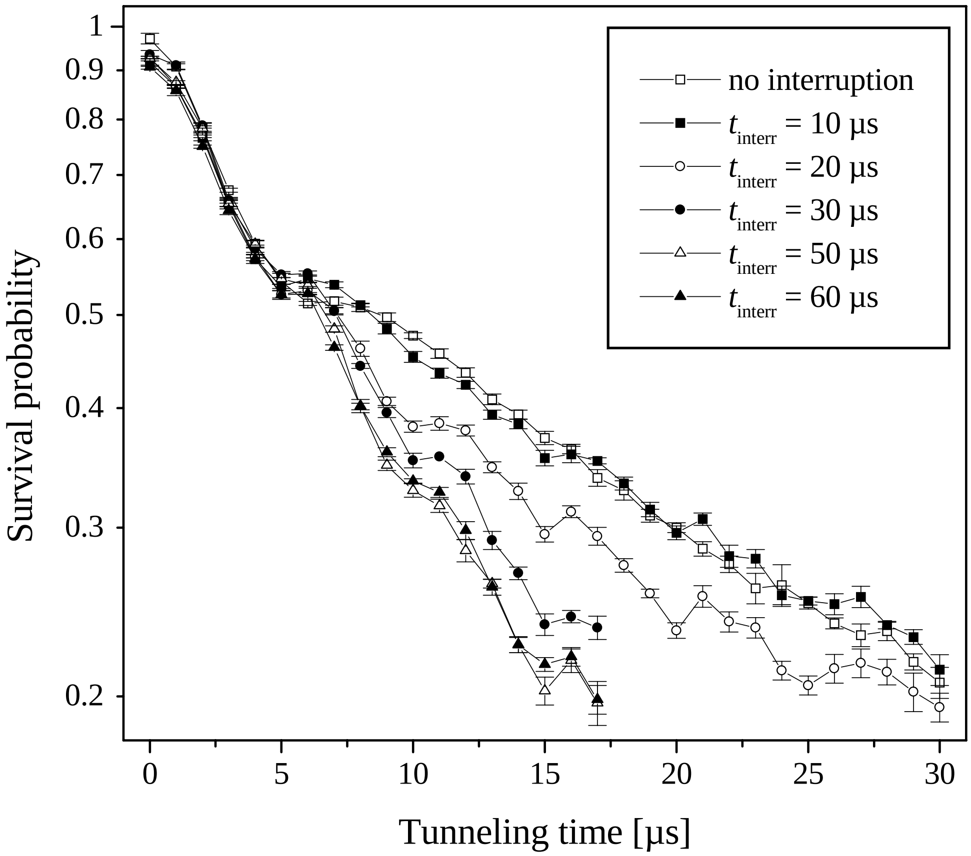

Figure 4.9: Survival probability as a function of duration of the tunneling acceleration. The hollow squares show the non-interrupted sequence, other symbols indicate the sequence with a finite interruption duration after every 5 μs of tunneling. The error bars denote the error of the mean. A further increase of the interruption duration than as indicated does not result in a further change of the decay behavior. The experimental data points have been connected by solid lines for clarity. For these data the parameters were: $a_{\mathrm{tunnel}} = 15,000\,\mathrm{m/s}^2$, $a_{\mathrm{interr}} = 2,000\,\mathrm{m/s}^2$ and $V_0/h = 91$ kHz, leading to a Bloch period of $\tau_{\mathrm{B}} = 30\,\mu$s.

celeration of a_{interr} of $2000\,\text{m/s}^2$. The hollow squares show the uninterrupted decay sequence as a reference. For an interruption duration smaller than the Bloch period of 30 μs the measurement of the atom number is incomplete and has little or no effect. For a duration longer than the Bloch period the effect saturates and results in a complete restart of the decay behavior after every interruption. Even though this method of interruption is not an instantaneous measurement of the state of the unstable system, we can still accomplish the task of redefining the initial state by first switching the system from an unstable to a stable one, then in a finite time perform the measurement and finally switching the system back to being unstable again.

Chapter 5

Recoil-Induced Resonance

In the previous chapters we were investigating the manipulation of atoms with light. We used optical potentials to accelerate atoms or build barriers through which the atoms could tunnel. The main interest was to manipulate the motional state of the atoms. So far we have not investigated at all whether the optical potential undergoes any changes caused by the interaction with the atoms. To change its motional state, an atom needs to acquire the corresponding amount of momentum. The only possible source of momentum is the light beams creating the optical potential. Therefore we should be able to detect the change of momentum of the light beams as a signature of the interaction. If we can gain access to this information encoded in the light, we might be able to extract information about the motional state of the atom.

As described earlier, we measured the momentum distribution by letting the atoms expand and then illuminating them with near-resonant light to record their position. Owing to the dissipative nature of the spontaneous emission process, this method is a destructive measurement. The spatial and momentum distributions undergo severe changes. This precludes, for example, a repeated measurement of the dynamics of an atomic sample without destroying it. Finding a way to measure the distribution while not severely perturbing the sample clears the path for a whole range of interesting experiments, for example, in the field of quantum chaos. Non-destructive measurements of the state of a system are difficult, if not impossible. One can, however, try to affect the system to such a small extent that is acceptable to its further evolution. We call this type of measurement a *least invasive measurement*.

The method of measuring *recoil-induced resonances* seems to be a promising candidate to accomplish this task. This method takes advantage of the effect of the atoms on the optical potential as described above. The exchange of photons between the constituent light beams is measured to obtain information about the momentum distribution of the interacting atomic cloud. This method was first demonstrated with a cold sample of cesium atoms [53, 54]. In our group, results for cesium atoms were obtained recently [55]. However, the experiments performed so far did not meet the requirements for a least invasive measurement. The atomic cloud was pushed away entirely during the interaction and for a subsequent measurement the sample had to be prepared again.

After briefly reviewing the theory of recoil-induced resonances, we will present a refined method that greatly improves the sensitivity of the measurement.

5.1 Quantum optics approach

In Section 1.3.1 we established the effective Hamiltonian for an optical potential created by two overlapping light beams. In this section we calculate a transition rate between momentum states coupled by the interaction. The derivation is based on stimulated Raman transitions as the momentum transfer mechanism. An illustration of this process is indicated in Fig. 5.1. An alternate derivation based on tunneling in the band picture is given in Section 5.2.

In the quantum transport and quantum tunneling experiments, we used

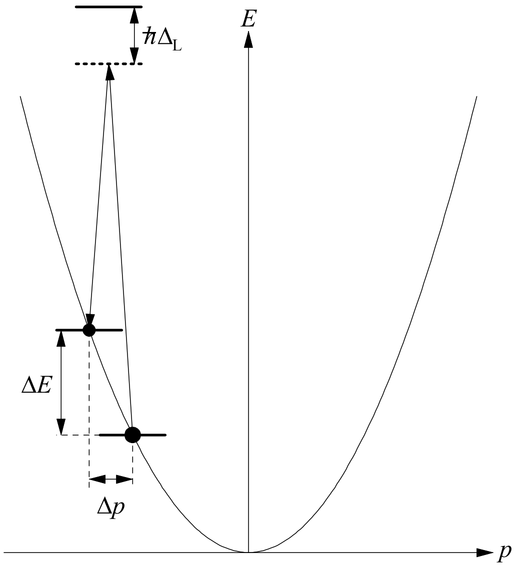

Figure 5.1: Sketch of a stimulated Raman transition between motional states of an atom. For a given frequency difference between the beams two velocity classes are connected by the Raman process. The resonant velocity classes are determined by energy and momentum conservation laws. If an atom undergoes a stimulated Raman transition it transfers a photon from one beam to the other.

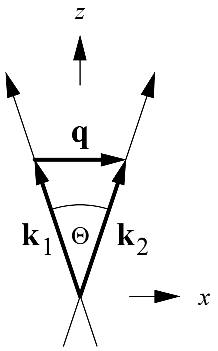

Figure 5.2: Sketch of the beam arrangement for the recoil induced resonance experiments. Two linearly polarized beams with parallel polarization vectors are overlapped enclosing a small angle at the position of the atomic cloud. The vector $\mathbf{q} = \mathbf{k}_2 - \mathbf{k}_1$ is the difference of the wave vectors of the beams.

counterpropagating beams to form an optical potential of period $\lambda_{\mathrm{L}}/2$. In this section we focus on the case of two beams enclosing a small angle Θ as indicated in Fig. 5.2. An atom undergoing a stimulated Raman transition between motional states, as indicated in Fig. 5.1, transfers a photon from one beam into the other. In the case of counterpropagating beams this corresponds to a momentum transfer of $2\hbar k_{\mathrm{L}}$. This can be considered the basic quantization unit of the momentum transfer. For the small-angle configuration, momentum conservation leads to a transfer of

$$\mathbf{p}_{\mathrm{final}} - \mathbf{p}_{\mathrm{initial}} = \hbar\mathbf{k}_2 - \hbar\mathbf{k}_1 = \hbar\mathbf{q}. \tag{5.1}$$

For small angles the absolute value of the momentum difference $\hbar q$ can be significantly smaller than $2\hbar k_{\mathrm{L}}$. This smaller unit of quantization allows us to interact with a given momentum distribution on a scale much finer than the single recoil momentum. The condition for energy conservation reads

$$\frac{p_{\mathrm{final}}^2}{2M} - \frac{p_{\mathrm{initial}}^2}{2M} = \hbar\delta, \tag{5.2}$$

where $\delta = \omega_2 - \omega_1$ as before. For ease of notation we assume that the beams enclose the z-axis and propagate in the x-z plane. The momentum difference q is then

$$q = q_x = 2k_{\mathrm{L}} \sin\frac{\Theta}{2}. \tag{5.3}$$

Combining Eqs. 5.1 and 5.2 results in

$$\mathbf{v}\cdot\mathbf{q} = v_x q = \delta - \frac{\hbar q^2}{2M} = \delta - 4\omega_{\mathrm{r}} \sin^2\frac{\Theta}{2}. \tag{5.4}$$

This equation constitutes a resonance condition for the stimulated Raman process. One can see that there is a one-to-one correspondence of the frequency difference δ and the velocity v_x of the atom undergoing the Raman transition. By choosing δ appropriately, we can select a subset of the atomic ensemble with velocity v_x that will interact resonantly with the light. From Eq. (5.4) it is apparent that only the velocity component along the x-direction is relevant. In the following treatment we restrict ourselves to one dimension.

5.1.1 Quasi-static solution

The Hamiltonian describing the coupling between atoms and the optical potential was derived in Section 1.3.1. We now assume a fixed frequency difference δ between the beams. Equation (1.21) then becomes

$$H = \frac{p^2}{2M} + \hbar \frac{\Omega_1 \Omega_2}{4\Delta_\mathrm{L}} \left(e^{i\mathbf{q}\cdot\mathbf{r}} e^{-i\delta t} + e^{-i\mathbf{q}\cdot\mathbf{r}} e^{i\delta t} \right). \tag{5.5}$$

We now define

$$\Omega_\mathrm{R} = \frac{\Omega_1 \Omega_2}{2\Delta_\mathrm{L}} \tag{5.6}$$

to be the resonant Rabi frequency, which is related to the well depth previously introduced as $V_0 = \hbar\Omega_\mathrm{R}$. The change of notation was done simply for notational convenience. For a given frequency difference δ, the resonance condition in Eq. (5.4) determines the momenta of the two motional states that are resonantly coupled. The separation in momentum of the two coupled states is $\hbar q$. To investigate the time evolution of the system, we can therefore assume the state to be a superposition of the form

$$|\Phi\rangle = \alpha\,|p_0\rangle + \beta\,|p_0 + \hbar q\rangle, \tag{5.7}$$

where the resonant momentum p_0 has been restricted to one dimension. Applying Schrödinger's equation with the Hamiltonian of Eq. (5.5) onto this state results in a set of equations for the amplitudes

$$i\hbar\partial_t \alpha = \frac{p_0^2}{2M}\,\alpha + \frac{\hbar}{2}\Omega_\mathrm{R}\, e^{i\delta t}\beta \tag{5.8}$$

$$i\hbar\partial_t \beta = \frac{(p_0 + \hbar q)^2}{2M}\,\beta + \frac{\hbar}{2}\Omega_\mathrm{R}\, e^{-i\delta t}\alpha. \tag{5.9}$$

This expression can be simplified by the transformations

$$\tilde{\alpha} = \alpha \exp\!\left(\frac{i}{\hbar} \frac{p_0^2}{2M} t \right) \tag{5.10}$$

$$\tilde{\beta} = \beta \exp\!\left(\frac{i}{\hbar} \frac{(p_0 + \hbar q)^2}{2M} t \right). \tag{5.11}$$

Defining the quantity

$$\omega_{\mathrm{res}} = \delta - \frac{p_0 q}{M} - \frac{\hbar q^2}{2M} \tag{5.12}$$

results in the more instructive form for the time evolution equations,

$$i\partial_t \alpha = \frac{\Omega_{\mathrm{R}}}{2}\, e^{i\omega_{\mathrm{res}} t}\, \beta \tag{5.13}$$

$$i\partial_t \beta = \frac{\Omega_{\mathrm{R}}}{2}\, e^{-i\omega_{\mathrm{res}} t}\, \alpha, \tag{5.14}$$

where the tildes have been dropped for notational convenience. It is important to note that the case $\omega_{\mathrm{res}} = 0$ corresponds to the resonance condition of Eq. (5.4). We can see that transitions between the two levels involved can be off-resonantly driven by the interaction. For the time being we assume that only one momentum state is initially populated. Without loss of generality we set $|\alpha(t=0)|^2 = 1$ and $|\beta(t=0)|^2 = 0$. The solution for the population probabilities can easily be found to be

$$|\beta(t)|^2 = \frac{\Omega_{\mathrm{R}}^2}{\Omega_{\mathrm{eff}}^2} \sin^2\!\Big(\frac{1}{2}\Omega_{\mathrm{eff}} t\Big) = 1 - |\alpha(t)|^2, \tag{5.15}$$

where the effective Rabi frequency Ω_{eff} is given by

$$\Omega_{\mathrm{eff}} = \sqrt{\omega_{\mathrm{res}}^2 + \Omega_{\mathrm{R}}^2}. \tag{5.16}$$

It is important to note that the symbols Ω_{R} and Ω_{eff} do not refer to the the same quantities as in Chapter 3, even though the qualitative behavior of the solution in Eq. (5.15) is the same (Rabi oscillations). As can be seen from Eq. (5.15) the population of the two momentum states involved exchanges with an oscillation frequency of Ω_{eff}.

In a realistic situation we have a continuous distribution of momenta within the atomic cloud. Since transitions can be driven off-resonantly we cannot simply restrict the attention to two resonantly coupled states. We have to include the entire atomic distribution to calculate the change of momentum in the light field due to the interaction with the atoms. In order to simplify this complex system, several approximations can be made. First we can assume that different momenta within the distribution are initially uncorrelated. For a thermal distribution in a MOT or molasses this assumption is justified. This allows us to calculate the total transition probability as a sum over the individual transition probabilities of the momentum classes within the distribution. It also justifies the choice for the initial population $|\alpha|^2$ and $|\beta|^2$ used above. For a general case the population for state $|p_0\rangle$ and $|p_0 + \hbar q\rangle$ are

$$\begin{aligned} |\alpha(t=0)|^2 &= N_{p_0} && (5.17) \\ |\beta(t=0)|^2 &= N_{p_0+\hbar q}. && (5.18) \end{aligned}$$

Using an uncorrelated ensemble we can treat this as two separate initial conditions. First we calculate the transition probability assuming one of the levels is unpopulated and then we do the same assuming the other level is empty. The quantity of interest is the total number of exchanged quanta of momentum. For each atom changing its momentum state, one photon is transferred from one beam to the other. If the number of atoms changing their momentum from p_0 to $p_0 + \hbar q$ is the same as the number changing from $p_0 + \hbar q$ to p_0, no net momentum is exchanged. In general the net number of photons exchanged while evolving the two momentum classes is therefore

$$n(p_0) = \frac{\Omega_{\mathrm{R}}^2}{\Omega_{\mathrm{eff}}^2} \sin^2\left(\frac{1}{2}\Omega_{\mathrm{eff}} t\right) \left[N_{p_0+\hbar q} - N_{p_0}\right]. \tag{5.19}$$

Integrating over a continuous distribution of momenta gives the total number of photons transferred as

$$n_{\mathrm{tot}} = N \int_{-\infty}^{\infty} \frac{\Omega_{\mathrm{R}}^2}{\Omega_{\mathrm{eff}}^2} \sin^2\left(\frac{1}{2}\Omega_{\mathrm{eff}} t\right) \left[\Pi(p_0 + \hbar q) - \Pi(p_0)\right] dp_0, \tag{5.20}$$

where $\Pi(p)$ is the momentum distribution function normalized to unity, and N is the total number of atoms interacting with the light. We can further simplify this expression by approximating the difference term of the distribution function. The difference is evaluated at points in momentum space separated by the value $\hbar q$. We can compare this difference with the scale over which the distribution function varies. The distributions we measure are smooth distributions with a typical width of $\Delta p \approx 10\,\hbar k_{\mathrm{L}}$. With an angle of $\Theta = 5°$ we have $\hbar q \approx 0.1\,\hbar k_{\mathrm{L}}$, which is a factor of 100 smaller than the width of the distribution. We can therefore safely assume

$$\Pi(p_0 + \hbar q) - \Pi(p_0) \approx \hbar q \left.\frac{\partial \Pi}{\partial p}\right|_{p=p_0}, \tag{5.21}$$

changing Eq. (5.20) to

$$n_{\mathrm{tot}} = N\hbar q \int_{-\infty}^{\infty} \frac{\Omega_{\mathrm{R}}^2}{\Omega_{\mathrm{eff}}^2} \sin^2\!\left(\frac{1}{2}\Omega_{\mathrm{eff}} t\right) \left.\frac{\partial \Pi}{\partial p}\right|_{p=p_0} dp_0. \tag{5.22}$$

Another approximation can be made with respect to the time-dependent part of the integrand, which we can write as

$$\frac{\sin^2\!\left(\frac{1}{2}\Omega_{\mathrm{eff}} t\right)}{\Omega_{\mathrm{eff}}^2} \equiv f(\omega_{\mathrm{res}}, t) \cdot t. \tag{5.23}$$

For small beam intensities we can disregard the power-dependent term in the expression for the effective Rabi frequency. The function f can then be written as

$$f(\omega_{\mathrm{res}}, t) = \frac{\sin^2\!\left(\frac{1}{2}\omega_{\mathrm{res}} t\right)}{\omega_{\mathrm{res}}^2 t}. \tag{5.24}$$

For large t this function is sharply peaked around the origin with a maximum f_{max} and a width $\delta\omega_{\mathrm{res}}$ of

$$f_{\mathrm{max}} = \frac{t}{4} \tag{5.25}$$

$$\delta\omega_{\mathrm{res}} = \frac{2\pi}{t}. \tag{5.26}$$

We can now compare $\delta\omega_{\mathrm{res}}$ to the width of the distribution of values ω_{res} over which we need to integrate in Eq. (5.22). For small angles in Eq. (5.12) we can neglect terms of second order in q:

$$\omega_{\mathrm{res}} = \delta - \frac{p_0 q}{M}. \tag{5.27}$$

If the momentum distribution we intend to measure has a typical width of Δp then the corresponding width in the distribution of ω_{res} is, according to Eq. (5.27),

$$\Delta\omega_{\text{res}} = \frac{q\,\Delta p}{M}. \tag{5.28}$$

Therefore, for times much larger than the inverse width,

$$t \gg \frac{2\pi}{\Delta\omega_{\text{res}}} = \frac{2\pi M}{q\,\Delta p}, \tag{5.29}$$

the function $f(\omega_{\text{res}}, t)$ can be approximated under the integral as

$$f(\omega_{\text{res}}, t) \approx \frac{\pi}{2}\delta(\omega_{\text{res}}), \tag{5.30}$$

where here the symbol δ denotes the *Dirac delta function.* As mentioned above this approximation is valid if Ω_{R} is sufficiently small. The arguments leading to the substitution with the delta function are strictly correct only if we replace ω_{res} with the effective Rabi frequency Ω_{eff}, but the required limiting value for the area under the curve f remains a good approximation if the additional condition

$$\Omega_{\text{R}} t \ll 1 \tag{5.31}$$

is satisfied. This condition essentially ensures that the incident light is not so strong as to produce a departure of the momentum transfer from the proportionality to the light intensity. Inserting the approximation of Eq. (5.30) into Eq. (5.22) results in

$$n_{\text{tot}} = N\frac{\pi}{2}\,\Omega_{\text{R}}^2\,\hbar q\,t \int_{-\infty}^{\infty} \delta(\omega_{\text{res}})\,\frac{\partial\Pi}{\partial p}\bigg|_{p=p_0} dp_0. \tag{5.32}$$

Using Eq. (5.27), the delta-function can be expressed as

$$\delta(\omega_{\text{res}}) = \frac{M}{q}\,\delta\!\left(p_0 - \frac{M\delta}{q}\right), \tag{5.33}$$

leading to the final expression

$$n_{\text{tot}} = N\frac{\pi}{2}\,\Omega_{\text{R}}^{2}\,\hbar M\,t\int_{-\infty}^{\infty}\delta\left(p_0-\frac{M\delta}{q}\right)\left.\frac{\partial\Pi}{\partial p}\right|_{p=p_0}dp_0 \tag{5.34}$$

$$= N\frac{\pi}{2}\,\Omega_{\text{R}}^{2}\,\hbar M\,t\left.\frac{\partial\Pi}{\partial p}\right|_{p=\frac{M\delta}{q}}. \tag{5.35}$$

The number of photons scattered from one beam to the other varies linearly in time and we can define a scattering rate

$$W=\frac{dn_{\text{tot}}}{dt}=N\frac{\pi}{2}\,\Omega_{\text{R}}^{2}\,\hbar M\left.\frac{\partial\Pi}{\partial p}\right|_{p=\frac{M\delta}{q}}. \tag{5.36}$$

It is worth noting that the procedure of integrating over an ensemble of particles undergoing Rabi oscillations to obtain a transition rate is analogous to the derivation of the Einstein B-coefficient from the solution of the Bloch equations for broad-band incident light.

The derivation of Eq. (5.36) is based on the effect of stimulated Raman transitions between motional states. A more thorough derivation taking into account line broadening mechanisms and polarization effects can be found in [56, 57]. Another approach to deriving this equation is to consider photon scattering on a light-induced grating of atoms. The moving periodic potential changes the momentum distribution of the atoms in a way as to imprint its periodicity on the ensemble in the form of a traveling matter wave. The light beams can then exchange photons by Bragg scattering on the matter wave. A comparison of both approaches is given in [58].

5.1.2 Extension for changing frequency

So far we assumed that the frequency difference δ between the beams is not changing with time. In the experiment we linearly chirp δ in order to sweep the resonance condition for the Raman process through the entire distribution. We can estimate conditions for the chirp rate under which the result in Eq. (5.36) is still applicable.

In order to resolve a resonance of width $\Delta\omega$ with a chirped frequency probe, the time during which the frequency has to hover in the range of the resonance needs to be larger than $\Delta t = 2\pi/\Delta\omega$. This condition can be seen explicitly in the resonance width of Eq. (5.26). During a linear scan $\delta = rt$ the frequency stays in the range $\Delta\omega$ for a time of $\tau = \Delta\omega/r$. Setting $\tau = \Delta t$ gives an expression for the maximum scan rate $r_{\max} = \frac{1}{2\pi}\Delta\omega^2$ which scales as the square of the resonance width to be resolved. Utilizing Eq. (5.27) the maximum scan rate to resolve a momentum distribution of width Δp therefore evaluates to

$$r_{\max} \approx \frac{1}{2\pi}\left(\frac{q\Delta p}{M}\right)^2. \tag{5.37}$$

It is clear from this scaling that for the measurement of distributions with decreasing widths, increased measurement times must be accepted, even though the range of momenta to be sampled is decreasing. Since for scan rates much faster than $r_{\max}$ the approximation Eq. (5.30) no longer holds, we cannot derive a momentum transition rate and very complicated coherent dynamics of the system are to be expected.

Very small scan rates violate another approximation used in the derivation leading to Eq. (5.36). In Eq. (5.20) we assumed a given momentum distribution function $\Pi(p)$. The measurement process, that is the scattering of photons from one beam into the other, changes the momentum distribution of the atoms. Even though the change in momentum for each photon transfer is very small for a small angle between the beams, it will always be present. The time scale over which the population of resonantly coupled momentum states changes is the resonant Rabi frequency Ω_{R}. If, during the scan, the frequency remains in the vicinity of the resonance for the Raman process much longer than the inverse Rabi frequency, a substantial alteration of the momentum distribution is to be expected. The width of the resonance can be estimated to be the frequency difference between two successive resonant Raman transitions. Setting $\Delta p = \hbar q$ in Eq. (5.27) yields a width of

$$\Delta\delta = \Delta p \frac{q}{M} = \frac{\hbar q^2}{M}. \tag{5.38}$$

The time Δt during which the frequency hovers in this range should be much less than the inverse resonant Rabi frequency. A linear scan in frequency $\delta = rt$ therefore leads to a condition for the minimum scan rate

$$r_{\text{min}} \approx \frac{\hbar q^2}{M} \Omega_{\text{R}}. \tag{5.39}$$

For scan rates much slower than r_{min} the momentum distribution will be dynamically changed during the measurement to such an extent as to change the outcome of the measurement itself. This is not to be confused with the heating of the atomic sample due to spontaneous scattering. The change of the momentum distribution described here is inherent to the measurement process and will occur even in the absence of spontaneous scattering.

5.2 Quantum transport approach

It is instructive to derive Eq. (5.36) using the framework of tunneling between Bloch bands. To begin the analysis we consider the interaction beams to form a “moving” standing wave of light as in the previous chapters. The lattice is turned on at a large negative velocity and is decelerated during the frequency scan towards the resonance condition for $p = 0$ at zero velocity. It then is accelerated to a positive velocity as the scan continues. At the time the optical potential is turned on, the atoms have a large velocity compared to the well. They are therefore projected into bands with high band indices. A sketch of the atomic motion through reciprocal space is shown in Fig. 5.3. The initial deceleration of the potential well moves the atomic distribution through reciprocal space towards lower energy (i.e. lower band indices). In doing so the atoms must tunnel through many band gaps. For the parameters used in the experiment, the higher band gaps are so small that the probability for tunneling is essentially unity. During the tunneling no photon transfer occurs between the beams. However, as the atoms approach the lowest band they can undergo Bragg reflections at the first band gap. In this case a photon is removed from one beam and transferred into the other when an atom enters the first Brillouin zone. As the optical potential crosses the point of zero velocity the atoms get transported back to higher band indices.

To simplify the analysis we assume that the majority of atoms tunnel through the lowest band gap and only few undergo a Bragg reflection. This assumption is justified for a large enough acceleration and a small enough well depth. The probability of tunneling from the second into the first band upon entering the first Brillouin zone is equal to the probability of tunneling back into the second band when leaving the Brillouin zone. Therefore only few atoms will Bragg reflect back into the first band after traversing the Brillouin zone. Extended Bloch oscillations of the atoms within the lowest band can be neglected due to the small reflection probability at the first band gap. This condition also ensures that the momentum distribution is not changed significantly during the interaction. The Bragg scattering process transfers a photon in opposite directions for scattering into and out of the first band. The total photon transfer rate is therefore the difference in the rate of scattering at the edges of the first Brillouin zone.

Let $\Pi(p)$ denote the normalized momentum distribution of the atomic ensemble. As we know from the semiclassical equations of motion in Eq. (3.29), the quasi-momentum k varies linearly in time under the influence of a constant

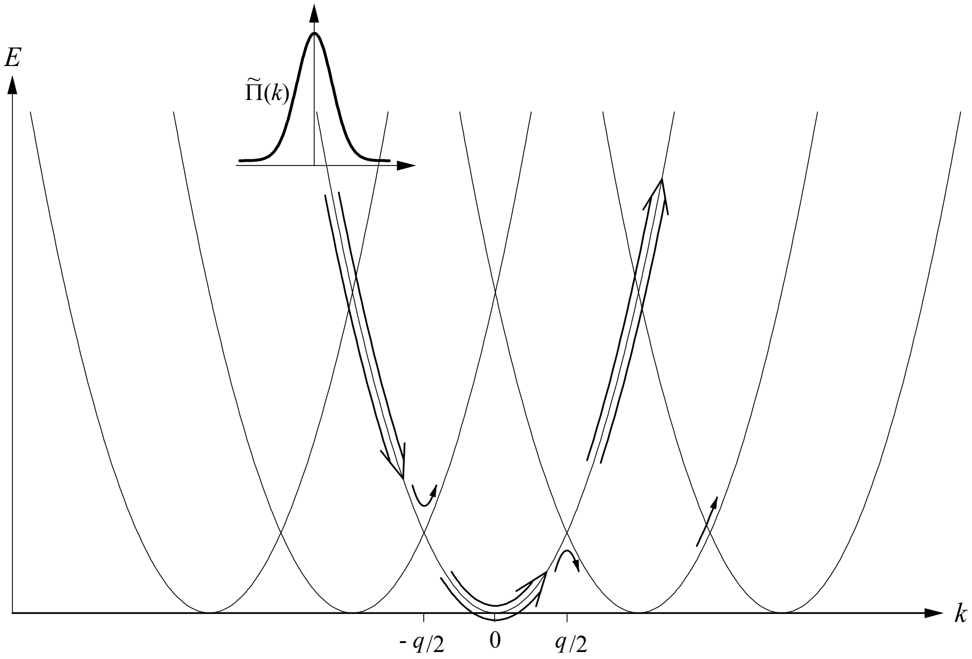

Figure 5.3: Sketch of the dynamics of the atomic motion through reciprocal space. The atomic ensemble starts out in high bands and approaches the lowest band. At the first band gap there is a small probability of undergoing a Bragg reflection, resulting in a change of momentum of $+\hbar q$. Most of the atoms, however, tunnel through the gap and transit the Brillouin zone in the lowest band. Upon exiting the zone they can Bragg reflect again back into the first band, changing their momentum by $-\hbar q$. The remaining atoms then continue their path towards higher band indices.

acceleration:

$$k(t) = k_0 - \frac{1}{\hbar} Mat. \tag{5.40}$$

Transforming the stationary momentum distribution $\Pi(p)$ into the quasi-momentum distribution in the accelerated frame $\tilde{\Pi}(k)$ yields

$$\tilde{\Pi}(k,t) = \hbar\,\Pi(\hbar k - \hbar k(t)) = \hbar\,\Pi(\hbar k - [p_0 - Mat])\,, \tag{5.41}$$

with the normalization $\int \tilde{\Pi}(k,t)dk = \int \Pi(p)dp = 1$. The quantity we need to calculate is the number of particles per unit time undergoing a Bragg reflection at the first band gap. The rate of Bragg scattering upon entering the first Brillouin zone n^- is given by the rate of particles approaching that region multiplied by the probability to follow the band adiabatically instead of tunneling through the gap. If we let P be the probability of tunneling, then the probability of following the band adiabatically is $1 - P$. The scattering rate n^- then evaluates to

$$n^- = N\,\tilde{\Pi}\Big(-\frac{q}{2}, t\Big)\,\frac{dk}{dt} \cdot (1 - P), \tag{5.42}$$

where the quasi-momentum distribution is evaluated at the left edge of the Brillouin zone and N is the total number of atoms participating. The probability of tunneling P is given by Eq. (4.6) as

$$P = e^{-a_\mathrm{c}/a}. \tag{5.43}$$

The critical acceleration a_c for the first band gap is given by

$$a_\mathrm{c} = \frac{\pi}{4}\,\frac{E_\mathrm{g}^2}{\hbar^2 k_\mathrm{L} \sin\frac{\Theta}{2}}, \tag{5.44}$$

where the additional factor of $\sin(\Theta/2)$ as compared to Eq. (4.7) takes into account the angled beam configuration. As derived in Section 3.1 the width of the first band gap E_g is, to first order,

$$E_\mathrm{g} = \hbar\Omega_\mathrm{R}, \tag{5.45}$$

which gives for the critical acceleration

$$a_{\mathrm{c}} = \frac{\pi}{2}\frac{\Omega_{\mathrm{R}}^2}{q}. \tag{5.46}$$

For large acceleration we can write

$$\begin{aligned} n^- &= N\,\tilde{\Pi}\Big(-\frac{q}{2}\Big)\,\frac{dk}{dt}\cdot(1-e^{-a_{\mathrm{c}}/a}) && (5.47)\\ &= N\hbar\,\Pi\bigg(-\frac{\hbar q}{2}-p_0+Mat\bigg)\,\frac{Ma}{\hbar}\,\frac{a_{\mathrm{c}}}{a} && (5.48)\\ &= N\frac{\pi}{2}\frac{M}{q}\Omega_{\mathrm{R}}^2\,\Pi\bigg(-\frac{\hbar q}{2}-p_0+Mat\bigg), && (5.49) \end{aligned}$$

where we approximated $1-e^{-a_{\mathrm{c}}/a}$ as a_{c}/a. Since each atom undergoing Bragg reflection at the first band gap transfers one photon the photon scattering rate W^- is equal to the atomic Bragg scattering rate n^-. The total photon transfer rate W is the difference in the rate of scattering at the left (W^-) and the right (W^+) edge of the first Brillouin zone. Evaluating W^+ in a similar manner we arrive at the expression for W as

$$\begin{aligned} W &= W^+ - W^- && (5.50)\\ &= N\frac{\pi}{2}\frac{M}{q}\Omega_{\mathrm{R}}^2\left[\Pi\bigg(\frac{\hbar q}{2}-p_0+Mat\bigg)-\Pi\bigg(-\frac{\hbar q}{2}-p_0+Mat\bigg)\right] && (5.51)\\ &= N\frac{\pi}{2}\hbar M\Omega_{\mathrm{R}}^2\,\frac{\partial\Pi}{\partial p}\bigg|_{p=p_0-Mat}, && (5.52) \end{aligned}$$

where in the last equation we again approximated the difference term with the derivative. We can express the resonant momentum p in terms of the frequency difference between the beams, making use of the relation $a=r/q$:

$$p = p_0 - Mat = \frac{M}{q}\,(\delta_0 - rt) = \frac{M\delta}{q}. \tag{5.53}$$

This finally leads us to

$$W = N\frac{\pi}{2}\hbar M\Omega_{\mathrm{R}}^2\,\frac{\partial\Pi}{\partial p}\bigg|_{p=\frac{M\delta}{q}}, \tag{5.54}$$

which is identical to Eq. (5.36) derived in the framework of Raman transitions.

5.3 Experimental realization

All experiments on recoil-induced resonances performed to date measured the momentum distribution of an atomic cloud by directly measuring the gain or absorption of one of the beams interacting with the cloud. For this purpose the intensity I of the probe beam passing through the sample was recorded with a photodiode. The absorption coefficient

$$g = \frac{I - I_0}{I_0} \tag{5.55}$$

was then determined by subtracting the value I_0 for the impinging intensity from the signal and by subsequent normalization with I_0. Low-frequency noise and incomplete subtraction of the signals typically limit the resolution for the absorption coefficient of this setup to about 10^{-3}. This forced the experimenters to choose a small value for the detuning of the interaction beams from resonance in order to enhance the strength of the interaction and therefore increase the gain coefficient. However, the drawback of doing so was a substantial number of spontaneous emissions during the interaction.

5.3.1 Frequency modulation spectroscopy

In order to increase the sensitivity of the detection we used a frequency modulation setup as sketched in Fig. 5.4. This method is commonly employed in high resolution spectroscopy. In this setup the probe beam is phase modulated at a frequency ω_{m}. The central frequency is chosen such that the frequency difference δ between the first lower-frequency modulation sideband and the unmodulated pump beam is small. The amplitude E_{i} and intensity I_{i} of the incident probe beam are changed by the interaction with the atoms to

$$E_{\mathrm{f}} = t(\delta)\, E_{\mathrm{i}} \tag{5.56}$$

$$I_{\mathrm{f}} = T(\delta)\, I_{\mathrm{i}}. \tag{5.57}$$

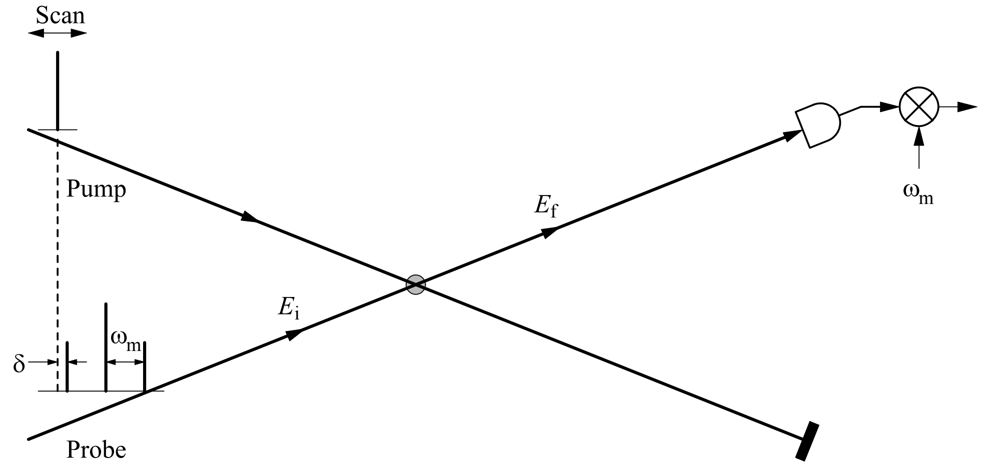

Figure 5.4: Sketch of the frequency modulation setup to increase the detection efficiency. The probe beam is phase modulated at a frequency of ω_m. The lower sideband has a frequency difference of δ with respect to the pump beam. By linearly ramping the frequency of the pump beam, δ is swept through the Raman resonance condition for atoms within the distribution. Frequency dependent absorption of the probe beam passing through the atoms causes an imbalance of the sideband intensities. The resulting intensity variations at the modulation frequency are detected by mixing the photodetector signal with the modulation drive.

These transmission coefficients are related to the gain coefficient by

$$T = t^2 = 1 + g. \tag{5.58}$$

Let us assume the momentum distribution to be measured has a width of order Δp. According to Eq. (5.27) the corresponding width of the distribution of resonance frequencies is $\Delta\omega_{\mathrm{res}} = \frac{q}{M}\Delta p$. If the phase-modulation frequency ω_{m} is chosen much larger than $\Delta\omega_{\mathrm{res}}$ then all but the first lower-frequency sideband of the probe beam are too far from resonance to be affected by the distribution. To analyze the resulting change of amplitude we can write the electric field of the incident modulated probe beam as

$$\begin{aligned} E_{\mathrm{i}} &= E_0\, e^{i(\omega_0 t + m \sin(\omega_{\mathrm{m}} t))} && (5.59) \\ &= E_0\, e^{i\omega_0 t} \sum_{n=-\infty}^{\infty} J_n(m) e^{in\omega_{\mathrm{m}} t}, && (5.60) \end{aligned}$$

where m is the modulation amplitude and J_n is the Bessel function of order n. Each frequency component is now amplified or attenuated according to the amplitude transmission coefficient t to form the final amplitude

$$E_{\mathrm{f}} = E_0\, e^{i\omega_0 t} \sum_{n=-\infty}^{\infty} t(\omega_0 + n\omega_{\mathrm{m}}) J_n(m) e^{in\omega_{\mathrm{m}} t}. \tag{5.61}$$

The resulting intensity for the outgoing probe beam is

$$\begin{aligned} I_{\mathrm{f}} &= \frac{1}{2} c\epsilon_0 \left|E_f\right|^2 && (5.62) \\ &= I_{\mathrm{i}} \sum_{k,l} t(\omega_0 + k\omega_{\mathrm{m}})\, t(\omega_0 + l\omega_{\mathrm{m}}) J_k(m) J_l(m)\, e^{i(k-l)\omega_{\mathrm{m}} t} && (5.63) \\ &= I_{\mathrm{i}} \left[\sum_k t^2(\omega_0 + k\omega_{\mathrm{m}}) J_k^2(m) \right. \\ &\quad \left. + 2 \sum_{k<l} t(\omega_0 + k\omega_{\mathrm{m}})\, t(\omega_0 + l\omega_{\mathrm{m}}) J_k J_l \cos\left([k-l]\omega_{\mathrm{m}} t\right) \right]. && (5.64) \end{aligned}$$

In the absence of the atoms the transmission coefficient is unity, independent of the frequency, and the incident beam is unchanged ($I_{\mathrm{f}} = I_{\mathrm{i}}$). If atoms are present, the last sum in Eq. (5.64) will produce variations in the signal at the modulation frequency ω_m and higher harmonics. The signal at the fundamental frequency ω_m is given as

$$I_{\omega_\mathrm{m}} = 2I_\mathrm{i} \sum_k t(\omega_0 + k\omega_\mathrm{m})\, t(\omega_0 + [k-1]\omega_\mathrm{m}) J_k J_{k-1}. \tag{5.65}$$

The value for $t(\omega_0 + k\omega_\mathrm{m})$ is only appreciably different from unity if the frequency $\omega_0 + k\omega_\mathrm{m}$ is close to the frequency of the pump beam. As discussed above only the first sideband fulfills this condition, so that $t(\delta) = t(\omega_0 - \omega_\mathrm{m}) \neq 1$ is the only term different from unity. Most terms in the sum cancel due to the property $J_{-n} = (-1)^n J_n$ and the remaining terms leave us with

$$\begin{aligned} I_{\omega_\mathrm{m}} &= 2I_\mathrm{i}\,[1 - t(\delta)]\,(J_0 J_1 + J_1 J_2) && (5.66) \\ &= 2I_\mathrm{i}\,[1 - t(\delta)]\,\frac{2}{m} J_1^2. && (5.67) \end{aligned}$$

The factor $\frac{2}{m} J_1^2(m)$ has its global maximum of 0.42 at $m = 1.36$.

The change of power in the probe beam due to gain or absorption in the atomic sample is given by

$$\Delta P_\mathrm{probe} = \hbar\omega_0 W = g P_\mathrm{probe}. \tag{5.68}$$

This gives an expression for the absorption coefficient g

$$g = \frac{\hbar\omega_0}{P_\mathrm{probe}} W. \tag{5.69}$$

For small values of g we see from Eq. (5.58) that $1 - t \approx -g/2$. The maximum change in the integrated power in the probe beam at the modulation frequency ω_m is then

$$\Delta P_{\omega_\mathrm{m}} = 0.42 \cdot 2P_\mathrm{probe}\,[1 - t(\delta)] \approx -0.42\, g P_\mathrm{probe} \tag{5.70}$$

The maximum amplitude of the photocurrent signal corresponding to this change in power is

$$I_\mathrm{sig} = \mathcal{R} \Delta P_{\omega_\mathrm{m}} = 0.42\, \mathcal{R} \hbar\omega_0 W, \tag{5.71}$$

where $\mathcal{R}$ is the photodiode responsivity.

5.3.2 Experimental setup

The experimental apparatus used in this experiment is a refined version of the one described in Chapter 3. The method for preparing the initial cloud of atoms remains essentially unchanged. For this set of experiments the final atomic distribution was approximately Gaussian with a width of $\sigma_x = 0.35$ mm in position and $\sigma_p = 8\,\hbar k_\mathrm{L}$ in momentum. The major change from the previous setup occurred in the preparation of the interaction beams. A schematic of the relevant parts of the experiment is shown in Fig. 5.5.

The frequency scanning arm of the setup provided the pump beam. Whereas in the experiments described in previous chapters the well was turned on at zero velocity, here it was turned on with a velocity corresponding to a value far outside the velocity distribution of the atomic ensemble. The frequency difference was then swept symmetrically through the resonance at a fixed rate. The center frequency of AOM6 was 37.5 MHz and the scan range was typically ±450 kHz. The beam was aligned through the position of the atomic cloud overlapping with the probe beam. The small enclosed angle effectively reduced the atomic recoil frequency and therefore reduced the scan width as compared to the counterpropagating configuration.

The fixed frequency arm of the setup (probe beam) was phase modulated with a Conoptics Model 370 electro-optic modulator (EOM). The EOM was electrically integrated into a resonant circuit to reduce the drive power necessary to obtain the optimum modulation index of $m = 1.36$ at the modulation frequency of 20 MHz. A hand wound coil in a copper enclosure served as the inductive part of the resonator. The tapping position into the coil was optimized for minimum back reflection. The resulting linewidth of 300 kHz and a VSWR of 1.12 was sufficient for this experiment. The adjustment of the drive power for an optimum modulation index was performed by monitoring a heterodyne spectrum. Because the first lower-frequency sideband was to be

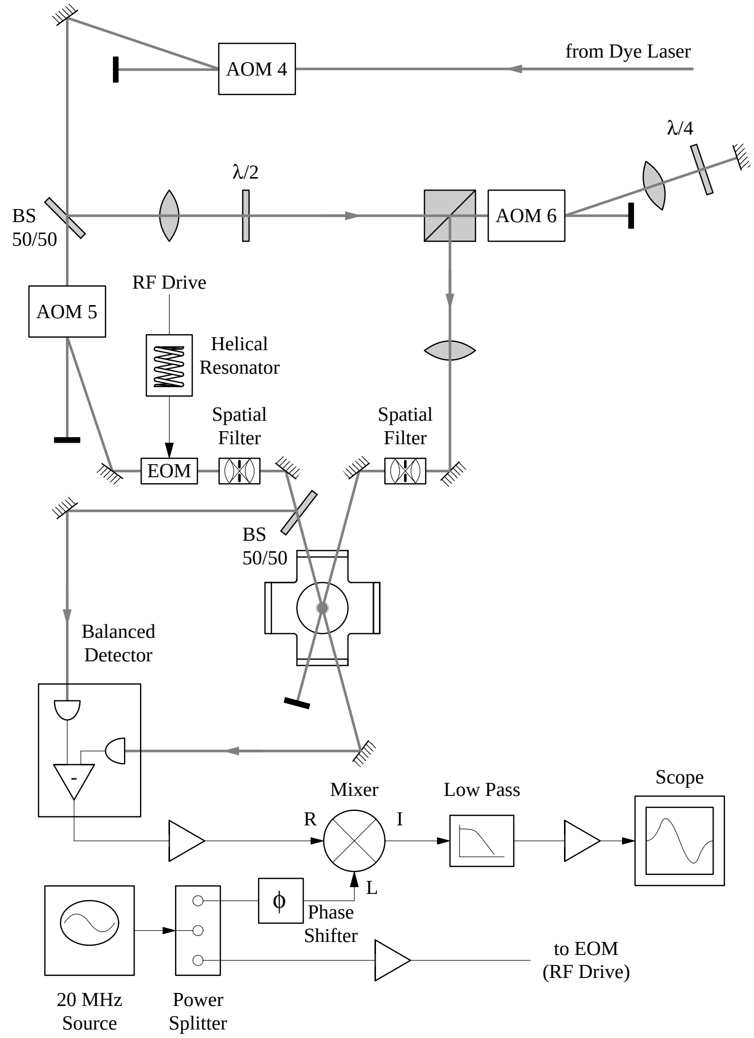

Figure 5.5: Sketch of the interaction beam setup for the recoil induced resonance experiments. The frequency of the pump beam is adjusted by double-passing it through an acousto-optic modulator. An electro-optic modulator provides phase modulation sidebands on the probe beam. To cancel residual amplitude modulation, a balanced photoreceiver is used for detection. The recoil-induced resonance signal at the modulation frequency is extracted and captured on a digitizing oscilloscope for further analysis.

resonant with the atomic ensemble, the AOM in this path (AOM5) was operated at a frequency of 95 MHz. The optical axis of the EOM was aligned to minimize residual amplitude modulation (AM). The ratio of amplitude modulation to the steady state value of the power was about -50 dB, but this value fluctuated by as much as ±5 dB, most likely caused by temperature variations of the crystal. After passing through the EOM the beam was aligned through the position of the atomic cloud overlapping with the pump beam. The enclosed angle between the beams was measured to be $\Theta = 6.3^\circ$ and was dictated mainly by constraints of the vacuum chamber. After leaving the chamber the beam was focused onto a photodetector. As discussed in the previous section absorption or gain in the atomic sample lead to a signal component at the frequency of modulation ω_m. In order to obtain a high signal-to-noise ratio the frequency dependent noise power density at the value for ω_m should be as small as possible. The value $\omega_\mathrm{m} = 20$ MHz was chosen outside the range of significant electronic $1/f$-noise contributions while avoiding regions of increased noise due to other high frequency sources. Because the frequency of the signal to be recorded coincided with the frequency of the residual AM, a further reduction of this effect was necessary. For this purpose half of the power was split from the probe beam before entering the interaction region and both beams were directed onto the input ports of a New Focus Model 1607-AC balanced photoreceiver. Care was taken to equalize the beam intensities and the optical pathlength of both beams. The subtraction of the signals in the photodetector further reduced the AM contribution by 20 dB, suppressing it below the noise level.

A measurement of the integrated noise level of the photodetector at various levels of the incident light power was performed, and the results are shown in Fig. 5.6. The maximum incident power at which the detector operated linearly was 1.5 mW, corresponding to an output voltage of 5 V. For

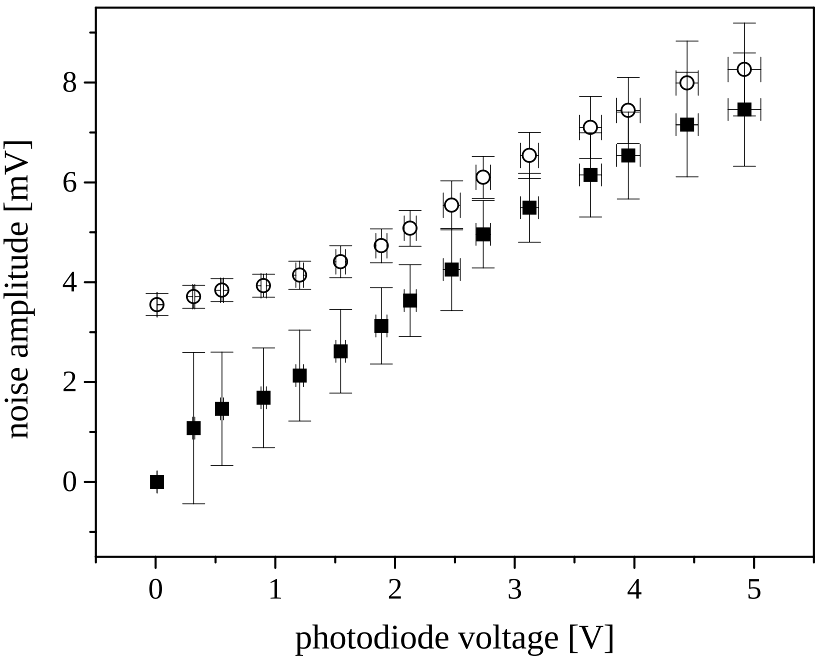

Figure 5.6: Plot of the standard deviation of the photodetector noise for various values of the incident light power. The incident power was converted to a photodetector voltage within the linear operating range. The hollow circles indicate the total noise level σ_{tot}, whereas the solid squares indicate the noise values σ_{light} caused by the light alone. These were calculated using $\sigma^2_{\text{light}} = \sigma^2_{\text{tot}} - \sigma^2_{\text{tot,P=0}}$, where $\sigma_{\text{tot,P=0}}$ is the value for the total noise without incident light.

this maximum power, the noise doubled compared to the value without illumination. The data points indicate that at the maximum power the largest contribution to the noise of the photodetector is due to the shot noise of the incident light.

After being recorded by the photoreceiver, an RF mixer multiplied the amplified signal with a phase-shifted portion of the reference signal. The output was a DC level proportional to the amplitude of the signal at the modulation frequency. Higher harmonics were eliminated by a low pass filter with a cut-off frequency of 200 kHz. After another amplification stage the signal was captured by a digitizing oscilloscope and transferred to the control computer for analysis.

5.4 Momentum measurements

Figure 5.7 shows an example of a single-shot, recoil-induced resonance trace. No averaging was performed to obtain this signal. In this experiment an integrated power of $P_{\text{pump}} = 5$ mW in the pump beam was focused onto the atoms. The spot size at the position of the atomic cloud was $w_{\text{pump}} = 340\ \mu$m. The corresponding values for the probe beam were $P_{\text{probe}} = 0.72$ mW and $w_{\text{probe}} = 220\ \mu$m. The detuning from resonance was $\Delta_{\text{L}}/2\pi = 1$ GHz. The frequency difference of the two beams was scanned over 900 kHz in 200 μs.

We can now compare the acquired signal to the theoretical approximation derived earlier. The initial condition of the atomic cloud before the RIR interaction was a Gaussian distribution of momenta,

$$\Pi(p) = \frac{1}{\sqrt{2\pi}\sigma_p} e^{-\frac{p^2}{2\sigma_p^2}}, \tag{5.72}$$

with $\sigma_p = 8\,\hbar k_{\text{L}}$. This distribution had a size of roughly $\sigma_x = 0.35$ mm and contained about $1.5 \cdot 10^6$ atoms. The expression for the RIR signal in Eq. (5.36)

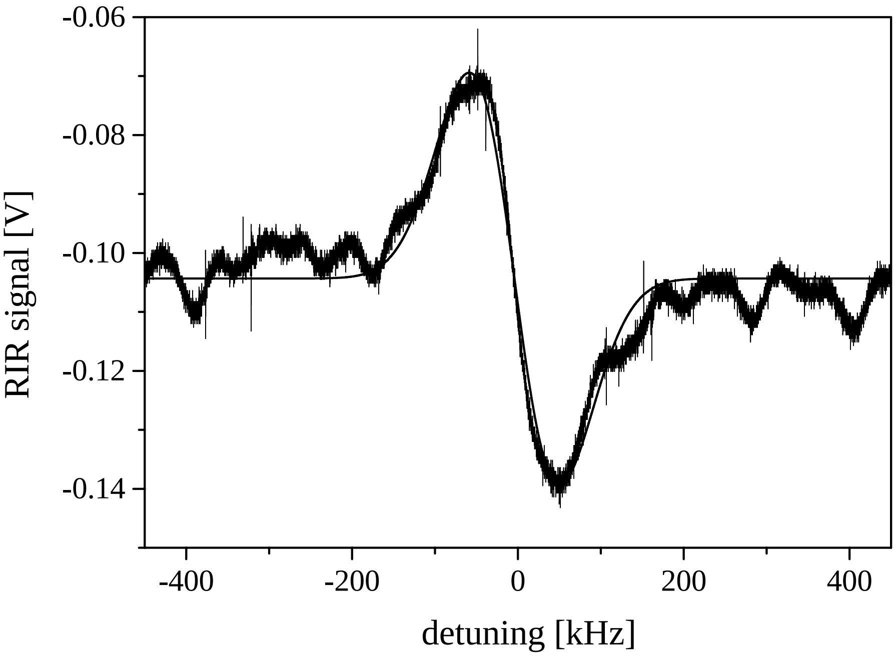

Figure 5.7: An example of a single-shot, recoil-induced resonance trace of the atomic distribution after being released from the MOT. Indicated also is a best fit of a derivative of a Gaussian curve to the experimental data. The fitted value for the width of the momentum distribution is $\sigma_p = 10\,\hbar k_{\mathrm{L}}$.

is

$$
\begin{aligned}
W &= N\sqrt{\frac{\pi}{8}}\,\Omega_{\mathrm{R}}^2\,\frac{\hbar M^2\delta}{q\sigma_p^3}\,e^{-\frac{1}{2}\left(\frac{M\delta}{q\sigma_p}\right)^2} && (5.73)\\
&= N\sqrt{\frac{\pi}{8}}\,\Omega_{\mathrm{R}}^2\,\frac{1}{8\omega_{\mathrm{r}}^2\sin(\Theta/2)}\,\frac{\delta}{n_{\mathrm{rec}}^3}\,e^{-\frac{1}{2}\left(\frac{\delta}{4n\omega_{\mathrm{r}}\sin(\Theta/2)}\right)^2}, && (5.74)
\end{aligned}
$$

where we expressed the width of the momentum distribution as $\sigma_p = n_{\mathrm{rec}}\hbar k_{\mathrm{L}}$. The maximum value W_{max} for the scattering rate in Eq. (5.74) occurs when the frequency difference has a value of $\delta = \frac{q\sigma_p}{M}$ resulting in

$$W_{\mathrm{max}} = N\sqrt{\frac{\pi}{8}}e^{-1/2}\,\Omega_{\mathrm{R}}^2\,\frac{1}{2n_{\mathrm{rec}}^2\omega_{\mathrm{r}}}. \tag{5.75}$$

To optimize the RIR signal the interaction beam size should be comparable to the size of the atomic distribution. For much smaller beams only a fraction of the atoms interact with the light. Choosing them much larger lets most of the beams miss the atoms without interacting, unnecessarily increasing the light induced noise in the photodetector. Integration over the momentum distribution of width σ_x taking into account the Gaussian profile of the beam intensity decreases the maximum scattering signal by a factor

$$\eta_{\mathrm{Gauss}} = \left(1 + \frac{4\sigma_x^2}{w_{\mathrm{probe}}^2} + \frac{4\sigma_x^2}{w_{\mathrm{pump}}^2}\right)^{-1}. \tag{5.76}$$

Using Eq. (5.71) for the amplitude of the photocurrent signal at the modulation frequency yields

$$I_{\mathrm{max,rms}} = 0.42\,\frac{1}{\sqrt{2}}\sqrt{\frac{\pi}{8}}e^{-1/2}N\eta_{\mathrm{Gauss}}\,\mathcal{R}\,\hbar\omega_0\,\Omega_{\mathrm{R}}^2\,\frac{1}{2n_{\mathrm{rec}}^2\omega_{\mathrm{r}}}. \tag{5.77}$$

The photodiode used had a responsivity of $\mathcal{R} = 0.4$ A/W and a transimpedance gain of 700 V/A. Tracing the electronic gain of the signal through the setup resulted in a voltage gain of $V_{\mathrm{output}}/V_{\mathrm{max,rms}} \approx 1900$. Combining Eq. (5.77) with the values for the experimental parameters yields an expected maximum change of power in the probe beam of $\Delta P_{\mathrm{probe}} = 0.4\,\mu$W and a corresponding signal of $V_{\mathrm{output}} = 60$ mV. The experimental trace has a maximum value of roughly $V_{\text{output}} = 30$ mV. Considering the difficult calibration of the system and the strong dependence of the signal on the optical alignment the theoretical approximation agrees quite well with the experiment.

We can also obtain a theoretical value for the signal-to-noise ratio. The dominant noise source for the signal is the inherent fluctuation of the number of photons in the probe beam (shot noise). The noise current of the photodiode integrated over a bandwidth B is given by

$$I_{\text{noise}} = \sqrt{2eI_{\text{dc}}B}, \tag{5.78}$$

where e is the electron charge and $I_{\text{dc}} = \mathcal{R}P_{\text{probe}}$ is the DC photocurrent. The integration bandwidth is determined by the low-pass filter in the electronic setup and was set to $B = 200$ kHz. Comparing I_{noise} to the value for the signal photo current in Eq. (5.77) leads to a signal-to-noise ration of $\text{S/N} \approx 15$, which is not too far from the signal-to-noise ratio of the trace in Fig. 5.7.

Also indicated in Fig. 5.7 is a least-squares fit of a curve, as given in Eq. (5.74), to the experimental data. The best-fit value for the temperature of the atomic cloud was $\sigma_p = 10\,\hbar k_{\text{L}}$. This value is slightly higher than the value $\sigma_p = 8\,\hbar k_{\text{L}}$ measured with the ballistic-expansion method. We attribute this to the measurement-induced heating described earlier.

To investigate this heating effect further we acquired RIR signals for various detunings of the interaction beams from resonance. Figure 5.8(a) shows the fitted value of σ_p in units of the single photon recoil momentum. For comparison, the horizontal line indicates the measurement of the temperature using the ballistic-expansion method. Part (b) of the same figure shows the fitted value for the amplitude of the RIR signal and the amplitude predicted from the theoretical approximation using Eq. (5.77).

It is important to note that for the RIR scans from which the data in Fig. 5.8 were obtained, the repump beam was left on during the interaction.

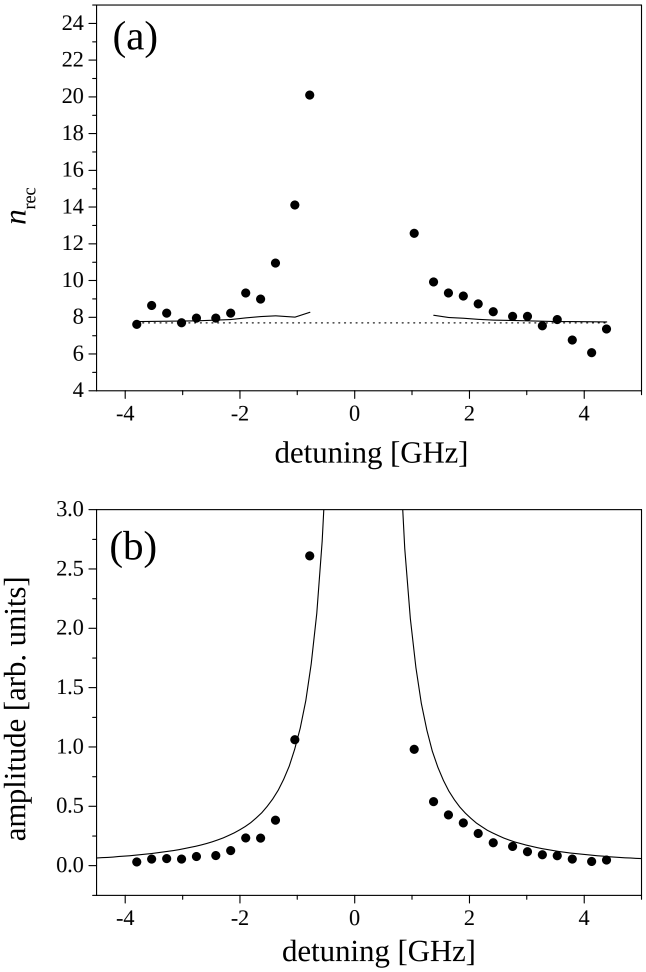

Figure 5.8: Dependence of the RIR signal parameters on the detuning of the interaction beams relative to the transition $(S_{1/2}, F = 2) \rightarrow (P_{3/2}, F' = 3)$. The data points in part (a) show the fitted value of $n_{\rm rec}$ (σ_p in units of the single photon recoil momentum). As a comparison the horizontal dotted line indicates the value for $n_{\rm rec}$ obtained with the method of ballistic expansion. The solid line indicates the momentum variance of the cloud that one could expect for the cloud being heated due to spontaneous emission alone. The data points in (b) show the fitted value of the amplitude. Indicated as a solid line is the dependence predicted from the theoretical approximation.

For beam frequencies that were close to resonance for a particular hyperfine level of the ground state, the absence of the repump beam allowed the atoms to fall into the other hyperfine ground state, for which the light was much further detuned. For detunings larger than roughly 1 GHz the presence of the repump beam did not change the RIR signal shape.

The dominant heating effect present in the experiments on RIR performed previously was the large number of spontaneous emissions during the interaction. A ballistic-expansion measurement in the direction in which the RIR measurement was performed was not possible due to limited optical access for the CCD camera. To quantitatively study the amount of heating due to spontaneous emission in our system, we determined the momentum that the atomic cloud acquired during the push. For this purpose we placed the CCD camera so that it was able to record the displacement of the atomic cloud in the direction of the interaction beams after a time of free expansion. The measurement of the mean acquired momentum in this direction enabled us to estimate the number of spontaneous emissions. Each absorbed photon leads to a momentum kick of $\hbar k_{\mathrm{L}}$ given to the atom. When an atom decays into the lower hyperfine ground state, it will immediately be pumped back to the excited state by the repump light . Since the repump beams illuminate the atomic sample from all directions, the absorption of photons from these beams does not lead to an average displacement of the cloud. However, this process will contribute to the heating of the sample. Assuming an isotropic emission we can then estimate the temperature increase due to the random recoil momentum kicks. The temperature one could expect caused solely by this heating effect is indicated as a solid line in Fig. 5.8(a). One can see that the measured temperature increase can not be accounted for by spontaneous emission alone.

A few simple arguments can give us an estimate for the size of the heating effects. First we consider the heating inherent to the measurement. The energy transferred to the atom during a single Raman transition is $E = \hbar\delta$. Integrating over the whole sweep duration yields the average energy transferred per atom:

$$\begin{aligned} E_{\mathrm{inc,measure}} &= \int W(\delta)dt = \frac{1}{r}\int W(\delta)d\delta && (5.79)\\ &= \frac{4\pi}{r}\Omega_{\mathrm{R}}^2\,\hbar\omega_{\mathrm{r}}\sin^2(\Theta/2)\,. && (5.80)\end{aligned}$$

This energy transfer leads to an increase in the momentum variance as

$$\sigma^2_{p,\mathrm{final}} = \sigma^2_{p,\mathrm{initial}} + 2ME_{\mathrm{inc,measure}}. \tag{5.81}$$

The heating due to spontaneous emissions can be estimated by determining the spread in momentum caused by random emission of photons. Since we are only interested in the spread in one dimension, the increase in the variance after n_{sc} scattering events is [54]

$$\sigma_{\mathrm{inc,spont}} = \frac{2}{5}\sqrt{n_{\mathrm{sc}}}\,\hbar k_{\mathrm{L}}. \tag{5.82}$$

The number of scattered photons can be estimated according to Eq. (1.35) as

$$n_{\mathrm{sc}} = 2\cdot\left(\frac{\Gamma}{2}\right)\frac{S}{1+S+4(\Delta_{\mathrm{L}}/\Gamma)^2}\cdot\tau_{\mathrm{int}}, \tag{5.83}$$

where τ_{int} is the duration of the interaction. The first factor of two in this equation accounts for the fact that photons can reach the lower hyperfine ground state. From there they are removed immediately by the repump beam, adding to the number of spontaneously scattered photons. For the parameters used to obtain the data in Fig. 5.8, the energy increase due to the measurement is about three times larger than the increase due to spontaneous emission for the range of detunings measured.

To test the limits of the semiclassical derivation given in Section 5.1.2 we changed the scan rate of the frequency difference over a wide range. Experimental traces for the RIR signals for various scan rates are displayed in

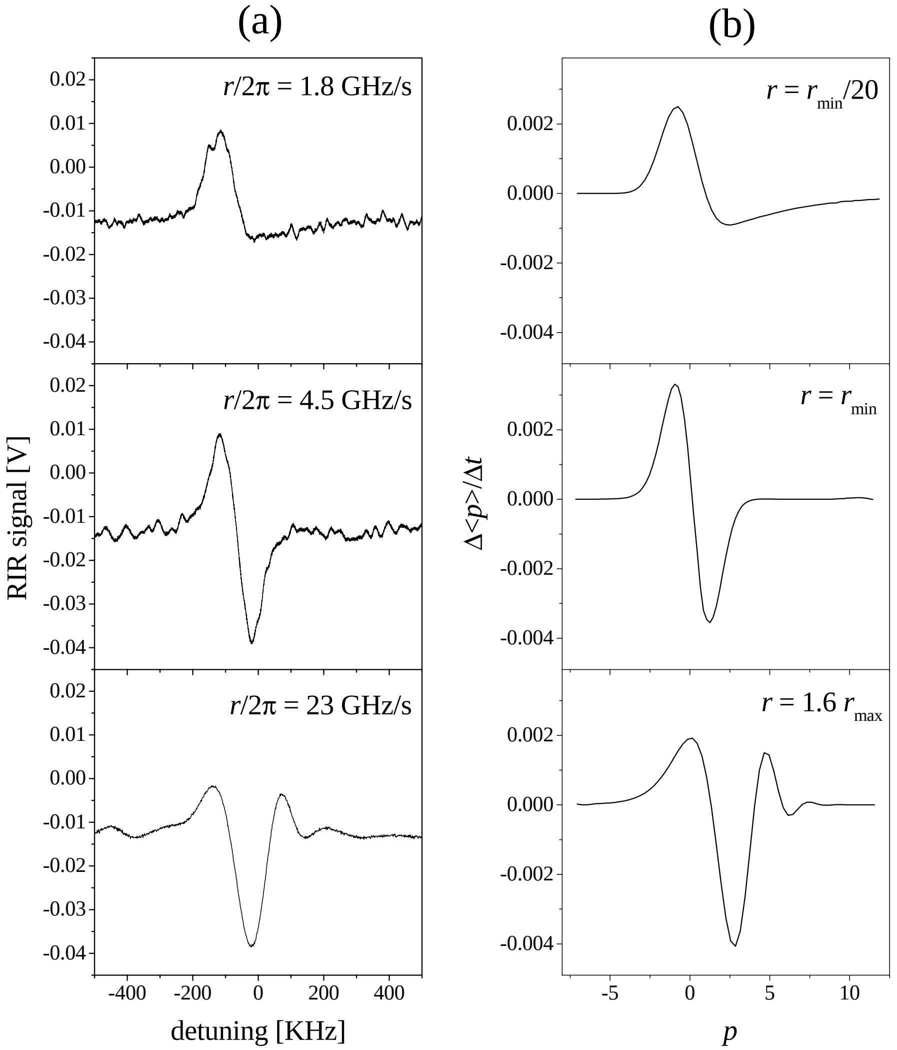

Figure 5.9: The left panels show experimental RIR traces for different scan rates. Each trace is an average over 20 acquisitions. The scan direction was from negative to positive detunings. The frequency range of the scan was held constant at $\delta\nu = 900$ kHz, but the scan time was changed to produce the given scan rate. The right panels show quantum numerical simulations for scan rates that are smaller (top), within (middle) or outside (bottom) of the range $[r_{\text{min}}, r_{\text{max}}]$. It is important to point out that the parameters for the experimental runs and the numerical simulations are not the same.

the left panel of Fig. 5.9. For all traces the scan direction was from negative to positive detunings. The estimates for the minimum and maximum scan rates as given by Eqs. (5.39) and (5.37) for the parameters used in the experiments give $r_{\min} \approx r_{\max} \approx (2\pi) \cdot 10$ GHz/s. This indicates a small range of scan rates for which the expression for the RIR signal is applicable.

For the top panel in Fig. 5.9, the scan rate was chosen much smaller than $r_{\min}$. The trace shows a strong asymmetry in the shape. The first (positive) peak is large and localized whereas the second (negative) peak after the center of the resonance is small and returns to zero very slowly with a long tail. The exchange of momentum within the atomic cloud always tends to increase the momentum spread of the distribution. At the start of the frequency scan the momentum is transferred from the central regions towards the wing in the direction opposite to the scan direction. For small scan rates the light interacts with a given velocity class for a time long enough to alter the distribution significantly. Off-resonant interactions let the atoms transfer momentum even before the light reaches the corresponding resonance condition. This transfers most of the atoms prior to the frequency difference reaching zero for a resonance at $p = 0$. Past this point the momentum transfer occurs in the direction of the scan direction. The atoms which have not been transferred too far out of resonance can be ‘dragged’ along in the scan direction to very high momenta, explaining the long tail in the RIR signal trace. For the case of a fast scan (bottom panel) no such simple explanation could be found. The frequency is broadened substantially and the light is interacting with a large part of the ensemble simultaneously. The RIR traces show an oscillatory behavior after the frequency passes through the resonance.

We also compared the shape of the RIR signals to numerical quantum mechanical simulations. For the case of small angles in the RIR setup the momentum quantization unit $\hbar q$ was much smaller than the width in momentum of the real atomic sample. Therefore numerical simulations with actual experimental parameters required the solution of a set of ordinary differential equations of prohibitively large dimension, as discussed in Appendix A. Since we were not intending to extract quantitative information from the simulations we restricted the simulation runs to distributions much narrower than the experimental ones. Because the scaling arguments for the scan rates involve the width of the distribution the relative scan rates between experiment and simulation cannot be directly compared.

Appendix

Appendix A

Numerical Methods

A.1 Scaling the effective Hamiltonian

Throughout this dissertation, most physical quantities have been quoted in SI units. However, sometimes it is more convenient to express quantities in *natural units*. An example of this practice is to quote momentum in units of the single photon recoil momentum $\hbar k_{\mathrm{L}}$. This practice greatly simplifies the notation and facilitates the formulation of computer simulations [59, 60] as well as the analytic, mathematical analysis. Moreover, these units reflect the natural scales of the system.

The most general one-dimensional effective Hamiltonian used in this work is given in Eq. (1.25) as

$$H(x,p) = \frac{p^2}{2M} + V_0 \cos\left(qx - \phi(t)\right). \tag{A.1}$$

We define our new units by the relationships

$$\begin{aligned} H' &= \frac{H}{E_{\mathrm{u}}} && \text{(A.2)} \\ V_0' &= \frac{V_0}{E_{\mathrm{u}}} && \text{(A.3)} \\ t' &= \frac{t}{t_{\mathrm{u}}} && \text{(A.4)} \\ p' &= \frac{p}{p_{\mathrm{u}}} && \text{(A.5)} \\ x' &= \frac{x}{x_{\mathrm{u}}}, && \text{(A.6)} \end{aligned}$$

where the parameters measured in SI units are unprimed and their counterpart measured in natural units are primed. The obvious choice for the scaling of the position variable is $x' = qx$. For the scaling of the remaining variables we need to pay attention to some constraints of the transformation. First, the transformation needs to be canonical in order to preserve the validity of Hamilton's equations of motion. Second, the commutator $[x, p] = i\hbar$ should also have a simple form in the natural units of the system; for convenience we can choose $[x', p'] = i$. These conditions define all of the scaling parameters above to be

$$\begin{aligned} E_\mathrm{u} &= 8\hbar\tilde{\omega}_\mathrm{r} && \text{(A.7)} \\ t_\mathrm{u} &= \frac{1}{8\tilde{\omega}_\mathrm{r}} && \text{(A.8)} \\ p_\mathrm{u} &= \hbar q && \text{(A.9)} \\ x_\mathrm{u} &= \frac{1}{q}. && \text{(A.10)} \end{aligned}$$

The unit of momentum $\hbar q$ is the change of momentum due to a single photon transfer from one beam to the other, and $1/q$ is the periodicity of the potential divided by 2π. The recoil energy $\hbar\tilde{\omega}_\mathrm{r}$ is defined as the kinetic energy of an atom moving with half the momentum transferred during an exchange of photons, with

$$\tilde{\omega}_\mathrm{r} = \frac{\hbar q^2}{8M} = \frac{\hbar {k_\mathrm{L}}^2}{2M} \sin^2 \frac{\Theta}{2}. \tag{A.11}$$

With this change of units, the Hamiltonian of Eq. (A.1) becomes, after dropping the primes,

$$H(x, p) = \frac{p^2}{2} + V_0 \cos(x - \phi(t)), \tag{A.12}$$

and the Schrödinger equation becomes

$$i\frac{\partial}{\partial t}|\psi\rangle = H|\psi\rangle. \tag{A.13}$$

With a unitary transformation we can write the Hamiltonian in Eq. (A.12) in a form that is more convenient for numerical work. We can choose a translation in position space by the amount $\phi(t)$, combined with a phase shift of $\eta(t)$, described by the unitary transformation operator

$$U(t) = e^{i\phi(t)p} e^{-i\eta(t)}. \tag{A.14}$$

Applying this transformation to the Hamiltonian and choosing $\dot{\eta} = \dot{\phi}^2/2$ yields

$$H = \frac{\left(p - \dot{\phi}(t)\right)^2}{2} + V_0 \cos x, \tag{A.15}$$

where the dot denotes a time derivative. For example, the Hamiltonian corresponding to an accelerated standing wave with an added probe term as used in the Wannier-Stark experiments would be

$$H = \frac{(p - at - m_{\mathrm{p}}\omega_{\mathrm{p}} \sin(\omega_{\mathrm{p}} t))^2}{2} + V_0 \cos x. \tag{A.16}$$

A.2 Time evolution

In this section, we calculate the time evolution of the system by evolving a distribution in momentum space, following the procedure outlined by Georgakis [60]. Assuming an initially uncorrelated distribution we can evolve each momentum eigenstate separately and add the resulting momentum probability distribution incoherently. If we match the momentum distribution to a given experimental situation, we will most likely have a mismatch in the spatial extent. However, for cold but spatially extended atomic clouds, this approach is justified.

The natural unit for the transfer of momentum, stimulated by the interaction, is $\Delta p = 1$. To solve Schrödinger's equation (A.13) for a given momentum p_0, we expand the eigenstate for p_0 in the basis set of states spaced by Δp:

$$\Psi_x(p_0, t) = \sum_n A_n(p_0, t)\, e^{i(p_0+n)x}. \tag{A.17}$$

The momentum representation of this state is given by

$$\begin{aligned}\Psi_p(p_0,t) &= \frac{1}{\sqrt{2\pi}}\int \Psi_x(p_0,t)e^{-ipx} && \text{(A.18)}\\ &= \sum_n A_n(p_0,t)\,\delta(p-[p_0+n])\,. && \text{(A.19)}\end{aligned}$$

Inserting Eq. (A.17) into Eq. (A.13) and projecting the result onto the momentum eigenstates yields the evolution equation for the coefficients $A_n(p_0,t)$

$$\begin{aligned}i\partial_t A_n(p_0,t) &= \frac{1}{2}\left(p_0+n-\dot{\phi}(t)\right)^2 A_n(p_0,t)\\ &\quad+\frac{V_0}{2}\left[A_{n+1}(p_0,t)+A_{n-1}(p_0,t)\right]. && \text{(A.20)}\end{aligned}$$

We now assume an initial distribution of momenta $\Pi(p,t=0)$. It is instructive to write the initial distribution in terms of the momentum eigenstates in Eq. (A.19)

$$\Pi(p,0)=\int \Pi(p_0,0)\left|\Psi_p(p_0,0)\right|^2 dp_0. \tag{A.21}$$

The time-evolved distribution can be obtained in a similar fashion by (incoherently) integrating over the time-evolved probabilities of the momentum states with the initial distribution as the weight function

$$\Pi(p,t)=\int \Pi(p_0,0)\left|\Psi_p(p_0,t)\right|^2 dp_0. \tag{A.22}$$

Inserting Eq. (A.19) into this equation yields

$$\begin{aligned}\Pi(p,t) &= \int \Pi(p_0,0)\left|\sum_n A_n(p_0,t)\,\delta(p-[p_0+n])\right|^2 dp_0 && \text{(A.23)}\\ &= \int \Pi(p_0,0)\sum_n \left|A_n(p_0,t)\right|^2\,\delta(p-[p_0+n])\,dp_0 && \text{(A.24)}\\ &= \sum_n \left|A_n(p-n,t)\right|^2\Pi(p-n,0). && \text{(A.25)}\end{aligned}$$

Note that in order to obtain the distribution $\Pi(p,t)$, all the plane waves that are within the range of the initial momentum distribution need to be propagated.

For the recoil-induced resonance signals as described in Chapter 5, the quantity measured in the experiment is the number of transferred photons. In order to extract this signal from the simulation we can calculate the mean momentum of the sample

$$\begin{aligned} \langle p\rangle_t &= \int p\,\Pi(p,t)dp && \text{(A.26)}\\ &= \int p\sum_n |A_n(p-n,t)|^2\,\Pi(p-n,0)dp && \text{(A.27)} \end{aligned}$$

at times t and $t+\Delta t$, where Δt is small. The photon transfer rate can then be approximated as

$$W(t) = \frac{\langle p\rangle_{t+\Delta t} - \langle p\rangle_t}{\Delta t}. \tag{A.28}$$

The numerical integration of Eq. (A.20) with the appropriate expression for the time-dependent phase of the standing wave $\phi(t)$ was programmed in ANSI-C and was performed on standard PC's. When $\phi(t)$ is chosen to correspond to a velocity profile of an acceleration sequence as used in the experiments (for example as in Fig. 3.5), care must be taken to avoid discontinuous phase jumps of $\phi(t)$ when switching between accelerations. To integrate Eq. (A.20) we used the 'Numerical Recipes' *Burlisch-Stör* integration routine [61]. For the equation at hand, this routine proved to be more robust than the conventional Runge-Kutta method. Performance-optimized ODE solvers for this type of ordinary differential equation were not tested here.

A.3 Initial conditions

For most problems considered here it is advantageous to expand the initial condition not in terms of plane waves but in terms of superpositions of plane waves. A plane wave evolving in a periodic lattice will spread due to Bloch tunneling. However, if we choose a superposition of plane waves corresponding to an eigenstate of the lattice, no change over time will occur. This procedure is especially suited for the calculation of the Rabi oscillations between Bloch bands, since, in this case, the lattice itself is stationary. As an initial state we choose a Bloch eigenstate in a certain band for a given quasi-momentum. This state can be evolved in time with the method described above. The resulting state can then simply be projected back onto the initial state to obtain the probability of remaining within that state during the evolution. In the case of an accelerating potential, the quasi-momentum, for which the eigenstate was obtained, changes with time. Therefore, the projection method produces an autocorrelation function which does not directly yield the survival probability in the specified band any more [35].

To calculate the eigenfunction $\Psi_n(k)$ and eigenenergy $E_n(k)$ of a Bloch state we first expand this state in plane waves

$$\Psi_n(k) = \sum_N c_{n,k+N}\, e^{i(k+N)x}, \tag{A.29}$$

where k is the quasi-momentum and n is the band index. Inserting this superposition into the eigenvalue equation

$$H\Psi_n(k) = E_n(k)\Psi_n(k) \tag{A.30}$$

with the Hamiltonian for a stationary standing wave ($\phi = 0$ in Eq. (A.12)) and projecting onto the plane waves yields

$$\frac{(k+N)^2}{2}\, c_N + \frac{V_0}{2}\,(c_{N-1} + c_{N+1}) = E\, c_N, \tag{A.31}$$

where the indices k and n have been dropped. To solve this set of equations we solve for the eigenvalues and eigenvectors of

$$\mathbf{Hc} = E\mathbf{c}, \tag{A.32}$$

where **H** is the tri-diagonal matrix given by

$$H_{N,N} = \frac{(k+N)^2}{2} \tag{A.33}$$

$$H_{N,N+1} = H_{N,N-1} = \frac{V_0}{2}. \tag{A.34}$$

Since **H** is real and symmetric, the eigenvalues and eigenvectors are real. For each value of the quasi-momentum there is a set of possible eigenvalues and eigenfunctions that correspond to states for different band index n. The appropriate eigenstate can then be chosen as the initial condition for the evolution equation (A.20).

Bibliography

[1] O. R. Frisch, "Experimenteller Nachweis des Einsteinschen Strahlungsrückstosses," *Z. Phys.* **86**, 42 (1933).

[2] Claude Cohen-Tannoudji, Jacques Dupont-Roc, and Gilbert Grynberg, *Atom-Photon Interactions* (Wiley and Sons, New York, 1992).

[3] Steven Chu, "The manipulation of neutral particles," *Rev. Mod. Phys.* **70**, 685 (1998).

[4] Felix Bloch, "Über die Quantenmechanik der Elektronen in Kristallgittern," *Z. Phys.* **52**, 555 (1928).

[5] Emilio E. Mendez and Gérald Bastard, "Wannier-Stark ladders and Bloch oscillations in superlattices," *Physics Today*, June 1993, p. 34.

[6] Mark G. Raizen, Christophe Salomon, and Qian Niu, "New light on quantum transport," *Physics Today*, July 1997, p. 30.

[7] Kirk William Madison, *Quantum transport in optical lattices*, Ph.D. thesis, The University of Texas at Austin (1998).

[8] R. Graham, M. Schlautmann, and P. Zoller, "Dynamical localization of atomic-beam deflection by a modulated standing light-wave," *Phys. Rev. A* **45**, R19 (1992).

[9] Rodney Loudon, *The quantum theory of light* (Clarendon, Oxford, 1983), 2nd ed.

[10] Peter W. Milonni and Joseph H. Eberly, *Lasers* (Wiley and Sons, New York, 1988).

[11] Daniel A. Steck, "Sodium D line data," (February 2001). Available at `http://www.ph.utexas.edu/~quantopt/resources.html`.

[12] B. Segev, R. Côté, and M. G. Raizen, "Quantum reflection from an atomic mirror," *Phys. Rev. A* **56**, R3350 (1997).

[13] R. Côté, B. Segev, and M. G. Raizen, "Retardation effects on quantum reflection from an evanescent-wave atomic mirror," *Phys. Rev. A* **58**, R3999 (1998).

[14] K. B. Davis, M.-O. Mewes, M. A. Joffe, M. R. Andrews, and W. Ketterle, "Evaporative cooling of sodium atoms," *Phys. Rev. Lett.* **74**, 5202 (1995).

[15] Steven Chu, "Laser manipulation of atoms and particles," *Science* **253**, 861 (1991).

[16] E. Raab, M. Prentiss, A. Cable, S. Chu, and D. Pritchard, "Trapping of neutral sodium atoms with radiation pressure," *Phys. Rev. Lett.* **59**, 2631 (1987).

[17] Christopher John Myatt, *Bose-Einstein condensation experiments in a dilute vapor of rubidium*, Ph.D. thesis, University of Colorado (1997).

[18] W. Ketterle, K. B. Davis, M. A. Joffe, A. Martin, and D. E. Pritchard, "High densities of cold atoms in a dark spontaneous-force optical trap," *Phys. Rev. Lett.* **70**, 2253 (1993).

[19] W. Petrich, M. H. Anderson, J. R. Ensher, and E. A. Cornell, "Behavior of atoms in a compressed magneto-optical trap," *J. Opt. Soc. Am. B* **11**, 1332 (1994).

[20] P. D. Lett, W. D. Phillips, S. L. Rolston, C. E. Tanner, R. N. Watts, and C. I. Westbrook, "Optical molasses," *J. Opt. Soc. Am. B* **6**, 2084 (1989).

[21] Martin Christian Fischer, *Design and Performance of a Ring Dye Laser*, Master's thesis, The University of Texas at Austin (1993).

[22] T. W. Hänsch and B. Couillaud, "Laser frequency stabilization by polarization spectroscopy of a reflecting reference cavity," *Optics Comm.* **35**, 441 (1980).

[23] Neil W. Ashcroft and N. David Mermin, *Solid State Physics* (Saunders College, Philadelphia, 1976).

[24] Michael P. Marder, *Condensed Matter Physics* (Wiley and Sons, New York, 2000).

[25] Milton Abramowitz and Irene A. Stegun, eds., *Handbook of Mathematical Functions* (Dover, New York, 1965).

[26] E. Peik, M. B. Dahan, I. Bouchoule, Y. Castin, and C. Salomon, "Bloch oscillations of atoms, adiabatic rapid passage and monokinetic atomic beams," *Phys. Rev. A* **55**, 2989 (1997).

[27] J. B. Krieger and G. J. Iafrate, "Time evolution of Bloch electrons in a homogeneous electric field," *Phys. Rev. B* **33**, 5494 (1986).

[28] M. C. Fischer, K. W. Madison, Qian Niu, and M. G. Raizen, "Observation of Rabi oscillations betweeen Bloch bands in an optical potential," *Phys. Rev. A* **58**, R2648 (1998).

[29] Qian Niu, Xian-Geng Zhao, G. A. Georgakis, and M. G. Raizen, "Atomic Landau-Zener tunneling and Wannier-Stark ladders in optical potentials," *Phys. Rev. Lett.* **76**, 4504 (1996).

[30] K. W. Madison, M. C. Fischer, R. B. Diener, Qian Niu, and M. G. Raizen, "Dynamical Bloch band suppression in an optical lattice," *Phys. Rev. Lett.* **81**, 5093 (1998).

[31] K. W. Madison, M. C. Fischer, and M. G. Raizen, "Observation of the Wannier-Stark fan and the fractional ladder in an accelerating optical lattice," *Phys. Rev. A* **60**, R1767 (1999).

[32] S. R. Wilkinson, C. F. Bharucha, M. C. Fischer, K. W. Madison, P. R. Morrow, Qian Niu, Bala Sundaram, and M. G. Raizen, "Experimental evidence for non-exponential decay in quantum tunneling," *Nature* **387**, 575 (June 1997).

[33] C. Zener, "Non-adiabatic crossing of energy levels," *Proc. R. Soc. London A* **137**, 696 (1932).

[34] C. Zener, "A theory of the electrical breakdown of solid dielectrics," *Proc. R. Soc. London A* **145**, 523 (1934).

[35] C. F. Bharucha, K. W. Madison, P. R. Morrow, S. R. Wilkinson, Bala Sundaram, and M. G. Raizen, "Observation of atomic tunneling from an accelerating optical potential," *Phys. Rev. A* **55**, R857 (1997).

[36] K. W. Madison, C. F. Bharucha, P. R. Morrow, S. R. Wilkinson, Qian Niu, Bala Sundaram, and M. G. Raizen, "Quantum transport of ultracold atoms in an accelerating optical potential," *Appl. Phys. B* **65**, 693 (1997).

[37] L. A. Khalfin, "Contribution to the decay theory of a quasi-stationary state," *JETP* **6**, 1053 (1958).

[38] R. G. Winter, "Evolution of a quasi-stationary state," *Phys. Rev.* **123**, 1503 (1961).

[39] L. Fonda, G. C. Ghirardi, and G. C. Rimini, "A decay theory of unstable quantum systems," *Rep. Prog. Phys.* **41**, 587 (1978).

[40] K. Grotz and H. V. Klapdor, "Time scale of short time deviations from exponential decay," *Phys. Rev. C* **30**, 2098 (1984).

[41] P. T. Greenland and A. M. Lane, "Exposure of decay at non-constant rate by rapid fluctuations," *Phys. Lett. A* **117**, 181 (1986).

[42] Qian Niu and M. G. Raizen, "How Landau-Zener tunneling takes time," *Phys. Rev. Lett.* **80**, 3491 (1998).

[43] David E. Johnson and John L. Hilburn, eds., *Rapid Practical Designs of Active Filters* (Wiley and Sons, New York, 1975).

[44] B. Misra and E. C. G. Sudarshan, "The Zeno's paradox in quantum theory," *J. Math. Phys.* **18**, 756 (1977).

[45] C. B. Chiu, E. C. G. Sudarshan, and B. Misra, "Time evolution of unstable quantum states and a resolution of Zeno's paradox," *Phys. Rev. D* **16**, 520 (1977).

[46] P. Valanju, E. C. G. Sudarshan, and C. B. Chiu, "Spatial-temporal development of hadron-nucleus collisions," *Phys. Rev. D* **21**, 1304 (1980).

[47] J. J. Sakurai, *Modern Quantum Mechanics Revised Edition* (Addison-Wesley, New York, 1994).

[48] W. M. Itano, D. J. Heinzen, J. J. Bollinger, and D. J. Wineland, "Quantum Zeno effect," *Phys. Rev. A* **41**, 2295 (1990).

[49] P. Kwiat, H. Weinfurter, T. Herzog, A. Zeilinger, and M. Kasevich, "Interaction-free measurement," *Phys. Rev. Lett.* **74**, 4763 (1995).

[50] A. G. Kofman and G. Kurizki, “Quantum zeno effect on atomic excitation decay in resonators,” *Phys. Rev. A* **54**, R3750 (1996).

[51] A. G. Kofman and G. Kurizki, “Acceleration of quantum decay processes by frequent observations,” *Nature* **405**, 546 (2000).

[52] P. Facchi, H. Nakazato, and S. Pascazio, “From the quantum Zeno to the inverse quantum Zeno effect,” *Phys. Rev. Lett.* **86**, 2699 (2001).

[53] J.-Y. Courtois, G. Grynberg, B. Lounis, and P. Verkerk, “Recoil-induced resonances in cesium: An atomic analog to the free-electron laser,” *Phys. Rev. Lett.* **72**, 3017 (1994).

[54] D. R. Meacher, D. Boiron, H. Metcalf, C. Salomon, and G. Grynberg, “Method for velocimetry of cold atoms,” *Phys. Rev. A* **50**, R1992 (1994).

[55] Alexander Mück, *Recoil induced resonances for velocimetry of cold cesium atoms*, Master’s thesis, The University of Texas at Austin (1999).

[56] J. Guo, P. R. Berman, B. Dubetsky, and G. Grynberg, “Recoil-induced resonances in nonlinear spectroscopy,” *Phys. Rev. A* **46**, 1426 (1992).

[57] J. Guo and P. R. Berman, “Recoil-induced resonances in pump-probe spectroscopy including effects of level degeneracy,” *Phys. Rev. A* **47**, 4128 (1993).

[58] S. Guibal, C. Triché, L. Guidoni, P. Verkerk, and G. Grynberg, “Recoil-induced resonances of cesium atoms in the transient domain,” *Opt. Comm.* **131**, 61 (1996).

[59] Cyrus Bharucha, *Numerical simulation of a two-level atom in a modulated standing wave*, Master’s thesis, The University of Texas at Austin (1994).

[60] Georgios Andreas Georgakis, *Exploring Condensed Matter Problems Using Optical Lattices*, Ph.D. thesis, The University of Texas at Austin (1996).

[61] W. H. Press, S. A. Teukolsky, W. T. Vetterling, and B. P. Flannery, *Numerical Recipes in C* (Cambridge University Press, Cambridge, 1992).